EFFECTS FROM AS, CO, AND NI IMPURITIES ON PYRITE OXIDATION KINETICS: STUDIES OF CHARGE TRANSFER AT A SEMICONDUCTOR/ELECTROLYTE INTERFACE

By

Stephen William Lehner

Dissertation

Submitted to the Faculty of the

Graduate School of Vanderbilt University

in partial fulfillment of the requirements for

the degree of

DOCTOR OF PHILOSOPHY

in

Environmental Science

August, 2007

Nashville, Tennessee

Approved:

Professor Kaye S. Savage

Professor John C. Ayers

Professor David E. Cliffel

Professor Florence Sanchez

Professor James H. Clarke

To my children, Erin, Ava and Dylan

and

To my wife, Maria whose loving support made this work possible

ACKNOWLEDGEMENTS

We thank Leonard Feldman (Vanderbilt University Physics Department) for use of the Hall effect equipment. We are grateful to John Ayers and Peixin He of CH Instruments, Inc. for helpful discussion, and to Daniela Stefan for her assistance with pyrite synthesis and for providing the natural pyrite thick sections and characterization. I especially want to thank Madalina Ciobanu for her untiring assistance with all matters concerning electrochemistry. We appreciate assistance from Alan Wiseman (Vanderbilt University Dept. of Earth and Environmental Sciences) with the SEM. We thank Sankaran Mahadevan for support through NSF-DGE 0114329 (Integrative Graduate Education and Research Traineeship for Reliability and Risk Engineering Management (Vanderbilt University Department of Civil and Environmental Engineering). This study was supported by NSF-EAR 0409155 and 0617396 (KSS). Portions of the research were carried out at the Stanford Synchrotron Radiation Laboratory, a national user facility operated by Stanford University on behalf of the U.S. Department of Energy, Office of Basic Energy Sciences.

I would like to thank the members of my dissertation committee. I have learned a great deal from my conversations with John Ayers, Jim Clarke and David Cliffel thank Florence Sanchez for her guidance and advice in the examination process. I would especially like to thank Dr Kaye Savage for teaching me how to write and to become a scientist and for allowing me impromptu access to her time, our most valuable commodity.

No one has been more important to the success of this project than the members of my family. I would like to thank them for their patience in enduring the long hours and low pay that allowed me to achieve this transformation.

TABLE OF CONENTS

Page

ACKNOWLEDGEMENTS iii

LIST OF FIGURES vii

Chapter I vii
Chapter II vii
Chapter III ix
Chapter IV ix

LIST OF TABLES xi

Chapter

I. DISSERTATION OVERVIEW 1

Semi-chronological review of pyrite oxidation literature 3
Overview of dissertation chapters 10
Chapter II 10
Chapter III 11
Chapter IV 11
References 12

II. THE EFFECT OF AS, CO AND NI IMPURITIES ON PYRITE OXIDATION KINETICS: AN ELECTROCHEMICAL STUDY OF SYNTHETIC PYRITE 15

Abstract 15
Introduction 16
AC voltammetry response as an indication of surface state density 21
AC voltammetry: Metal electrodes 22
AC Voltammetry: pyrite 23
Methods 25
Samples 25
Composition and crystallinity 25
Bulk electrical properties 26
Electrochemical cell and electrode preparation 27
Cyclic voltammetry and AC voltammetry 27
Anodic and cathodic Tafel plots 28
Phase angle correction for nonfaradaic impedance 29
Results 29
Composition and crystallinity 29
AC and cyclic voltammetry 32
Statistical comparison of the oxidation proxies 32
Potential step experiments 35

Comparison of electrochemical proxies with bulk electrical properties..... 35
Relationships among the current peaks from AC and cyclic voltammetry... 35
Discussion..... 38
Anodic current at 1.1 V vs. anodic dissolution from potential step experiments: Evidence for corrosion by holes..... 38
Reactivity, surface state density and impurities..... 39
Evidence from electrochemical etching of the electrodes..... 39
Evidence for surface states from the AC response 41
Deep defect states of Ni and As suggest a connection between impurities and intra-band gap surface states..... 43
Correlation of electrochemical reactivity and bulk electrical properties..... 46
Evidence from AC voltammetry phase angles and nonfaradaic capacitance 47
Conclusions..... 50
Acknowledgements..... 51
References..... 51

III. THE EFFECT OF AS, CO, AND NI IMPURITIES ON PYRITE OXIDATION KINETICS: BATCH AND FLOW-THROUGH REACTOR EXPERIMENTS WITH SYNTHETIC PYRITE..... 56

Abstract..... 56
Introduction..... 57
Postulated mechanisms of pyrite oxidation..... 58
Pyrite oxidation rate dependencies 61
Methods 64
Samples..... 64
Reactor set-up..... 65
BET and particle size analysis..... 66
Reaction progress variables (RPVs)..... 67
Concentration of As, Co and Ni in sample and solution..... 68
Rate calculations..... 68
Data analysis..... 69
Results..... 69
Overview..... 69
BET surface area and particle size distribution..... 70
Impurity concentration in solid pyrite..... 71
MF reactor rates with ferric and ferrous iron as reaction progress variables (RPV)..... 72
MF reactor rates with sulfate as RPV..... 73
Batch reactor rates 73
Reaction rates as a function of impurity concentration in pyrite..... 75
Trace element concentration in solution (ICPMS)..... 75
Discussion..... 77
Conclusion..... 79
Acknowledgements..... 79
References..... 80

IV. ELECTROCHEMICAL IMPEDANCE SPECTROSCOPY OF SYNTHETIC PYRITE DOPED WITH AS, CO, AND NI: THE EFFECT OF IMPURITIES

ON CHARGE TRANSFER KINETICS..... 86

Abstract..... 86
Introduction..... 86
The effect of As, Co and Ni impurities on surface state energy..... 87
Methods..... 92
Samples..... 92
Composition..... 93
Bulk electrical properties..... 93
Electrochemical cell and electrode preparation..... 93
Impedance measurements..... 94
Equivalent circuit analysis..... 95
Data analysis..... 95
Results and discussion..... 96
Pyrite oxidation mechanisms..... 99
Equivalent circuit elements..... 100
Solution sample resistance..... 100
Charge transfer to ferric iron in solution..... 101
Surface state capacitance..... 105
Recombination in the inner circuit loop..... 106
Conclusions..... 108
Acknowledgements..... 109
References..... 109

V. IMPLICATIONS AND RECOMENDATIONS..... 112
References..... 115

APPENDIX I..... 116
Program script for Phreeqc ferric iron concentration and speciation calculation..... 116
Data from Chapter III experiments..... 116

APPENDIX II..... 127
Supplemental information for the EIS study (Chapter IV)..... 127
Correlation of EIS and AC voltammetry scans..... 127
Diagrams of model fits for EC: R(QR)(Q(C(C(RW))))..... 130

LIST OF FIGURES

Chapter I

Figure Page

1. Eh-pH diagram for iron oxides and sulfides in the presence of water at 25°C with total sulfur concentration of 0.1 mol L^{-1} after Faure (1998)..... 2

2. Acidic waters of the Rio Tinto pH 1.7 -2.5. Image taken by Linda Amaral Zettler (Bordenstein, 2006)..... 2

Chapter II

1. Possible equivalent circuit elements for the semiconductor electrode/solution interface. C signifies capacitance and R resistance. Subscript are as follows: SC is the space charge layer, SS is surface states, OX stands for oxide layer, and H is the Helmholtz layer (after Morrison, 1980)..... 24

2. Schematic of the electrochemical cell containing the pyrite working electrode with the space charge region exaggerated and no depiction of surface states..... 26

3. Synchrotron X-ray powder-diffraction patterns for selected synthetic samples, recalculated to display at $\lambda = 1.54$ Å (Cu-kα, see methods). Crystallinity is indicated by the flat background and sharp peaks. Inset shows SEM backscattered electron image of a synthetic pyrite crystal doped with Ni..... 33

4. Representative cyclic and AC voltammetry scans in pH 1.78 H_2SO_4 solution containing 1 mM ferric iron added as $FeCl_3$. Peak values for examples shown are close to the median for electrodes of each type..... 33

   A. CV scans showing relative value of anodic peak at 1.1V. The box is the potential region of ferric iron reduction..... 33
   B. Ferric iron reduction peaks from CV scans in (A.) (C) Median ferric iron reduction peaks from AC voltammetry. 33

5. Results from the statistical analysis for the four proxies for pyrite oxidation. For the box and whisker plots the notch represents the 95% confidence interval and the top and bottom represent the interquartile range (IQR) for the median from non-parametric statistics. The dotted lines represent the nearest observations within 1.5 IQRs. The diamond shows the 95% confidence interval for the mean from parametric statistics. Pluses are outliers..... 36

6. Tafel slopes for anodic oxidation of pyrite in 0.005 M H_2SO_4 solution, pH 2, with no added iron, from potential step experiments.
   Tafel slopes are ~ 1.4 V $decade^{-1}$; $\alpha \approx 0.57$..... 37

7. CV scans showing the effect of anodic polarization
   to 1.1 V in H_2SO_4 solution at pH 2 40

A. containing 10 mM ferric iron added as $FeCl_3$ 40
B. no added iron..... 40
8. Scanning electron microscope images of 40

A. Electrode 3B after polishing 40
B. Electrode 3B after anodic dissolution to 1.1V and AC voltammetry scan in H_2SO_4 solution at pH 1.78 containing 1 mM ferric iron added as $FeCl_3$ 40
C. Electrode 3C after applied potential was held at 1.1V for 30 minutes in 1M H_2SO_4 containing 6ppm ferric iron..... 40

9. Gerischer model diagrams showing the difference in response to applied alternating potential when surface state density leads to Fermi level pinning. 42

A. No Fermi level pinning, low surface state density..... 42
B. Fermi level pinning, high surface state density..... 42

10. Gerischer model diagrams for proposed mechanism by which bulk defect states from impurities result in higher surface state density..... 44

A. Undoped pyrite has low surface state density from mechanical defects. The space charge depletion region is deep, the potential barrier is high and there are few carriers available. Limited charge transfer can occur via the surface states..... 44
B.Co-doped pyrite has a defect state high in the bandgap overlapping the conduction band. Electrons are delocalized and free to move in response to an electric field. There is still a significant potential barrier; the extra surface states are so high in the band gap that they mirror the conduction band. Charge transfer can occur from the conduction band and through surface states. 44
C. The Ni-doped defect state is portrayed in the middle of the band gap. Due to the high density of surface states the space charge potential will remain constant despite applied potential as the band energies at the surface are free to move. Charge transfer can occur through surface states when applied potential raises the surface/bulk energy. 44
D. As-doped pyrite has a defect state low in the bandgap which is easily populated by thermally activated electrons. The bands bend down because the resulting charge carriers are positive (holes) and the depletion layer is negative in relation to the bulk. Like Ni-doped pyrite, the space charge potential will remain constant despite applied potential as the band energies at the surface are free to move and charge transfer can occur via surface states. 44

Chapter III

1. SEM secondary electron images showing the samples of synthetic pyrite from each doped population that were used for surface area measurements..... 63

2. Schematic showing mixed flow reactor setup..... 65

3. Example illustrating achievement of steady state conditions according to emf readings of effluent solution during the course of a typical mixed-flow reactor experiment..... 67

4. Results of statistical analyses of reaction rates for each population of synthetic pyrite samples, expressed in terms of three reaction progress variables: ferric iron reduction, production of ferrous iron, and production of sulfate. Rate distributions are shown for both mixed-flow experiments (left column) and batch reactor experiments (right column). The diamonds represent the 95% confidence interval for the mean from parametric analysis. The notched box and whisker plots represent Wilcoxon signed rank test. The notch is the 95% confidence interval for the median. The top and bottom of the box represents the inter-quartile range..... 72

5. Reaction rates for each pyrite sample determined from mixed flow reactor experiments, plotted against the concentration of impurity elements in the solid. Results for each reaction progress variable are shown. Each point represents one experiment. The star represents the Leadville natural sample and the open square represents the Elba sample..... 74

6. Solution concentrations of minor elements released from pyrite, after achievement of steady state in mixed flow reactor experiments, plotted against the concentration of impurity elements in the solid. Each point represents one experiment..... 75

7. Solution concentrations of minor elements released from pyrite over the course of batch reactor experiments. Values in legends represent the concentration of the impurity element in the reacting pyrite sample..... 76

8. Solution concentrations of minor elements released from the Leadville, CO pyrite sample over the course of a batch reactor experiment..... 76

Chapter IV

1. Nyquist plots showing the fit of the equivalent circuit model to the impedance data. The closed circles are the measured data and the open squares are the calculated fit. The solid line intersecting the Zreal axis is an example of the extrapolation of the semi-circle to obtain the charge transfer resistance. Values for other elecrodes constrained by the fitting procedure..... 96

    A. Undoped sample..... 96
    B. Ni-doped sample..... 96
    C. Co-doped sample..... 96
    D. As-doped sample..... 96

2. Schematic relating the equivalent circuit elements to physical components and processes. The equivalent circuit is below the Gerischer diagram depicting a Ni-doped pyrite/solution interface. Energy is on the Y axis and the X-axis is split between distance on the pyrite electrode side and probability on the solution side. The bell curves represent the distribution of allowed energy levels of the oxidized and reduced iron species in solution. The grey-shaded area represents the bulk defect state in the center of the band-gap energy of the Ni-doped pyrite. The solid arrows indicate charge transfer between the pyrite and solution while the dashed arrows indicate charge transfer between the bulk pyrite and the surface states..... 97

3. A. Statistical comparison of the equivalent circuit element R1 for synthetic electrodes grouped according to dopant type. The diamonds represent the 90% confidence interval for the mean from parametric analysis. The notched box and whisper plots represent Wilcoxon signed rank test. The notch is the 90% confidence interval for the median for populations with sufficient number of samples. The top and bottom of the box represents the inter-quartile range..... 101
B. Statistical comparison of the bulk resistivity values for electrodes from (2).... 101

4. A. Statistical comparison of the equivalent circuit element values for Q1 with the elecrodes grouped according to dopant type. 103
B. Comparison of the charge transfer resistance values for the electrodes grouped according to their relative response to the AC voltammetry (2)..... 103

5. A. statistical comparison of values for element C2 for electrodes grouped according to whether their AC voltammetry data gave meaningful phase angle values after subtracting the non faradaic impedance measured in the absence of the redox couple..... 107
B. Comparison of the values for element R3 for electrodes grouped according to dopant type..... 107

Appendix II

1. EIS impedance spectra displayed in three dimensions..... 127

2. Bode plot for EIS scan of 7331a As-doped electrode with low AC response score.... 128

LIST OF TABLES

Chapter II

Table Page

1. Impurity concentration, results of AC voltammetry, cyclic voltammetry and van der Pauw/Hall measurements..... 30

1. continued..... 31

2. Results of the Wilcoxon signed rank test..... 36

3. Correlations between bulk electronic properties and electrochemical proxies (R^2).. 37

4. Correlations between electrochemical proxies (R^2)..... 37

Chapter III

1. Calculated rates in nmol RPV $m^{-2}s^{-1}$ for mixed flow and batch experiments..... 70

2. Impurity concentrations in pyrite samples (parts per million)..... 71

3. One-sided statistical probabilities that pairs of synthetic pyrite populations differ in oxidation rates, calculated from mixed flow reactor results..... 73

4. One-sided statistical probabilities that pairs of synthetic pyrite populations differ in oxidation rates, calculated from 2nd order polynomial fit of batch reactor results..... 74

Chapter IV

1. EIS model parameters for synthetic pyrite..... 98

2. EIS model parameters for natural pyrite..... 98

Appendix I

1. Concentrations of reaction progress variables (RPV) in solutions collected from batch reactor experiments..... 116

2. Concentrations of RPV in solutions collected from mixed flow-through reactor data..... 123

Appendix II

1. The absolute value of total impedance and the phase angle from EIS spectra at ~ 100Hz. 129

2. Identity of electrodes with high and low AC response scores..... 129

3. Electrodes grouped according to phase angle correction..... 130

CHAPTER I

DISSERTATION OVERVIEW

Pyrite, $FeS_{2,}$ is the most common sulfide mineral near the Earth's surface. Both the sulfur and iron in pyrite are in a reduced state indicating that pyrite is stable in non-oxidizing environments (Figure 1). Many economically important commodities are also found in reduced environments rich in sulfur including coal, uranium, base metals and precious metals. Iron is naturally more abundant than precious and most base metals. Consequently, when sought-after metals in sulfide deposits are concentrated enough to be extracted economically, pyrite is almost always the dominant gangue mineral. As such, it is often exposed to oxidizing conditions in waste piles in or near surface waters. Under these conditions, pyrite is unstable and oxidation occurs producing sulfuric acid or what is termed acid mine drainage. This is an environmental challenge for mining interests and for land managers overseeing historical mining sites. Pyritic mining waste piles have the potential to produce acid for centuries. For example, the Rio Tinto mine in Spain, worked as early as 3000 BC by the Iberians and later by the Romans, has been a source of acid mine drainage for over 5000 years and yet is still an important source of copper and sulfur (Figure 2) (Bordenstein, 2006). Therefore, pyrite oxidation has been the focus of intense study for over 100 years. Since the 1960s much progress has been made toward understanding the mechanisms of this complex process. Described next are some highlights to provide a context for the work presented in the following chapters, which focuses specifically on how impurities in pyrite affect its oxidation.

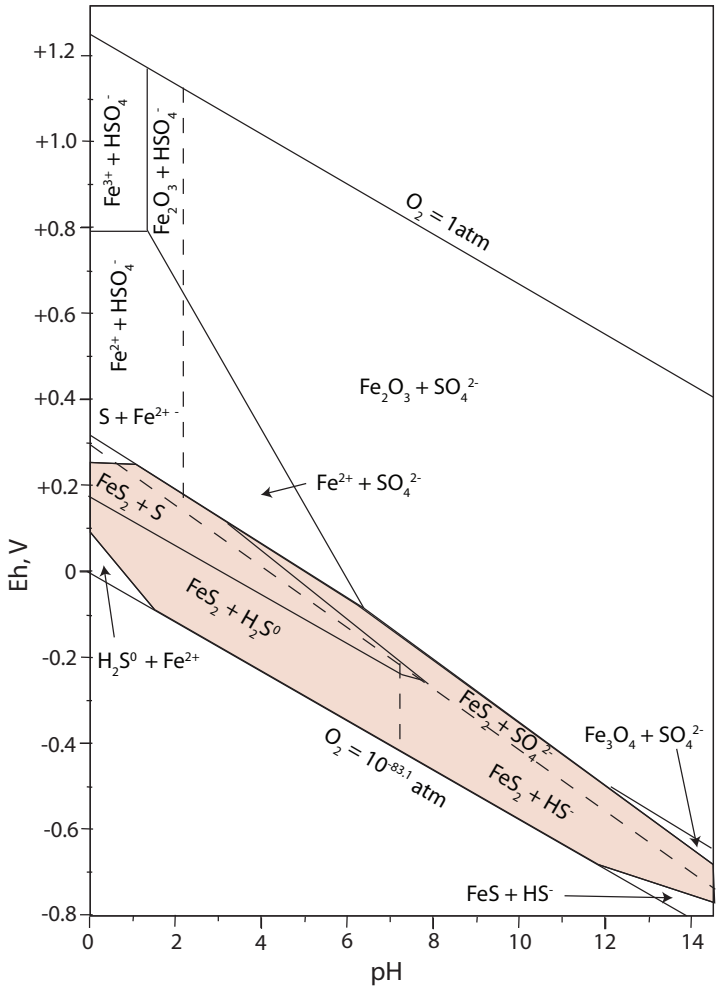

Figure 1. Eh-pH diagram for iron oxides and sulfides in the presence of water at 25°C with total sulfur concentration of 0.1 mol L^{-1} after Faure (1998)

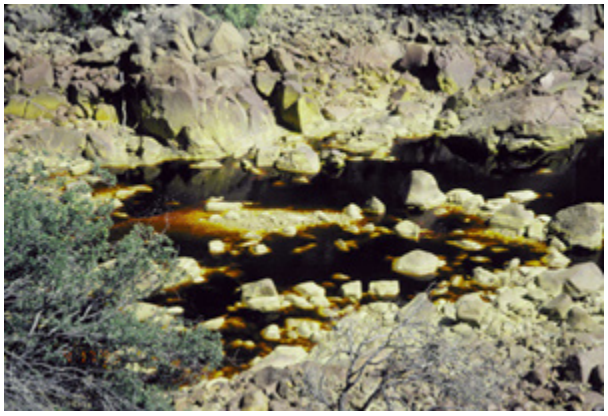

Figure 2. Acidic waters of the Rio Tinto (pH 1.7 -2.5). Image taken by Linda Amaral Zettler (Bordenstein, 2006) .

Semi-chronological review of pyrite oxidation literature

Pyrite oxidation is a complicated redox process whereby the sulfur in the FeS_2 is oxidized from a valence state of minus one to plus six in sulfate. The most common initial oxidation products are hydrogen ions, sulfate, and ferrous iron or, in other words, sulfuric acid and iron. Elemental sulfurand other intermediate S species are also observed under some conditions. Pyrite oxidation studies can be grouped according to three criteria: Abiotic aqueous pyrite oxidation, pyrite oxidation in moist air, and pyrite oxidation catalyzed by microbial activity. The focus of my research is on abiotic pyrite oxidation in aqueous systems near pH 2. The principle simplified, abiotic, aqueous reactions are:

$$FeS_2 + 7/2O_2 + H_2O = Fe^{2+} + 2SO_4^{2-} + 2H^+ \quad (1)$$

$$FeS_2 + 14Fe^{3+} + 8H_2O = 15Fe^{2+} + 2SO_4^{2-} + 16H^+ \quad (2)$$

Important secondary reactions include the oxidation of ferrous iron by dissolved oxygen:

$$Fe^{2+} + 1/4O_2 + H^+ = Fe3^+ + 1/2H_2O \quad (3)$$

and the precipitation of iron hydroxide as more neutral waters are encountered:

$$Fe^{3+} + 3H_2O = Fe(OH)_3 + 3H^+ \quad (4)$$

As a heterogeneous reaction, pyrite oxidation is usually assumed to be controlled by surface area. The mechanisms of this multi-step process are still sought after in hopes of discovering methods to control the production of acid drainage. We take up the saga with Singer and Stumm (1970) who reported that the rate-determining step in pyrite oxidation is the oxidation of ferrous iron by dissolved oxygen (Reaction 3). The resultant ferric ion was cited as the principle oxidant of the pyrite.

Weirsma and Rimstidt (1984) measured rates of reaction of pyrite and marcasite at pH 2 using ferric iron as the oxidant and the reaction progress variable. They found the reaction to conform to a rate law: $-\frac{dm_{Fe^{3+}}}{dt} = k\left(\frac{A}{M}\right)m_{Fe^{3+}}$, where m_{Fe}^{3+} is the molal concentration of ferric iron, k is the rate constant, A is the surface area of the pyrite and M is the mass of the solution. They measured oxidation rates of early diagenetic pyrite, formed at low temperature, and

compared them to those of high temperature hydrothermal pyrite. They found higher reactivity for the higher temperature pyrite but concluded that, geologically, the rate differences were insignificant.

McKibben and Barnes (1986) derived rate laws for the reaction of pyrite with ferric ion, dissolved oxygen, and hydrogen peroxide. They report that reactive surface area is less than total surface area and question the assumption of a first order dependence of oxidation rates on surface area.

Moses et al. (1987) explored pyrite reaction rates in solutions from pH 2 to 9 containing both dissolved oxygen and ferric iron. Using total sulfur and sulfate as reaction progress variables, they determined that the rate of oxidation was more dependent on the ferric iron concentration than on the presence of dissolved oxygen. At higher pH the role of oxygen became more important as an oxidant for ferrous iron thus providing a supply of ferric iron for the pyrite oxidation (Reactions 2 and 3). They speculated on the role of hydroxide radicals from the ferric iron hydration shell, citing isotopic studies indicating the oxygen in the sulfate product comes from the water, not dissolved oxygen.

Luther (1987) used molecular orbital theory to explain the observations of some of the previous studies of that time whereby the principle oxidant of pyrite is ferric iron. He hypothesizes the formation of a "persulfido" bridge. Essentially this means that the ferric ion attaches to the S_2^{2-} site on the pyrite surface via an inner sphere process. Single electron transfer steps occur between π^* S orbitals in the pyrite to lower energy π orbitals in the ferric ion via this bridge. The reaction proceeds by producing sulfoxy intermediates which are oxidized by reaction with ferric ion to ultimately form sulfate.

Brown and Jurinak (1989) studied pyrite oxidation in acid and alkaline solutions for up to 3 weeks and found the rate to be independent of time. They found that ferric iron is the rate-controlling oxidant even at high pH by observing the effect of DTPA on the reaction. Furthermore they report that the presence of Cl^- and SO_4^{2-} slow the rate of reaction with pyrite and they speculate that this is due to the complexing of ferric ion. They hypothesize an inner

sphere electron transfer via the disulfide surface site which is promoted by a hydroxyl bridging ligand.

Nicholson et al. (1988) studied the kinetics of pyrite oxidation in carbonate-buffered solutions. They varied the oxygen concentration, surface area and temperature of their solution at pH 6.7 to 8.5. In contrast to Brown and Jurinak (1989) they dismiss the role of ferric iron in this pH range. They found the same rate of oxidation in five different types of pyrite within 25%. They found a linear dependence of oxidation rate on the surface area and a non-linear relation with the oxygen concentration which was limited by the adsorption of O_2 and decomposition of oxidation products on the surface. The temperature dependence varied in an Arrhenious style with activation energy of 88 kJ. They give some trace element concentrations (but not arsenic) and they were unable to determine if the trace elements were in the pyrite or secondary phases. In a similar study in carbonate-buffered solution, Nicholson et al. (1990) ran their oxidation experiments for 59.52 weeks and report the rate decreasing with time. Surface analysis by XPS revealed a ferric oxide coating on the pyrite samples. They speculate that pyrite oxidation at near-neutral pH can be modeled by a shrinking-core concept whereby the grains become coated with ferric hydroxide, limiting the transport of H^+ ions and the reactivity of the pyrite surface.

Moses and Herman (1991) also studied pyrite oxidation near neutral pH and found that ferric iron is an effective oxidant but that the reaction requires dissolved oxygen. They proposed a mechanism whereby aqueous ferrous iron is adsorbed onto the surface preferentially over ferric iron. This adsorbed ferrous iron is oxidized by dissolved oxygen. The resulting adsorbed ferric iron then oxidizes the sulfur in pyrite reminiscent of the ideas presented by Singer and Stumm (1970). The adsorbed iron is then cycled between valence states until a stable sulfoxy species dissociates from the surface.

Reedy et al. (1991) used near isotopically pure O_2 and H_2O to study pyrite oxidation at pH 1. They report that in the absence of ferric iron the majority but not all of the oxygen came from the water, but that in the presence of ferric iron 90% of the oxygen came from the water.

They interpret Reaction 2 to be the dominant reaction at low pH while the reaction of dissolved oxygen directly with pyrite may be important at near neutral pH.

Mishra and Osseo Asare (1992) used electrochemical cyclic voltammetry to study the anodic dissolution of pyrite in 0.1 M $HClO_4$ and report the electro-adsorption of OH^- ions at pyrite surface iron d-states. Subsequently, the OH^- ions are transferred to sulfur surface states where the sulfur is progressively oxidized to thiosulfate.

Williamson and Rimstidt (1994) compiled rate data from the literature and produced rate laws for the oxidation of pyrite by dissolved oxygen and by ferric iron both in the presence of dissolved oxygen and in the absence of dissolved oxygen. They also performed experiments where a single pyrite sample was repeatedly reacted with identical solution conditions which showed the rate of oxidation slowing. They considered the fraction orders of reaction to indicate an electrochemical oxidation mechanism involving non-site-specific anodic and cathodic reactions. This is a somewhat different interpretation than the shrinking core concept proposed by Nicholson et al. (1990).

Evangelou and Zhang (1995) wrote a comprehensive survey of abiotic and biotic pyrite oxidation at low and high pH. They also reviewed treatment procedures for acid mine drainage. They conclude that pyrite oxidation initially proceeds by Reaction 1 but that oxidation and hydrolysis of the resulting ferrous iron releases acid into the environment. When the pH drops below 3.5 the reaction with ferric iron becomes dominant. Also at low pH pyrite oxidation is catalyzed by microbes. Microbial oxidation diminishes at higher pH but abiotic pyrite oxidation accelerates via hydroxyl surface complexation. Evangelou and Zhang also report evidence for increased pyrite oxidation in the presence of CO_2, resulting from carbonate ion surface complexation.

Wei and Osseo Asare (1996; 1997) report that the anodic dissolution of n-type (electrons as the dominant charge carriers) synthetic pyrite in acidic solutions occurs through transfer of holes (positively charged vacancies) to the valence band. They also report evidence from experiments in aqueous and non-aqueous electrolytes (1997) that both electrochemical

and chemical reactions take place requiring the presence of water.

Kelsall et al. (1999) used cyclic voltammetry, Fourier transform infrared spectroscopy, X-ray photoelectron spectroscopy and ion chromatography to study the oxidation of pyrite in 1 M HCl. They point to the semiconducting properties of pyrite to explain the wide potential range over which pyrite is relatively unreactive, suggesting that most of the applied potential falls across the space charge layer (see chapters II and IV). They propose a mechanism for the electrochemical oxidation involving progressive adsorption of OH^- from the dissociation of water leading to thiosulfate and the breaking of the Fe-S bond with other sulfoxy species as unstable intermediaries. Depending upon the potential, elemental sulfur and HSO_4^- may also form as reaction products. They report that, once ferric iron is released from the secondary oxidation of ferrous iron, it can further oxidize the pyrite surface as well as surface sulfur species to sulfate. The ratio of elemental S to sulfate depends upon the potential of the electrochemical dissolution.

Holmes and Crundwell (2000) used electrochemical techniques to study abiotic pyrite oxidation by dissolved oxygen and ferric iron from pH 1.5 to 3 in sulfuric acid solutions. Using cyclic voltammetry and stepped potential experiments they devised a general rate law based on the Butler-Volmer equation (Bard and Faulkner, 2001) that agreed well with their collected data and with the results of Williamson and Rimstidt (1994). Their interpretation was that, near pH 2, pyrite oxidation is predominantly an electrochemical reaction and that ferric iron is the predominant oxidant.

Rimstidt and Vaughn (2003) assessed the reaction mechanism of pyrite oxidation concluding that it is an electrochemical process which can be described by separate cathodic and anodic reactions that may occur on physically separated surface sites. The cathodic site supports the rate-determining step where an electron is transferred from a lattice cation (ferrous iron) to an oxidant, most commonly ferric iron or dissolved oxygen. This electron is replaced by one from the anodic site. The ferrous iron can be cycled between the ferric and ferrous state while at the anodic site the positive charge resulting from replenishing the cathodic site attracts water

molecules. The oxygen in the water molecules bonds with the surface sulfur and subsequently a proton is released into the solution. This process continues as the terminal S atom is progressively oxidized and protons are released into solution. Eventually, the sulf-oxy surface complex becomes unstable and is released into solution, usually in the form of sulfate but at higher pH perhaps in the form of thiosulfate.

Usher et al. (2004) used isotopically tagged H_2O and horizontal attenuated total reflection Fourier transform infrared spectroscopy to study the origin of oxygen in the reaction products of pyrite oxidation in water at neutral pH. They report the oxygen in the sulfate is primarily from water while the oxygen in the oxyhydroxides reaction product are only from dissolved oxygen. Usher et al. (2005) investigated the mechanisms of pyrite oxidation in moist air with the same methods. Noting that a small portion of the oxygen in the sulfate reaction product is from molecular oxygen they chose to investigate the relation between O_2 and H_2O as reactants. They show from the oxygen partitioning in the sulfate that the relative contribution from each reactant is a function of the concentration ratio of the reactants and the exposure history of the pyrite to the two reactants. Though the dissolution is more favored in the presence of water there appears to be more than one pathway for the formation of sulfate. Thus, while the electrochemical model where separate reactions occur on the cathodic iron sites and the anodic sulfur sites is still very useful, it does not account for all charge transfer pathways involved in pyrite oxidation (Usher et al., 2005).

Descostes et al. (2004) measured pyrite oxidation with batch reaction experiments at pH 2 and 3. They analyzed the S to Fe ratios and noted nonstoichiometric dissolution in the form of a sulfur deficit. They used thermodynamic equilibrium arguments to say that thiosulfate ($S_2O_3^{2-}$) and tetrathionate ($S_4O_6^{2-}$) form as intermediaries. Their proposed reaction path is for thiosulfate to be released from the pyrite surface which then disproportionates into thetrathionate and elemental sulfur. The insolubility of elemental sulfur explains the observed nonstoichiometric concentration of solution iron and sulfur. They also put forth the suggestion that SO_2 gas can be a byproduct of pyrite oxidation which is lost to the atmosphere further

explaining the sulfur deficit.

A comment on the Descostes (2004) article was written by Druschel and Borda (2006) in which they point out that thermodynamic relations are not necessarily relevant under the conditions in the study as the reactions are primarily dominated by kinetics. They propose other plausible explanations for the observed nonstoichiometry such as multiple series of elemental reaction steps or pathways and cite evidence that thiosulfate, though detected on the surface of oxidizing pyrite, is not the species released into solution.

This is a small subset of the voluminous literature on pyrite oxidation and the material properties of pyrite. The following chapters refer to this material in greater depth. The view emerging from the last fifty years of pyrite oxidation studies is that there are multiple pathways for pyrite oxidation to occur. As proposed by Druschel and Borda (2006) these include the electrochemical cell model suggested by Rimstidt and Vaughan where the oxidation of the disulfide proceeds through thiosulfate to sulfate released into solution, a pathway leading to the production of both S and polysulfides and perhaps a separate pathway where holes generated from light exposure or defects from impurities result in the nucleophilic attack of water eventually resulting in the breaking of bonds.

The work presented in this dissertation concerns an important and understudied aspect of the complex chemistry of pyrite oxidation, namely, the role of minor elements substituting for iron and sulfur in the pyrite crystal lattice. Three of the most common minor elements are As, Co, and Ni. Co and Ni are both in the 2+ valence state in low spin configuration (Vaughan and Craig, 1978). The valence state of As in the pyrite structure is controversial. While it could be in a minus one state substituting for S, it could also be in the 3+ state substituting for Fe. There are other possibilities due to the many valence states of As.

Pyrite is a semiconductor and has been extensively studied by materials scientists for applications in photovoltaics and battery design. It has been debated whether or not the variable semiconducting nature of pyrite has any effect on the rate of pyrite oxidation, though it has been acknowledged that pyrite oxidation is an electrochemical reaction. Observations suggest

that pyrite from certain sources is more reactive than others and one hypothesis is that the impurity content may be a factor. My research, focusing on these three common pyrite impurities shows that impurities do affect pyrite oxidation rates and mechanisms. My doctoral work is built upon the results of my previous work (Lehner, 2004; Lehner et al., 2006) which involved developing methods to synthesize pyrite doped with impurities and measuring the effect of As, Co and Ni on pyrite semiconducting properties.

Overview of dissertation chapters

Chapter II

The second chapter describes the use of electrochemical techniques to study the reaction of pyrite with ferric iron, thought to be the dominant pyrite oxidation reaction near pH 2. I felt it was important to relate the impurity concentration of a pyrite specimen to its solid state electrical properties and oxidation behavior. The specific goal was to compare oxidation rates of the synthetic pyrite types and to be able to relate the reactivity to the dopant concentrations and electrical properties. One great advantage of using electrochemical techniques is that they allowed study of aqueous oxidation behavior on the same pyrite thick sections that had previously been analyzed for impurity concentration (with laser ablation inductively coupled plasma mass spectroscopy) and whose semiconducting properties had been measured (with the van der Pauw four probe method). Another advantage of electrochemical techniques arises from using alternating current. An alternating potential is applied to the pyrite electrode and an alternating current is generated. The two signals are related to each other by the impedance which is, in effect, a charge transfer function expressed mathematically as a vector. Due to the small amplitude of the AC signal, the technique is very sensitive and information about processes occurring on a molecular scale can be inferred. In this chapter I show that pyrite with As, Co and Ni does oxidize faster than pyrite with very low impurity concentration (Figure 3). Based on the results, I hypothesize that the mechanism for this increased reactivity is the presence of intra-bandgap surface states at the pyrite/electrolyte interface introduced by impurities. These

results were published in the journal Geochimica et Cosmochimica Acta (Lehner et al., 2007).

Chapter III

The third chapter describes a series of experiments whose specific goal was to determine if the effects observed in the electrochemical study are observed using wet chemistry techniques which have been the mainstay in pyrite oxidation studies. Another goal was to measure the concentration of impurities released to solution from pyrite oxidation. For this work pyrite was ground, sieved and cleaned for batch and flow-through reactor experiments. In these experiments, done at pH 2 with added ferric iron, the reaction progress is monitored by measuring the change in concentration of reaction products over time. A total of 26 batch and 26 flow-through reactor experiments were conducted including two natural pyrite samples. The number of experiments enabled the use of statistical methods to compare the oxidation rates of the doped and undoped pyrite. The results of this study also show that pyrite with impurities oxidizes faster than pyrite with very low impurity concentration. The reactor solutions were also monitored for changes in minor element concentration using inductively coupled plasma mass spectroscopy. The study shows that Ni and Co concentrations in solution increased with time as pyrite containing them oxidizes but that As was not released to solution. The results also indicate that ferrous iron is recycled under experimental conditions. The results from this study were submitted for review to Geochimica et Cosmochimica Acta on June 20, 2007.

Chapter IV

The fourth chapter describes the results of a more in-depth investigation of the charge transfer mechanisms at the pyrite/electrolyte interface. In this study we employ electrochemical impedance spectroscopy wherein an AC voltage is applied at frequencies ranging from 10^5 to 10^{-4} Hz. The resulting three dimensional vector is modeled by an equivalent circuit of resistances, capacitances and constant phase elements. Though equivalent circuits are not necessarily

unique, the modeling results can be constrained by parameters obtained from the data and on theoretical concepts developed from years of research on the semiconductor/ electrolyte interface. The specific goal was to gain a deeper understanding of charge transfer mechanisms and to explain why pyrite with impurities is more reactive.

This study builds upon the results of Chapter II. The electrodes studied were chosen according to their response to the AC stimulus at 100 Hz and according to dopant type. Additionally 5 natural pyrite samples were investigated. The equivalent circuit model developed in Chapter IV provides evidence for, and a refinement of, the hypothesis formulated in Chapter II where charge transfer is mediated by impurity-introduced, intra-bandgap surface states. This work was submitted to The Journal of the Electrochemical Society on June 27, 2007.

References

Bard, A. J., and Faulkner, L. R., 2001, Electrochemical Methods: Fundamentals and Applications 2nd Edition: Hoboken, New Jersey, John Wiley and Sons Inc., 833 p.

Bordenstein, S., 2006, Rio Tinto, Spain, Science Education Resource Center, Carlton College.

Brown, A. D., and Jurinak, J. J., 1989, Mechanism of Pyrite Oxidation in Aqueous Mixtures: Journal of Environmental Quality, v. 18, no. 4, p. 545-550.

Descostes, M., Vitorge, P., and Beaucaire, C., 2004, Pyrite dissolution in acidic media: Geochimica et Cosmochimica Acta, v. 68, no. 22, p. 4559-4569.

Druschel, G., and Borda, M., 2006, Comment on "Pyrite dissolution in acidic media" by M. Descostes, P. Vitorge, and C. Beaucaire: Geochimica Et Cosmochimica Acta, v. 70, no. 20, p. 5246-5250.

Evangelou, V. P., and Zang, Y. L., 1995, A review: pyrite oxidation mechanisms and acid mine drainage prevention: Critical Reviews in Environmental Science and Technology, v. 25, no. 2, p. 141-199.

Faure, G., 1998, Principles and applications of geochemistry: Upper Saddle River, New Jersey, Simon & Schuster.

Holmes, P. R., and Crundwell, F. K., 2000, The kinetics of the oxidation of pyrite by ferric ions

and dissolved oxygen: an electrochemical study: Geochimica et Cosmochimica Acta, v. 64, no. 2, p. 263-274.

Kelsall, G. H., Yin, Q., Vaughan, D. J., England, K. E. R., and Brandon, N. P., 1999, Electrochemical oxidation of pyrite (FeS_2) in aqueous electrolytes: Journal of Electroanalytical Chemistry, v. 471, p. 116-125.

Lehner, S., Savage, K., Ciobanu, M., and Cliffel, D. E., 2007, The effect of As, Co, and Ni impurities on pyrite oxidation kinetics: An electrochemical study of synthetic pyrite: Geochimica et Cosmochimica Acta, v. 71, no. 10, p. 2491-2509.

Lehner, S. W., 2004, The effect of impurities on the electronic properties of pyrite crystals: Studies of synthetic pyrite (FeS_2) doped with As, Co, and Ni [Masters thesis]: Vanderbilt University, 84 p.

Lehner, S. W., Savage, K. S., and Ayers, J. C., 2006, Vapor growth and characterization of pyrite (FeS2) doped with Co, Ni, and As: Variations in semiconducting properties: Journal of Crystal Growth, v. 286, no. 2, p. 306-317.

Luther, I., George W., 1987, Pyrite oxidation and reduction: Molecular orbital theory considerations: Geochimica et Cosmochimica Acta, v. 51, no. 12, p. 3193-3199.

McKibben, M. A., and Barnes, H. L., 1986, Oxidation of pyrite in low temperature acidic solutions: Rate laws and surface textures: Geochimica et Cosmochimica Acta, v. 50, no. 7, p. 1509-1520.

Mishra, K. K., and Osseo Asare, K., 1992, Fermi Level Pinning at Pyrite (FeS_2) Electrolyte Junctions: Journal of the Electrochemical Society, v. 139, no. 3, p. 749-752.

Moses, C. O., and Herman, J. S., 1991, Pyrite oxidation at circumneutral pH: Geochimica et Cosmochimica Acta, v. 55, no. 2, p. 471-482.

Moses, C. O., Kirk Nordstrom, D., Herman, J. S., and Mills, A. L., 1987, Aqueous pyrite oxidation by dissolved oxygen and by ferric iron: Geochimica et Cosmochimica Acta, v. 51, no. 6, p. 1561-1571.

Nicholson, R. V., Gillham, R. W., and Reardon, E. J., 1988, Pyrite oxidation in carbonate-buffered solution: 1. Experimental kinetics: Geochimica et Cosmochimica Acta, v. 52, no. 5, p. 1077-1085.

-, 1990, Pyrite oxidation in carbonate-buffered solution: 2. Rate control by oxide coatings: Geochimica et Cosmochimica Acta, v. 54, no. 2, p. 395-402.

Reedy, B. J., Beattie, J. K., and Lowson, R. T., 1991, A vibrational spectroscopic ^{18}O tracer study of pyrite oxidation: Geochimica et Cosmochimica Acta, v. 55, no. 6, p. 1609-1614.

Rimstidt, J. D., and Vaughan, D. J., 2003, Pyrite oxidation: a state-of-the-art assessment of the reaction mechanism: Geochimica et Cosmochimica Acta, v. 67, no. 5, p. 873-880.

Savage, K. S., Tingle, T. N., O'Day, P. A., Waychunas, G. A., and Bird, D. K., 2000, Arsenic speciation in pyrite and secondary weathering phases, Mother Lode Gold District, Tuolumne County, California: Applied Geochemistry, v. 15, no. 8, p. 1219-1244.
Singer, P. C., and Stumm, W., 1970, Acidic Mine Drainage: The Rate-Determining Step: Science, v. 167, no. 3921, p. 1121-1123.

Usher, C. R., Cleveland, C. A., Strongin, D. R., and Schoonen, M. A., 2004, Origin of oxygen in sulfate during pyrite oxidation with water and dissolved oxygen: An in situ horizontal attenuated total reflectance infrared spectroscopy isotope study: Environmental Science & Technology, v. 38, no. 21, p. 5604-5606.

Usher, C. R., Paul, K. W., Narayansamy, J., Kubicki, J. D., Sparks, D. L., Schoonen, M. A. A., and Strongin, D. R., 2005, Mechanistic aspects of pyrite oxidation in an oxidizing gaseous environment: An in situ HATR-IR isotope study: Environmental Science & Technology, v. 39, no. 19, p. 7576-7584.

Vaughan, D. J., and Craig, J. R., 1978, Mineral Chemistry of Metal Sulfides, Cambridge Earth Science Series: London, New York, Melbourne, Cambridge University Press, 493 p.

Wei, D., and OsseoAsare, K., 1996, Semiconductor electrochemistry of particulate pyrite: Dissolution via hole and electron pathways: Journal of the Electrochemical Society, v. 143, no. 10, p. 3192-3198.

-, 1997, Semiconductor electrochemistry of particulate pyrite; mechanisms and products of dissolution: Journal of the Electrochemical Society: Electrochemical Science and Technology, v. 144, no. 2, p. 546-553.

Wiersma, C. L., and Rimstidt, J. D., 1984, Rates of reaction of pyrite and marcasite with ferric iron at pH 2: Geochimica et Cosmochimica Acta, v. 48, no. 1, p. 85-92.

Williamson, M. A., and Rimstidt, J. D., 1994, The kinetics and electrochemical rate-determining step of aqueous pyrite oxidation: Geochimica et Cosmochimica Acta, v. 58, no. 24, p. 5443-5454.

CHAPTER II

THE EFFECT OF AS, CO AND NI IMPURITIES ON PYRITE OXIDATION KINETICS: AN ELECTROCHEMICAL STUDY OF SYNTHETIC PYRITE[1]

Abstract

Synthetic pyrite crystals doped with As, Co, or Ni, undoped pyrite, and natural arsenian pyrite from Leadville, Colorado were investigated with electrochemical techniques and solid-state measurements of semiconducting properties to determine the effect of impurity content on pyrite's oxidation behavior. Potential step experiments, cyclic voltammetry, and AC voltammetry were performed in a standard three-electrode electrochemical cell setup. A pH 1.78 sulfuric acid solution containing 1 mM ferric iron, open to atmospheric oxygen, was chosen to approximate water affected by acid drainage. Van der Pauw/Hall effect measurements determined resistivity, carrier concentration and carrier mobility.

The anodic dissolution of pyrite and the reduction of ferric iron half-reactions are taken as proxies for natural pyrite oxidation. Pyrite containing no impurities is least reactive. Pyrite with As is more reactive than pyrite with either Ni or Co despite lower dopant concentration. As, Co and Ni impurities introduce bulk defect states at different energy levels within the band gap. Higher reactivity of impure pyrite suggests that introduced defect levels lead to higher density of occupied surface states at the solid-solution interface and increased metallic behavior. The current density generated from potential step experiments increased with increasing As concentration. The higher reactivity of As-doped pyrite may be related to p-type conductivity and corrosion by holes. The results of this study suggest that considering the impurity content of pyrite in mining waste may lead to more accurate risk assessment of acid producing potential.

1 Lehner, S., Savage, K., Ciobanu, M., and Cliffel, D. E., 2007, The effect of As, Co, and Ni impurities on pyrite oxidation kinetics: An electrochemical study of synthetic pyrite: Geochimica et Cosmochimica Acta, v. 71, no. 10, p. 2491-2509.

Introduction

Pyrite oxidation has been extensively studied for its role in the production of acid mine drainage, and as an important factor in ore enrichment processes. Pyrite is a semiconductor with a band gap of 0.95 eV; consequently, its oxidation properties are also of interest for their effect on its utility for solar energy conversion and electrochemical storage devices. Natural pyrite commonly contains As, Co and Ni impurities in some combination (Abraitis et al., 2004; Fleischer, 1955; Palache et al., 1944) but there has not been a systematic study of the effect of these minor elements on its oxidation rate, because naturally occurring pyrite crystals are often heterogeneous in concentration and distribution of minor elements (Craig et al., 1998). The present study assesses electrochemical response of synthetic pyrite doped with As, Co, and Ni and natural pyrite with As impurity to determine the influence of these minor elements without the complications arising from heterogenity and the presence of more than one minor element. The advantage of electrochemical studies, compared with batch or flow-through reaction studies on crushed pyrite, is that the measured reactivity of individual, intact pyrite thick sections can be related directly to their measured composition and solid-state properties.

The principal oxidants of pyrite responsible for the abiotic production of acid mine drainage are dissolved oxygen and ferric iron (reactions 1 and 2), with reaction (2) dominating below pH 2 (Rimstidt and Vaughan, 2003):

$$FeS_2 + 7/2O_2 + H_2O \rightarrow Fe^{2+} + 2SO_4^{2-} + 2H^+ \quad (1)$$

$$FeS_2 + 14Fe^{3+} + 8H_2O \rightarrow 15Fe^{2+} + 2SO_4^{2-} + 16H^+ \quad (2)$$

Pyrite oxidation can also be modeled as three electrochemical half-reactions: the anodic dissolution of pyrite, cathodic reduction of ferric iron ions, and the cathodic reduction of oxygen given by equations 4, 5, and 6, respectively (Holmes and Crundwell, 2000).

$$FeS_2 + 8H_2O \rightarrow Fe^{2+} + 2SO_4^{2-} + 16H^+ + 14e^- \quad (3)$$

$$Fe^{3+} + e^- \rightarrow Fe^{2+} \quad (4)$$

$$O_2 + 4H^+ + 4e^- \rightarrow 2H_2O \quad (5)$$

The oxidation rate law based on these individual half-reactions (Holmes and

Crundwell, 2000) agreed well with rate laws for oxidation of pyrite in solution with ferric iron, dissolved oxygen, or both, formulated by Williamson and Rimstidt (1994) on the basis of experimental results and data from the literature. Holmes and Crundwell (2000) concluded that pyrite oxidation is an electrochemical reaction and that semiconducting properties of individual samples could have an influence on oxidation rates.

Semiconducting electrical properties such as resistivity, charge carrier concentration and mobility are related to the type of impurity in pyrite (Bither et al., 1968; Chandler and Bene, 1973; Eyert et al., 1998; Lehner et al., 2006; Li et al., 1974; Zhao et al., 1993). We have studied the relationships among these electrical properties, impurity concentrations, and stoichiometry of synthetic pyrite doped with As, Co, and Ni and with negligible impurity (Lehner et al., 2006). From Hall effect measurements we found that resistivity, carrier concentration, and mobility vary predictably for pyrite with each type of impurity. For example, Co-doped pyrite has very low resistivity resulting from high carrier concentration and mobility. Electrons (n-type) or holes (p-type) may be charge carriers. All our synthetic pyrites are n-type except for As-doped pyrite which tends to be p-type.

The volume of literature on pyrite and its oxidation behavior is vast and spans well over a century of work. Pyrite has long been recognized as a semiconductor. The electromagnetic properties of sulfide ores were studied as early as the nineteenth century by Fox (1830) and Skey (1871) who measured the rest potentials of pyrite and other sulfides. Sveshnikov and Dobychin (1956) and Sato (1960) discovered that potential gradients between sulfide phases can lead to electrochemical dissolution of the phase with lower potential. As the field of electrochemistry has matured there have been many electrochemical studies of pyrite oxidation. Some have focused on the correlation of pyrite semiconducting properties with oxidation behavior. Springer (1970) reported no difference in anodic dissolution between n- and p-type pyrite and concluded that the semiconducting properties of natural pyrite have no effect on oxidation behavior. Biegler and Swift (1979) also found no systematic difference between n- and p-type natural pyrite in anodic dissolution experiments in acid solutions.

A number of other studies, however, do suggest that variable electrical properties arising from impurities and defects in pyrite may affect its oxidation rate. Crundwell (1988) asserts that the solid state electrical properties of sulfide minerals must be taken into account in order to understand the anodic dissolution behavior. Becker et al. (2001) and Rosso and Becker (2003) reported the "proximity effect" whereby electrons from one crystal site are transferred to remote sites where a reaction is taking place. This may imply that variations in resistivity such as we have observed (Lehner et al., 2006) could play a role in charge transfer kinetics. Dependence of oxidation rates on photo-excitation indicates that charge carrier type and concentration may be significant. For example, Schoonen et al. (2000) found a strong temperature dependence for pyrite oxidation by dissolved oxygen, and an accelerated rate when pyrite is exposed to visible light. Jaegermann and Tributsch (1983) attributed pyrite's photocurrent to photo-generated holes.

There is conflicting evidence on the role of holes in facilitating pyrite oxidation. Crundwell (Crundwell, 1988) suggested that pyrite resists dissolution by holes due to the non-bonding nature of the valence band orbitals. However, Wei and Osseo-Asare (1996) studied electrochemical dissolution of synthetic particulate n-type pyrite and concluded from the photo-response that anodic dissolution occurs by transfer of holes from the valence band to the surface, while cathodic dissolution involves transfer of electrons from the conduction band. They report in a subsequent study (Wei and OsseoAsare, 1997) that the mechanism of anodic dissolution in acidic media involves both chemical and electrochemical processes requiring the presence of water. By comparing synthetic n-type and p-type pyrite, our experiments provide new evidence for the possible role of holes.

The relationship between pyrite's band energy structure and intrinsic surface states, which are energy levels available to electrons within the band gap at the semiconductor surface, may also influence oxidation behavior. Bronold et al. (1994) conclude that Fe surface states are located within the band gap due to loss of degeneracy from the surface coordination. They report that if the concentration of surface states is high enough it can lead to the Fermi level

being pinned near the valence band edge. Fermi level pinning describes a situation in which the average energy level of electrons at the surface is controlled by surface states independent of applied potential (Bard et al., 1980). Under these conditions a pyrite electrode behaves as a metal. Ennaoui et al. (1986) report Fermi level pinning caused by surface states, and indicate that the oxidation reaction is mediated by these intra-band gap surface states. Fan and Bard (1991) also postulate a localized surface state within the band gap based upon results from scanning tunneling microscopy and tunneling spectroscopy on pyrite surfaces. Density functional theory calculations by Hung et al. (2002a; 2002b) indicate that the band gap is reduced and in some cases eliminated at intrinsic surface states on pyrite. Due to Fe coordination numbers of 4 and 5, compared with 6 in the bulk crystal, the Fe t_{2g} electrons at the top of the valence band lose their degeneracy and assume energy levels above one another, approaching the conduction band. At some sites (for example, on {111} planes) an electron from the highest energy electron pair will be able to occupy an antibonding orbital in the conduction band; the loss of spin parity results in paramagnetic regions. These regions are more attractive to molecular oxygen when exposed to air or water, and so may explain why pyrite oxidation has been observed to proceed from step and kink sites.

Several studies, noting that the ideal pyrite {100} surface would contain dangling Fe^{2+} bonds as surface states, suggest that pyrite oxidation is initiated as Fe^{2+} is oxidized to Fe^{3+} and instantly reduced by electrons from the lattice, ultimately resulting in the oxidation of S_2^{2-} anions (Rimstidt and Vaughan, 2003; Rosso et al., 1999). However, the surface of pyrite never breaks ideally along the {100} plane (Nesbitt et al., 1998). In conchoidal fractured pyrite where the surface may contain terraces, kinks, and perhaps fracture planes such as the {110}, {210}, and {111}, about 40% of the S-S bonds are broken. The surface S^- oxidizes the dangling Fe^{2+} resulting in about 40% of the Fe surface states being Fe^{3+} (Nesbitt et al., 1998). Schaufuß et al. (1998) used synchrotron sourced X-ray photoelectron spectroscopy to study the surface sulfur states and sulfur oxidation products of freshly fractured natural pyrite in air. They report sulfur surface species in order of decreasing reactivity: S^{2-}, S_2^{2-} with surface coordination, and S_2^{2-} with

bulk coordination. The S^{2-} species form immediately from S^{-} at fractured S-S bonds consistent with Nesbitt et al.'s (1998) reduction of S^{-} by Fe^{2+}. Schaufuß et al. (1998) proposed a mechanism whereby oxidation proceeds from the resulting Fe^{3+} dangling bonds. From these studies it appears that intrinsic surface states are a major factor in the initiation and mechanism of pyrite oxidation, but the relation between impurity atoms and surface states has not been explored.

In the present study, by comparing single-dopant and undoped synthetic pyrite that display different solid-state electrical properties, we address the relation between electrical properties and oxidation behavior without the complexity introduced by heterogeneous natural pyrite samples containing multiple minor elements. We employed cyclic voltammetry (CV), steady state voltammetry, and alternating current (AC) voltammetry to compare the electrochemically driven rates of pyrite oxidation for synthetic pyrite with different impurity compositions. We also investigated natural pyrite from Leadville, Colorado with As and Pb as the main impurities. We chose a system for the cyclic and AC voltammetry experiments below pH 2 that would approximate water affected by acid drainage. No attempt was made to eliminate oxygen.

Previous studies suggest that Fe^{3+} is the dominant pyrite oxidant and that Reaction 2 is the dominant redox reaction in this range (Rimstidt and Vaughan, 2003). We therefore focused on the current generated by cyclic and AC voltammetry corresponding to the reduction of ferric iron (Reaction 4) but also on the forced anodic dissolution (Reaction 3). The release of pyrite-derived ions into solution (Reaction 3) allows electrochemically driven reaction rates to be assessed by comparing the magnitude of the current generated by different pyrite electrode materials at the applied potentials where Reactions 3 and 4 occur. Current density, which is related to the stoichiometry of the reaction (the number of electrons transferred), is measured in A cm^{-2} or C s^{-1} cm^{-2}. Coulombs (C) are related to moles reacted through Faraday's constant. This study was designed to assess the behavior of differently doped pyrite crystals under identical electrochemical and solution conditions, rather than to develop explicit rate laws.

To investigate Reaction 4, we use AC voltammetry, a technique that is very sensitive to reaction rates due to the small amplitude and sinusoidal frequency of the applied potential. The

amplitude of the AC current near the equilibrium potential of the ferric/ferrous iron couple with which the pyrite electrode responds to alternating voltage is directly proportional to the standard heterogeneous rate constant and frequency (Bard and Faulkner, 2001; Breyer and Bauer, 1963; Smith, 1966). The standard heterogeneous rate constant corresponds to the exchange current which is the current of the forward and backward redox reactions when they are equal, i.e., at equilibrium. It is a measure of the kinetic facility of a reaction.

We report here on four proxies for the rate of pyrite oxidation that can be related to the impurity concentrations determined by LA-ICPMS and the bulk electrical properties determined by Hall effect-four-probe method for the same pyrite thick section: (i) the cyclic voltammetry current peak generated from the reduction of ferric iron, and (ii) the amplitude of the AC voltammetry peak from the reduction of ferric iron, both corresponding to reaction (4); (iii) the current generated from the anodic dissolution of pyrite at 1.1 V versus the Ag/AgCl 3M KCl reference electrode, corresponding to reaction (3); and (iv) the standard heterogeneous rate constant, k^o, calculated from the phase shift between the current and the applied potential vectors from the reduction of ferric iron in response to AC voltammetry. We use a pH 1.78 H_2SO_4 solution with 1 mM ferric iron added as $FeCl_3$. In addition to these four proxies, evidence of higher oxidation rate for pyrite with As impurity over the other types is presented in the form of the anodic branch of Tafel slopes generated from potential step experiments in pH 2 H_2SO_4 solutions between 0.65 and 0.1 V versus the Ag/AgCl 3M KCl reference electrode.

AC voltammetry response as an indication of surface state density

In AC voltammetry a sinusoidal voltage is applied to the electrode during a constant DC scan rate. The frequency of the sinusoidal voltage is much higher than the DC scan rate and the amplitude of voltage is small relative to the applied DC voltage. Both the alternating current and alternating voltage are expressed as phasors. They are related to each other by the impedance, a vector quantity, which has a resistive and a capacitive component. It is expressed as a complex number with the resistive component being the real part and the capacitive reac-

tance the imaginary part:

$$Z(\omega) = Z_{Re} - jZ_{Im} \qquad (6)$$

where Z_{Re} is resistance, $j = \sqrt{-1}$, and Z_{Im} is the capacitative reactance $1/\omega C$, where ω is angular frequency and C is the capacitance (Bard and Faulkner, 2001). The phase angle (ϕ) between the applied voltage and the resulting current is equal to the phase angle between the impedance vector, $Z(\omega)$, and the resistive (ZRe) component. As the AC signal is applied successively through the potential region most favorable to a particular reaction the maximum value for the cotangent of the phase angle occurs near the equilibrium potential for the reaction. Cot (φ) at this potential is inversely proportional to the standard heterogeneous rate constant:

$$k^o = \frac{\left(2D_O^b D_R^a\right)^{1/2} w^{1/2}}{\left[(\cot f)_{max} - 1\right]\left[\left(\frac{a}{b}\right)^{-a} + \left(\frac{a}{b}\right)^{b}\right]} \qquad (7)$$

where D_O and D_R are the diffusion coefficients for the oxidized and reduced species respectively; α is the transfer coefficient, $\beta = 1 - \alpha$; and ω is the angular frequency (from eqn. 10.5.26, Bard and Faulkner, 2001). This relationship holds for irreversible and quasi-reversible reactions (Bard and Faulkner, 2001). The phase angle at the potential of maximum cot (φ) is independent of the bulk solution concentration of the oxidant, the electrode surface area, the amplitude of the alternating potential, and the frequency of the AC signal. Thus, the k^o values calculated from the phase angles are evidence that the experimental results are not due only to surface area irregularities or to varying solution conditions.

AC voltammetry: Metal electrodes

To understand the utility of the phase angle (φ) it is useful to consider metal electrodes. The DC voltage controls the ratio of oxidized to reduced species near the surface of the

electrode. Because the AC signal is small compared to the applied DC potential, this ratio near the electrode surface has the same effect as if it were the bulk ratio in solution. Changing the DC potential is therefore equivalent to conducting multiple experiments using solutions with different redox conditions. For a metal electrode the total measured capacitance of the system is due to the capacity of the solution/electrode interface known as the Helmholtz capacitance or double layer capacitance, in parallel with the so-called pseudocapacitance of the charged redox species reacting with the surface. The pseudocapacitance arises from the faradaic process (the redox reaction) and is a function of the redox condition, the diffusion characteristics of the redox couple and the frequency of the AC signal. At a given redox condition (fixed DC potential) and frequency, the pseudocapacity should be the same for different metal electrodes; however, the resistance component of the impedance will vary depending on the charge transfer resistance for the different electrode material.

For a completely reversible redox reaction, by definition there is no charge transfer resistance and so $\varphi = 45^{o}$. In this case both the capacitive reactance and the resistance vector are defined by the diffusion characteristics of the redox couple and they are equal. As reactions become less reversible the charge transfer resistance increases the resistance vector, φ decreases, and cot (φ) increases. Therefore k^{o}, the rate constant for the equilibrium exchange current, is proportional to φ in a semi-reversible to irreversible system. The measured values have only to be corrected for the solution resistance and Helmholtz capacitance (Bard and Faulkner, 1980).

AC Voltammetry: pyrite

Pyrite, being a semiconductor, has at least two additional sources of capacitance that function in parallel to each other and in series with the Helmholtz capacitance (Figure 1, dashed region). One is the space charge region which is charged relative to the bulk pyrite due to surface states and reaction with species in solution. The result is a capacity due to either depletion or an excess of charge carriers. The capacitance of the space charge region is much

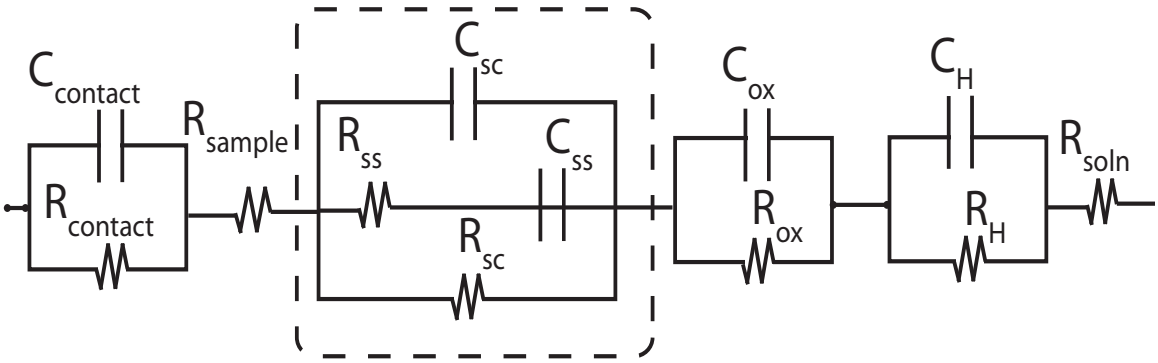

Figure 1. Possible equivalent circuit elements for the semiconductor electrode/solution interface. C signifies capacitance and R resistance. Subscript are as follows: SC is the space charge layer, SS is surface states, OX stands for oxide layer, and H is the Helmholtz layer (after Morrison, 1980).

smaller than the Helmholtz capacitance and therefore its capacitive reactance is much larger. The Helmholtz capacitance is considered a minor source of error in semiconductor surface characterization whereas the space charge capacitance is significant and changes as a function of applied potential (Morrison, 1980). The other source of additional capacitance is the surface states themselves: the available energy levels resulting from surface defects, adsorbed species, and impurity atoms. Unlike the space charge capacitance and the Helmholtz capacitance, which are similar to a parallel plate capacitor in that they can reversibly gain or lose charge, the surface state capacitance is dependent on the mobility of electrons between surface states and the bulk or species in solution. If the surface state capacitance is large, as may be the case if there are a large number of defect and impurity states, then the surface state capacitance should dominate the space charge capacitance and the electrode could behave as a metal. To obtain meaningful phase angles, measured values have to be corrected for all sources of non-faradaic capacitance and resistance. Figure 1 is an equivalent circuit showing some of the possible circuit elements affecting the semiconductor/solution interface. We can infer a relationship between surface states and impurity concentration by measuring the non-faradaic capacitance and resistance and applying the correction.

Methods

Samples

The pyrite used in this study is from two sources. Most samples were synthesized in our laboratory where pyrite crystals are grown with chemical vapor transport (CVT) in sealed evacuated quartz tubes in a temperature gradient of 700 to 550 °C over 16 cm using $FeBr_3$ as a transport agent (Lehner et al., 2006). The synthesized pyrite was doped with either As, Co, Ni or nothing at all. Pyrite from the Black Cloud Mine (Leadville, CO) that was found to contain primarily As and Pb impurities was also studied. Crystals at least 2 mm^3 were mounted in epoxy and cut into sections approximately 1 mm thick with a slow speed diamond saw.

Composition and crystallinity

The thick sections were analyzed for dopant concentration using laser ablation inductively coupled plasma mass spectrometry (LA-ICPMS) with a New Wave UP 213 laser ablation system coupled with a Perkin Elmer Elan DRC ICPMS using Ar plasma. Laser ablation scans were typically collected along a line from the epoxy near the edge of the mounted crystal to at least the center of the specimen. The scans were pre-ablated at 50% power at a rate of 70 μm/sec over a swath of 160 μm width to remove any residue. The analysis scan ablated an 80 μm swath down the middle of the pre-ablation path at a rate of 10 μm/sec at 65% power. Concentration and error was calculated as described in Lehner et al (2006) using a USGS prepared sulfide standard (Wilson et al., 2002). Pb concentration detected in the Leadville, Colorado samples was not quantified because the sulfide standard was not quantified for Pb.

Typical synthetic pyrite crystals from each dopant category were analyzed using synchrotron X-ray diffraction at the Stanford Synchrotron Radiation Laboratory, Beam Line 2-1. The wavelengths of the incident radiation, calibrated by Rietveld refinement of a powdered LaB_6 reference standard diffraction pattern (space group $Pm3m$, a = 4.1566 Å), were λ = 0.976 Å (data shown is 16° - 56° 2θ, step size 0.006°) or λ = 1.239 Å (20° to 64° 2θ, step size 0.008°) depending on when the data were collected. Samples were each loaded into the well inset of a

flat silicon plate after grinding to a smooth paste with mortar and pestle under acetone. The flat plate was rocked through $\theta = 2^{\circ}$ to minimize preferred orientation effects during data collection. The resulting data were recalculated to show the equivalent range of 2θ for Cu-kα ($\lambda = 1.54$ Å) to allow visual comparisons.

Bulk electrical properties

The resistivity, carrier concentration, and mobility were measured by a four probe MMR Technology van der Pauw/Hall set up as described in Lehner et al (2006). For the electrical measurement, the mounted pyrite surface was cleaned with methanol and left rough to facilitate ohmic contact with the gold probes. To ensure repeatability a series of 6 - 12 measurements was performed. To avoid distortion from applying more current than the sample could conduct, the current was increased in equal steps through an order of magnitude in range ending approximately 50% below the maximum current that the sample would transmit with applied potentials of up to 2.4V. The values reported for resistivity, carrier concentration and mobility are approximate. The error analysis is discussed in Lehner et al. (2006).

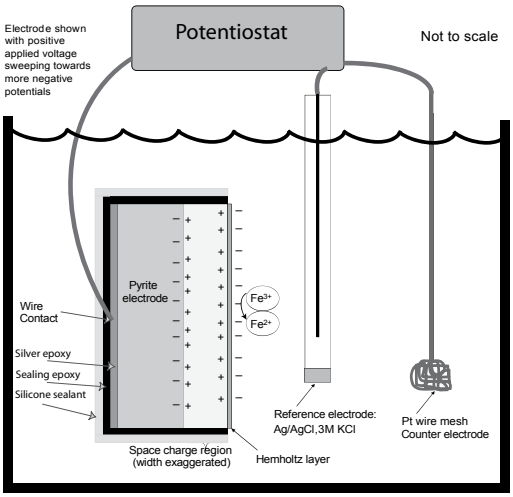

Figure 2. Schematic of the electrochemical cell containing the pyrite working electrode with the space charge region exaggerated and no depiction of surface states.

Electrochemical cell and electrode preparation

Electrochemical experiments were conducted in a standard three electrode cell setup (Figure 2) with approximately 4 mL of H_2SO_4 solution at pH 1.78 containing 1 mM ferric iron added as $FeCl_3$. The counter electrode was a platinum wire mesh. The reference electrode was the Ag/AgCl, 3M KCl. All voltages reported in this manuscript are versus this reference electrode. The pyrite working electrode was formed from previously analyzed thick sections by attaching copper wires with silver epoxy. The surface to which the wires were attached was first cleaned and etched for several hours with a 50% solution of H_2SO_4 or HCl. Once the silver epoxy had set, the back of the electrode with the contact was enclosed in sealing epoxy followed by silicone aquarium sealant leaving only one surface of the pyrite in contact with the solution in the electrochemical cell. The exposed surface was polished to 3 μm roughness with 600 grit silicon carbide sandpaper followed by a 3 μm diamond polishing compound. The flat surface area was calculated from digital photographs of the electrodes next to a precision scale.

Cyclic voltammetry and AC voltammetry

The cyclic voltammetry was performed with a CHI660 potentiostat controlled by CHI version 5.02 software at a scan rate of 0.01 Vs^{-1} over the potential region of 0 to 1.1 V. The initial scan polarity was positive and the sampling interval was 0.001V. The AC voltammetry was performed from 0.7 to 0.2 V in increments of 0.004 V. The frequency was 100Hz with alternating voltage amplitude of 0.05V held for 1 second. The preparation consisted of re-polishing the electrode with 3 μm diamond paste for approximately 5 minutes. The electrode was then washed in alconox solution and rinsed with acetone followed by DI water. This washing and rinsing sequence was performed twice followed by wiping with a fresh Kimwipe™. The electrodes were then etched with 50% HCl solution for at least 5 minutes after which they were again rinsed with DI water and placed in the electrochemical cell. The procedure for these measurements was to polish, wash, and etch the pyrite electrode followed by the CV scan which had the effect of electrochemically etching the pyrite. Then the AC voltammetry

was performed. Peak magnitudes for both the AC and cyclic voltammetry were calculated by subtracting the background or nonfaradaic current.

For the background capacitance measurements the same washing and polishing procedure was performed followed by the AC voltammetry experiment in a 0.1M KCl solution prepared with de-ionized water. The solution resistance of the pH 1.78 H_2SO_4 with 1 mM ferric iron was measured with electrochemical impedance spectroscopy performed at 0.1 V, 0.48 V and 0.6 V in a frequency range of 0.01 Hz to 10^5 Hz and amplitude of 0.005 V. All electrodes were placed in approximately the same configuration in each experiment to minimize the variability of solution resistance.

An AC response score was calculated as: $\frac{|i_P - i_{B_P}|}{|i_{B_1} - i_{B_2}|}$ where i_P is the current peak value, i_B represents the background current with B_1 being the background current at the beginning of the scan, B_2 the background current at the end of the scan and B_P the background current at the peak potential. If the value was less than one, the magnitude of the AC peak was less than the background fluctuation. The magnitude or lack of AC response was used to compare the reactivity of different electrodes and pyrite types.

Anodic and cathodic Tafel plots

The potential step experiments were performed in an H_2SO_4 solution at pH 2.0, with no added iron. The current was measured at fixed potentials for 2 minutes in increments of 0.05 V starting at 0.65 V to 0.25 V vs Ag/AgCl, 3 M KCl. The current was recorded every 0.1 seconds for 120 seconds. The asymptotic value of the potential after 120 seconds was used to construct the Tafel slope for the anodic dissolution of pyrite (Holmes and Crundwell, 2000). This was done for 7 As-doped, 2 Co-doped, 2 Ni-doped and 5 undoped pyrite electrodes. The slopes yield the transfer coefficient (α) from the Butler-Volmer model of electrode kinetics which is also used to calculate k^o from the AC phase angles (Bard and Faulkner, 2001). The transfer coefficient is a measure of the symmetry of the activation energy for a reaction with respect to reaction progress. Theoretically, it is different for semiconductors than for

metals. For an intrinsic semiconductor, where charge transfer is often rate limiting due to limited carriers and no states in the band gap, the transfer coefficient is expected to be 0 for redox couples near the conduction band energy and 1 for couples near the valence band, whereas for metals it is expected to be near 0.5 (Morrison, 1980).

The cathodic slope of the Tafel plot corresponding to the reduction of ferric iron was measured with scans of 0.01 and 0.005 Vs^{-1} in the pH 1.78 solution of H_2SO_4 with 1 mM ferric iron. This was done for 5 As-doped, 2 Co-doped, 2 Ni-doped and 2 undoped pyrite electrodes. The cathodic Tafel slope was also measured for 2 Co-doped and 2 Ni-doped electrodes using stair-step voltammetry with the potential fixed for 10 seconds in increments of 0.02 V in a 0.015 M $FeCl_3$ solution.

Phase angle correction for nonfaradaic impedance

In order to correct for the nonfaradaic resistance and capacitance, we modeled the system as a resistance and capacitance in series. The solution resistance was first subtracted from the measured resistance. Then, the series was converted to a parallel system where the non-faradaic capacitance was subtracted. The system model was then converted back to a series (Bard and Faulkner, 1980). The phase angle (φ) was calculated from the remaining faradaic capacitive reactance and resistance.

Results

Composition and crystallinity

Dopant concentrations are reported in Table 1. Samples with impurity concentrations less than 50 ppm were classified as undoped (but are labeled in Table 1 with their intended dopant). Figure 3 shows the results of the synchrotron X-ray diffraction analyses and a scanning electron micrograph of a typical Ni-doped crystal. The crystal morphology and sharp diffraction peaks that match the planar spacings of pyrite are evidence of the material's identity as pyrite.

Table 1. Impurity concentration, results of AC voltammetry, cyclic voltammetry and van der Pauw/Hall measurements

Electrode	LA-ICPMS		AC Voltammetrey					Cyclic voltammetrey		Hall - van der Pauw measurements			
	Impurity ppm[a]	Error[f] ppm	AC peak $\mu A cm^{-2}$	Meas. φ	Corrected φ	AC Resp. score	k^o $cm\ s^{-1}$	Fe^{3+} peak $\mu A\ cm^{-2}$	Anodic peak $\mu A\ cm^{-2}$	Resistivity ohm*cm	Mobility $cm^2\ v^{-1}\ s^{-1}$	Carrier Conc. cm^{-3}	Carrier type
Un[b] 7280b, As[c]	4	1.0	62	19.1	n[d]	6.1	N/A	63	4500	1.7E+02	41.1	9.0E+14	n
Un 72, Ni	4	0.4	3	50.9	LS[e]	0.1	N/A	41	9515	1.2E+01	47.6	1.1E+16	n
Un 7280A, As	5	1.0	23	17.0	n	2.9	N/A	47	3280	2.6E+02	32.1	7.6E+14	n
Un 7279B, As, Ni	5	1.0	162	19.0	13.6	12.1	0.014	60	6000	1.1E+01	169.3	3.3E+15	n
Un 69-1, Ni	5	0.3	14	43.8	6.0	0.6	0.005	49	8955	4.1E+02	1.4	1.1E+16	p
Un 69-2, Ni	5	0.3	6	39.9	n	0.2	N/A	27	6173	1.8E+03	16.7	2.1E+14	n
Un 69-3, Ni	5	0.3	14	35.0	n	0.5	N/A	45	5415	7.7E+02	25.7	4.2E+15	n
Un 69-4, Ni	5	0.3	3	36.8	n	0.1	N/A	22	5039	1.1E+02	59.1	9.8E+14	n
As T91A	5	1.0	0	45.7	n	0.3	N/A	28	4500	9.4E+01	10.0	6.6E+15	n or p
As T110	5	2.0	257	24.4	11.1	6.2	0.011	78	13000	1.5E+00	102.0	5.0E+15	n
As 93C	5	3.0	6	26.2	n	0.1	N/A	25	2098	2.2E+02	8.7	3.2E+15	n
As 93	5	3.0	16	28.6	n	0.9	N/A	40	2167	5.9E+01	28.0	3.8E+15	n
Un 7286A1, As	6	1.0	2	44.9	n	0.4	N/A	35	7390	4.3E+00	40.3	3.7E+16	n
Un 7286A2, As	6	1.0	3	45.9	n	0.3	N/A	37	12700	1.6E+01	6.4	4.1E+16	n
Un 7286B1, As	6	1.0	31	38.7	n	0.7	N/A	57	10780	2.5E+00	62.4	9.9E+16	n or p
Un 7286B2, As	6	1.0	33	30.4	n	0.7	N/A	65	7410	1.4E+01	11.8	2.6E+17	n or p
Un 70, Ni	8	0.4	135	23.9	n	3.3	N/A	83	10670	7.1E+01	16.0	5.5E+15	
As 7250A	9	1.0	0	50.7	n	0.2	N/A	4	12300	2.2E+01	13.7	2.2E+16	n
As 91C	11	1.0	0	36.7	n	0.0	N/A	38	5178	9.0E+01	0.4	1.7E+17	n
As 91B	11	1.0	8	41.2	n	0.3	N/A	40	7552	8.5E+01	111.0	6.6E+14	n
Un 7229, Ni	12	1.2	366	26.2	24.2	6.0	0.036	62	17630	2.5E+00	69.0	3.6E+16	n
As 7219B	23	3.0	21	27.2	n	1.3	N/A	51	3662	2.1E+02	0.4	1.1E+17	n
As 112	35	3.0	152	28.3	8.4	2.7	0.008	82	12200	2.4E+02	18.3	1.4E+15	p
As T101A	36	2.0	78	25.8	3.2	4.1	0.003	58	6000	1.6E+01	2.0	1.0E+17	p
As 7317A	98	6.0	32	35.9	n	1.0	N/A	59	9849	3.8E+01	4.5	4.2E+16	n
As 7317B	98	6.0	34	43.8	15.0	1.1	0.016	55	11900	1.3E+01	14.1	6.2E+16	n or p
As 3A	100	3.0	381	23.7	30.2	8.1	0.061	118	14400	1.1E+00	6.1	3.0E+18	p
As 3B	100	3.0	212	24.0	38.1	5.5	0.162	88	12390	8.7E-01	6.2	3.5E+18	p
As 3C	115	4.0	176	25.0	16.8	5.8	0.019	85	13000	6.7E-01	6.3	4.1E+18	p
As T102A	132	5.0	200	14.7	n	7.9	N/A	103	5900	9.0E+00	0.8	9.0E+17	p
As 7332A	145	8.0	132	26.3	n	4.7	N/A	85	15490	6.5E+00	2.3	1.2E+18	n or p
As 7332B	145	8.0	120	31.4	n	4.9	N/A	110	16040	8.1E+00	5.9	2.7E+17	n or p
As 7326	236	29.0	132	27.7	15.0	3.6	0.016	100	12660	1.3E+00	1.9	2.8E+18	p
As 7331A	251	11.0	35	36.6	n	0.6	N/A	147	15820	3.2E+00	7.3	3.4E+18	n or p

Table 1 continued

Electrode	LA-ICPMS		AC Voltammetrey					Cyclic voltammetrey		Hall - van der Pauw measurements			
	Impurity ppm[a]	Error[f] ppm	AC peak $\mu A cm^{-2}$	Meas. φ	Corrected φ	AC Resp. score	k° $cm\ s^{-1}$	Fe^{3+} peak $\mu A\ cm^{-2}$	Anodic peak $\mu A\ cm^{-2}$	Resistivity ohm*cm	Mobility $cm^2\ v^{-1}\ s^{-1}$	Carrier Conc. cm^{-3}	Carrier type
As 7331B	251	11.0	112	33.3	n	2.7	N/A	86	13430	1.8E+00	2.9	2.8E+17	n or p
As T102B	285	20.0	176	16.1	11.9	5.0	0.012	97	7400	7.6E+00	0.8	2.4E+18	n
As 96B	356	48.0	126	16.2	7.7	7.0	0.007	88	5600	1.7E+01	2.9	1.9E+17	p
As 7327	401	22.0	45	38.8	n	0.7	N/A	79	12920	1.0E+01	2.3	6.8E+17	n
As T102C	502	39.0	140	20.2	12.0	5.3	0.012	72	6800	5.4E+00	3.5	4.0E+17	n or p
As 96A	812	97.0	62	26.9	n	2.8	N/A	67	6900	1.1E+01	0.5	1.1E+18	p
Co 7272	452	6.0	134	25.0	15.9	6.1	0.018	85	12000	3.5E-03	336.6	8.2E+18	n
Co 82	454	13.0	94	33.0	4.4	2.6	0.004	47	10390	6.4E-03	142.0	6.9E+18	n
Co 7275	481	3.0	159	25.0	24.5	1.0	0.037	85	12000	3.5E-03	122.0	1.6E+19	
Co 7236D	507	10.0	116	29.5	n	3.7	N/A	85	11500	1.8E-02	62.2	5.7E+18	n
Co 7236C	525	12.0	25	40.4	n	1.2	N/A	50	3560	7.4E-02	44.0	1.9E+18	n
Co 7228A	1406	68.0	2	54.7	n	0.0	N/A	22	10200	9.1E-03	150.2	4.6E+18	n
Co 55	1846	73.0	284	23.7	15.5	8.4	0.017	109	13390	4.9E-03	272.0	4.7E+18	n
Co 62	2225	60.0	3	56.8	6.5	0.3	0.006	37	10500	4.2E-03	159.3	9.4E+18	n
Co 7243	3057	71.0	29	43.9	n	1.0	N/A	53	12210	4.0E-03	90.0	1.7E+19	n
Ni 85B	195	6.0	0	55.0	n	0.0	N/A	44	9111	7.0E+02	47.2	1.9E+14	n
Ni 85A	195	8.0	193	22.0	n	7.9	N/A	69	8447	5.0E+00	140.0	8.9E+15	n
Ni 84A	288	6.0	31	42.8	3.6	0.8	0.003	61	10430	2.0E+02	63.4	4.9E+14	n
Ni 90B	1071	26.0	151	28.7	n	6.7	N/A	78	12000	2.2E+00	166.7	1.7E+16	n
Ni 90D	1286	77.0	14	45.0	n	0.3	N/A	54	11540	1.3E+01	113.0	1.1E+16	n
Ni 90C	1286	77.0	6	45.0	n	0.2	N/A	36	8841	3.1E+01	61.0	3.3E+15	n
Ni 90A	1500	51.0	324	24.5	15.7	10.3	0.017	84	14040	4.2E+00	111.2	1.4E+16	n
Ni 7296	2183	30.0	102	27.2	20.0	6.6	0.025	85	7300	3.2E+00	39.9	4.9E+16	n
Ni 7296B	2183	30.0	128	26.2	26.4	5.8	0.044	73	5200	3.2E+00	39.9	4.9E+16	n
Ni 7290B	2812	13.0	262	24.0	12.8	11.7	0.013	88	12750	2.0E+00	30.5	1.1E+17	n

[a]Concentrations < 50 ppm are catagorized as undoped for statistical analysis

[b]Element abbreviation in front of the the electrode number is the intended dopant

[c]Element abbreviation after the electrode number is for impurities detected if different from intended

[d]n symbolizes negative phase angles

[e]Phase angle is not reported due to very low response score

[f]Error reported at the 95% confidence level

AC and cyclic voltammetry

Pyrite with As impurity generated more current from AC voltammetry than the undoped pyrite and the other types. As-doped pyrite also had the largest fraction of electrodes with AC response scores over 1, though the Ni-doped pyrite had the highest mean AC response score. The pyrite containing Ni and Co was also more reactive than undoped pyrite in each AC proxy. Figure 4 shows the cyclic voltammograms and AC voltammetry peaks for one electrode of each type: Undoped, As-doped, Co-doped and Ni-doped. The examples were chosen because they are close to the median of each population. The CV scans were performed from 0 V to 1.1 V with the anodic dissolution beginning at approximately 0.8 V. The ferric iron reduction peak occurs on the return scan at approximately 0.44 V (Figure 4B). The AC voltammetry data consists of the AC peak current density, the measured and corrected phase angles, the AC response score, and calculated k^o values. The data from the measurements of dopant concentration, flat electrode surface area, and AC voltammetry are reported in Table 1.

The data from cyclic voltammetry and the electrical properties from van der Pauw/Hall measurements are also reported in Table 1. Again, pyrite with As impurity generated more current than the undoped pyrite and the other types. The pyrite containing Ni and Co also generated more current than undoped pyrite in both cyclic voltammetry proxies. The cyclic voltammetry data consists of the magnitude of the peak current density associated with the reduction of ferric iron after subtracting the background or nonfaradaic current and the absolute value of the peak negative current density at 1.1 V. The van der Pauw/Hall measurements include the resistivity, mobility and carrier concentration. The values should be considered approximations due to the limitations of the method as discussed in Lehner et al. (2006).

Statistical comparison of the oxidation proxies

The results from the statistical analysis of the AC and cyclic voltammetry measurements as well as the AC response score are shown in Table 2. There are four populations: Undoped, As-doped (including the Leadville, CO samples), Co-doped, and Ni-doped; and

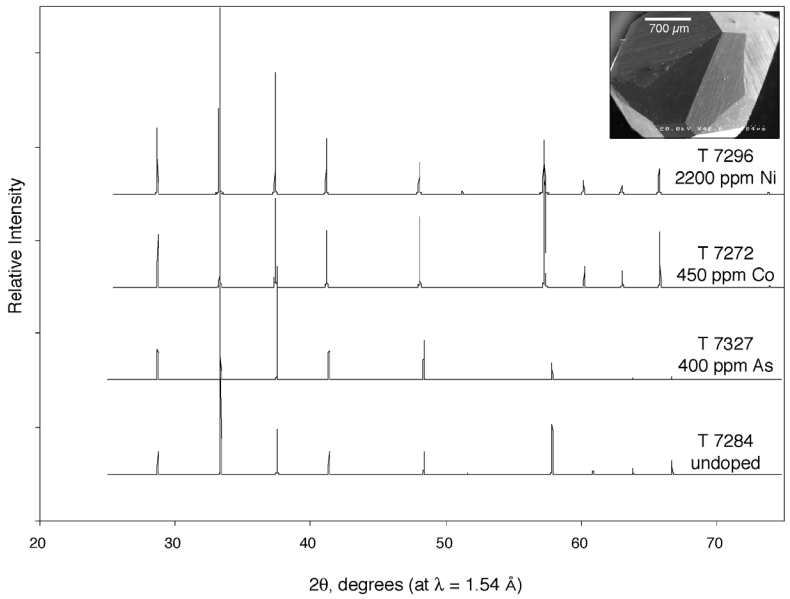

Figure 3. Synchrotron X-ray powder-diffraction patterns for selected synthetic samples, recalculated to display at λ = 1.54 Å (Cu-kα, see methods). Crystallinity is indicated by the flat background and sharp peaks. Inset shows SEM backscattered electron image of a synthetic pyrite crystal doped with Ni.

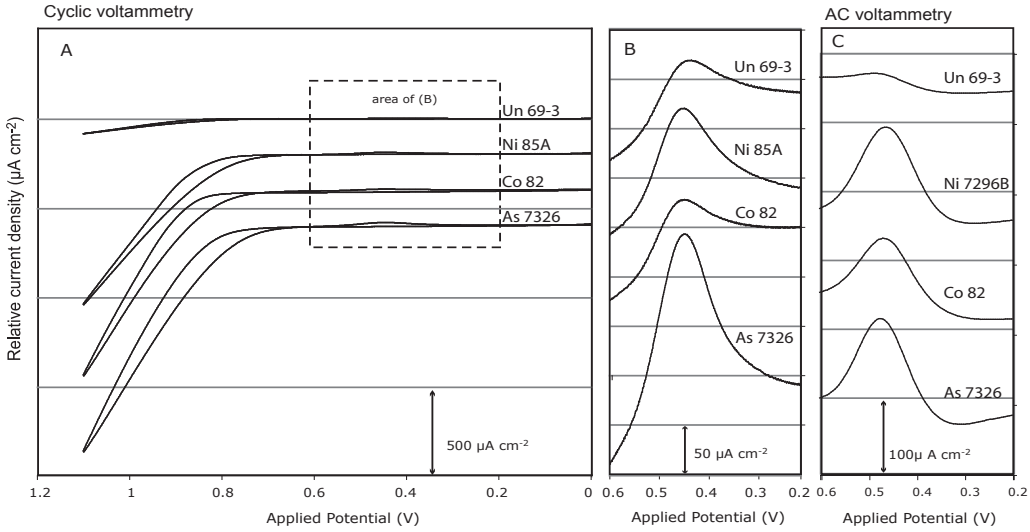

Figure 4. Representative cyclic and AC voltammetry scans in pH 1.78 H_2SO_4 solution containing 1 mM ferric iron added as $FeCl_3$. Peak values for examples shown are close to the median for electrodes of each type. (A) CV scans showing relative value of anodic peak at 1.1V. The box is the potential region of ferric iron reduction. (B) Ferric iron reduction peaks from CV scans in (A.) (C) Median ferric iron reduction peaks from AC voltammetry.

five datasets: k^o (the standard heterogeneous rate constant), AC peak current, CV ferric iron reduction peak current, anodic dissolution current at 1.1V and the AC response score. Of the resulting 20 measurement populations, 5 failed the Shapiro Wilk normality test at the 95 % confidence level. They were the As-doped population for k^o, the Co-doped population for the anodic dissolution at 1.1 V, both the As-doped and undoped populations for the AC voltammetry current peak and the undoped population for AC response score.

For each of the four pyrite oxidation proxies plus the AC response score there are 6 ways to pair the four electrode types. The statistical comparisons were done with both parametric and nonparametric techniques (Figure 5); the two sample T-test and the Wilcoxon signed rank test. The Wilcoxon results are presented in Table 2. Only 3 of the resulting 30 population pairs failed the F-test for equal variances at the 95% confidence level. The failures resulted from large values for k^o in two of the three the Leadville, CO samples.

The mean values for the standard heterogeneous rate constant k^o were somewhat higher for As-doped pyrite than for Ni-doped, Co-doped or undoped pyrite though not at the 95% confidence level. The mean AC peak current for As-doped, Ni-doped, and Co-doped pyrite was higher than the mean AC peak current for the undoped pyrite at 99, 95, and 90% confidence levels respectively. The mean ferric iron reduction peak current from cyclic voltammetry for As-doped, Ni-doped, and Co-doped pyrite was higher than the mean current for the undoped pyrite at 99, 96, and 88% confidence levels respectively. The mean anodic current from cyclic voltammetry at 1.1 V for As-doped, Ni-doped, and Co-doped pyrite was higher than the mean current for the undoped at 99, 99, and 95% confidence levels respectively. The Co-doped and Ni-doped pyrite responses were statistically equal at the 95% confidence level. However, the Co-doped electrodes averaged higher current for the anodic dissolution in the cyclic voltammetry at 1.1 V and the Ni-doped mean was higher for the AC response score. As-doped pyrite had the highest fraction of AC responsive electrodes (AC response score over 1) at 0.81 followed by Co-doped (0.78), Ni-doped (0.60) and undoped pyrite (0.38). More Co-doped than Ni-doped electrodes scored over 1 but the Ni-doped electrodes had higher mean and variance.

Potential step experiments

The average value of the transfer coefficient, calculated from the anodic Tafel slopes obtained from potential step experiments, $\alpha = 0.57$ is close to 0.5, in agreement with Holmes and Crundwell (2000). The current density generated from stepped potentials defining the Tafel slopes for the synthetic pyrite with As was higher than the other types (Figure 6). Furthermore, the current density increased with As concentration for the synthetic pyrite electrodes with over approximately 100 ppm As, a trend not clearly observed for As or any other dopant in the oxidation proxies. The Leadville samples used in the potential step experiments had concentrations of ~ 100 ppm As and generated current densities near the Ni and Co-doped electrodes in Figure 6.

Comparison of electrochemical proxies with bulk electrical properties

The magnitude of the CV ferric iron reduction peak is moderately correlated with the log carrier concentration from the Hall and van der Pauw measurements for the As-doped and Ni-doped pyrite (($R^2 = 0.53$ and 0.54 respectively; Table 3). There is also a moderate correlation between the log carrier concentration and the anodic peak for the Co-doped pyrite ($R^2 = 0.50$). A higher correlation is found between the log resistivity and anodic peak for Co-doped pyrite ($R^2 = 0.73$). Log resistivity is also moderately correlated with the CV ferric iron reduction peak for Ni-doped pyrite ($R^2 = 0.57$).

Relationships among the current peaks from AC and cyclic voltammetry

The peak current density from the AC voltammetry is well correlated with the CV ferric iron reduction peak magnitude for the undoped, Ni-doped and Co-doped pyrite (R^2 values of 0.68, 0.81, and 0.92 respectively; Table 4). There is a looser correlation between these proxies for the As-doped pyrite ($R^2 = 0.48$). The CV anodic peak is also correlated with the AC peak for the undoped pyrite ($R^2 = 0.68$) but this correlation is looser for the Ni-doped and Co-doped pyrite ($R^2 = 0.48$ and 0.54, respectively) while there is no correlation between AC peak and the anodic peak for the As-doped pyrite. The R^2 value for the correlation between CV

Table 2. Results of the Wilcoxon signed rank test

Comparison	k^o	AC Fe(III) peak	CV Fe(III) peak	CV anodic peak	AC resp. score
As/Un	0.89 >	0.99 >	1.00 >	1.00 >	0.94 >
As/Co	0.94 >	0.85 >	0.96 >	0.90 >	0.88 >
As/Ni	0.84 >	0.75 >	0.99 >	0.95 >	0.70 =
Co/Un	1.00 =	0.90 >	0.88 >	0.95 >	0.65 =
Co/Ni	0.81 =	1.00 =	0.91 =	0.82 >	0.85 <
Ni/Un	0.84 >	0.95 >	0.96 >	0.99 >	0.84 >

Values represent the confidence level of the hypothesis represented by the mathematical symbol being applied to the pair in place of the slash; As is As-doped pyrite (etc.)

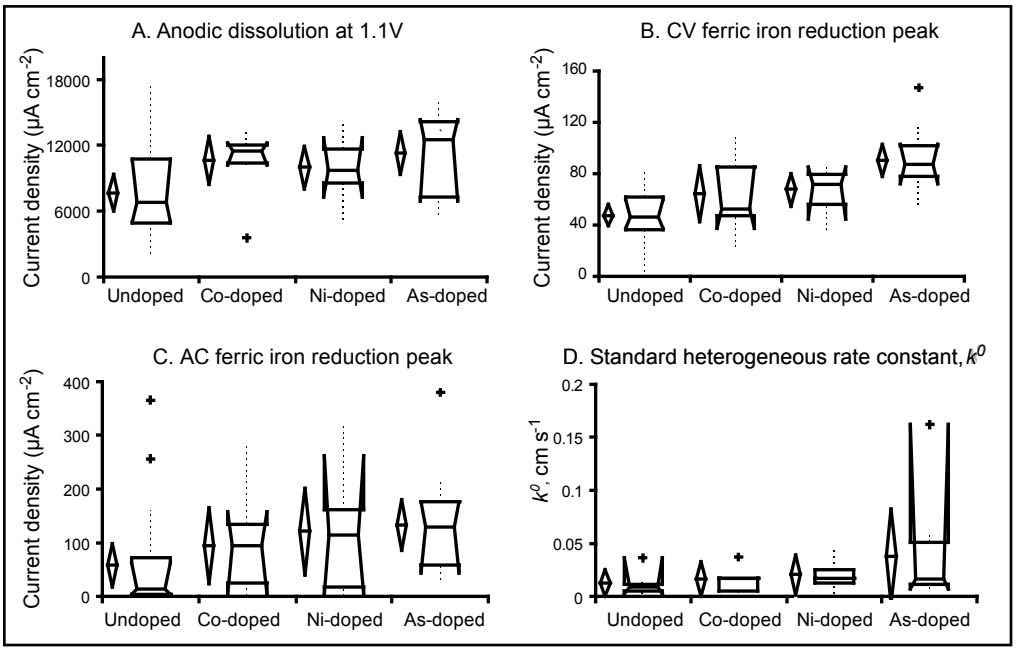

Figure 5. Results from the statistical analysis for the four proxies for pyrite oxidation. For the box and whisker plots the notch represents the 95% confidence interval and the top and bottom represent the interquartile range (IQR) for the median from non-parametric statistics. The dotted lines represent the nearest observations within 1.5 IQRs. The diamond shows the 95% confidence interval for the mean from parametric statistics. Pluses are outliers.

peak anodic current and the CV ferric iron reduction peak magnitude is near 0.5 for undoped and Co-doped pyrite but not significant for As and Ni-doped pyrite.

For electrodes that do not generate much CV ferric iron reduction current, the shape of the peak is often different. In addition to being lower, it is very broad and poorly defined.

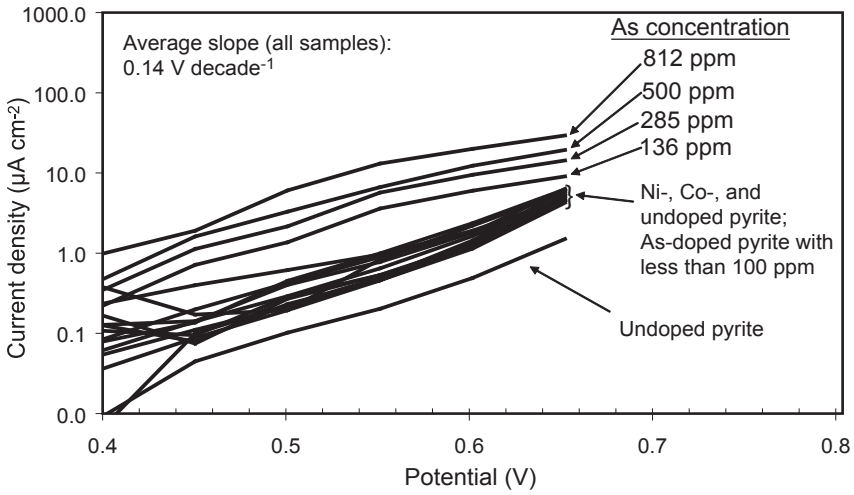

Figure 6. Tafel slopes for anodic oxidation of pyrite in 0.005 M H_2SO_4 solution, pH 2, with no added iron, from potential step experiments. Tafel slopes are ~ 1.4 V decade^{-1}; $\alpha \approx 0.57$

Table 3. Correlations between bulk electronic properties and electrochemical proxies (R^2).

Parameter	Type	Log (carrier conc.)	Log (resistivity)	Log (mobility)
AC Fe red. peak	As	0.36	0.39	0.02
	Ni	0.37	0.48	0.02
	Co	0.00	0.09	0.22
	Un	0.13	0.24	0.12
CV Fe red. peak	As	0.53	0.26	0.04
	Ni	0.54	0.57	0.00
	Co	0.01	0.04	0.08
	Un	0.00	0.11	0.02
CV anodic peak	As	0.03	0.17	0.32
	Ni	0.00	0.01	0.15
	Co	0.50	0.73	0.42
	Un	0.05	0.31	0.07

Table 4. Correlations between electrochemical proxies (R^2).

Parameter	Type	CV Fe red. Peak	AC Fe red. peak
CV anodic peak	As	0.25	0
	Ni	0.23	0.44
	Co	0.47	0.54
	Un	0.53	0.68
CV Fe red. Peak	As		0.48
	Ni		0.81
	Co		0.92
	Un		0.68

Usually these electrodes respond with low AC current to the AC voltage as well. This was more often the case for undoped pyrite.

Discussion

As-, Co- and Ni-doped pyrite produce more current from the electrochemical reactions than undoped pyrite; As-doped pyrite is the most reactive. Two proposed explanations are discussed below:

As-doped pyrite has higher relative reactivity because it has p-type conductivity and is susceptible to corrosion by holes. Evidence comes from the response to anodic polarization.

Bulk defect states arising from impurities in pyrite increase occupied surface state density, resulting in increased reactivity. Evidence for surface state density being linked to impurities and reactivity comes from the electrochemical etching necessary to activate the pyrite electrodes, comparisons of the behavior of As, Ni and Co-doped electrodes in light of the work previously done on their bulk properties, the correlation of Hall measurements with electrochemical response, the relative AC response and the correction of the AC phase angles.

Anodic current at 1.1 V vs. anodic dissolution from potential step experiments: Evidence for corrosion by holes

The anodic dissolution reaction is forced at the positive potential of 1.1 V where it is energetically favorable for pyrite to collect electrons from the solution. Holes are injected at the exposed pyrite surface where they combine with electrons and bonds are broken in a process known as corrosion by holes (Morrison, 1980) or dissolution. The dissolution reaction, requiring water (Wei and OsseoAsare, 1997), occurs at the electrode/solution interface, and releases sulfate and ferrous iron into solution (Reaction 3). The ease of electron or hole transport through the pyrite may influence the magnitude of the current produced. Co-doped pyrite has higher conductivity, carrier mobility and concentration than the other pyrite types, and it produces higher current density at 1.1 V than Ni-doped pyrite. The high electron mobility and low resistivity in Co-doped pyrite must facilitate the forced injection of holes at the surface.

The low resistivity does not appear to have as much effect on the response of Co-doped pyrite in the ferric iron reduction proxies (0.4-0.5V).

Since extreme polarization is not found in natural systems, one might question this reaction as a proxy for pyrite oxidation. However, even for this proxy, the As-doped pyrite has higher current density than all the other types. This could be because the majority carriers for As-doped pyrite tend to be holes (Table 1). Holes travel by displacing electrons; as they reach the pyrite surface they displace the bonding electrons, thereby oxidizing S and enhancing the forced injection of holes at 1.1 V. The partially oxidized sulfur ions are thought to react with H_2O (Reedy et al., 1991) and are eventually released as sulfate into solution along with ferrous iron (Reaction 3).

The potential step measurements used to define the Tafel slopes are collected at more modest potentials, 0.65 to 0.4 V, where the anodic dissolution (Reaction 3) occurs (Holmes and Crundwell, 2000) without electrochemically forced production of holes. In this potential range, the pyrite with As impurity above 100 ppm generated more current than the Co-doped, Ni-doped or undoped pyrite which clustered at about the same level (Figure 6). This is further evidence that p-type conductivity of As-doped pyrite may influence oxidation rates. In the potential region of 0.6 to 0.4 V only the As-doped pyrite produces significantly more current density because it is rich in holes that are able to reach the electrode surface and break bonds.

Reactivity, surface state density and impurities

Evidence from electrochemical etching of the electrodes

Most pyrite electrodes must be electrochemically etched in order to react quasi-reversibly with ferric iron in solution. Without this etching the electrodes did not respond to the ferric iron in the pH 1.78 H_2SO_4 solution with 1mM ferric iron when the potential was scanned from 0.7 to 0.2 V with CV or AC voltammetry. The etching consists of the anodic dissolution from the CV sweep to 1.1 V, after which the ferric iron reduction peak occurs at approximately

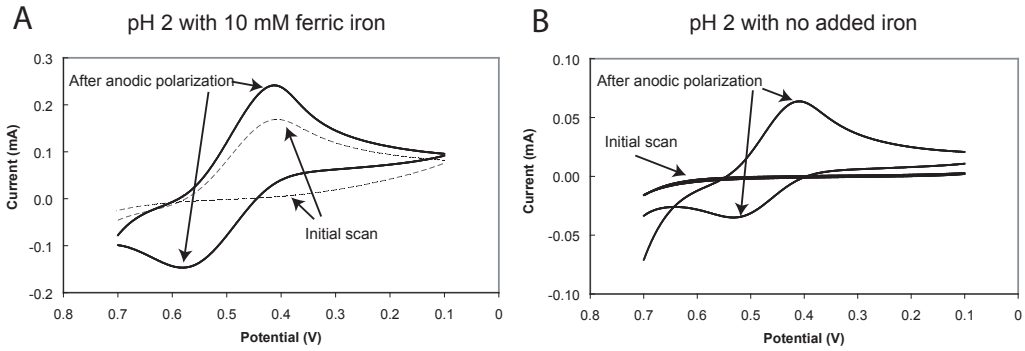

Figure 7. CV scans showing the effect of anodic polarization to 1.1 V in H_2SO_4 solution at pH 2 (A) containing 10 mM ferric iron added as $FeCl_3$ and (B) no added iron.

0.44 V in the return cathodic scan. If rescanned anodically, a ferrous iron oxidation peak, which is smaller in magnitude than the ferric iron reduction peak, occurs at approximately 0.6 V, indicating a quasi-reversible reaction (Figure 7). At the potential of 1.1 V, Reaction 3 (anodic dissolution) is forced. A portion of the surface is dissolved leaving a faint auburn to blue tarnish, possibly caused by the buildup of adsorbed ferrous iron or sulfate (Figure 8). Ferrous iron on the pyrite surface could be a source of electrons for the ferric iron reduction. However, the situation is likely more complicated.

For example, specific reaction sites such as kinks and steps that are likely to emerge during electrochemical etching promote the reduction of ferric iron. Seeliger et al. (1995) report results suggesting site-specific interaction with pyrite for the Fe^{3+}/Fe^{2+} couple: the adsorption of organic ligands results in a significant decrease in current for a Fe^{3+}/Fe^{2+} electrolyte but only

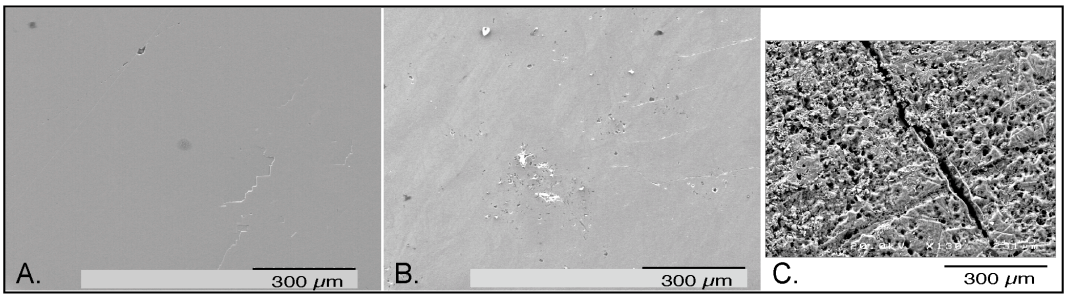

Figure 8. Scanning electron microscope images of (A) Electrode 3B after polishing; (B) Electrode 3B after anodic dissolution to 1.1V and AC voltammetry scan in H_2SO_4 solution at pH 1.78 containing 1 mM ferric iron added as $FeCl_3$; and C. Electrode 3C after applied potential was held at 1.1V for 30 minutes in 1M H_2SO_4 containing 6ppm ferric iron.

minor decrease for an I^- electrolyte. Buker et al. (1994) report that cathodic etching of polished pyrite electrodes, in contrast to the anodic etching in this study, neutralizes mechanically introduced defect states by diffusion of hydrogen into the bulk leading to a dramatic decrease in anodic current. Buker et al. (1996) found higher stored charge and corrosion for pyrite {111} surfaces than for {100} surfaces. This suggests that an increase in {111} surfaces may promote pyrite corrosion; anodic polarization may initiate the process by producing more surface texture.

The electrochemical dissolution of the surface (Figure 8) probably increases the number of defects, resulting in a higher density of surface states and electrons within the bandgap. Evidence for increased surface states after anodic polarization comes from cathodic Tafel slopes measured before and after anodic polarization for two Ni-doped electrodes. The transfer coefficient before the anodic polarization to 1.1 V was approximately $\alpha = 0.2$, indicating semi-conducting behavior (Morrison, 1980), while after the anodic dissolution the value was approximately 0.5 as for a metal. It is also possible that the anodic dissolution is removing a charge transfer-inhibiting oxide coating gained during the polishing procedure.

There is evidence that additional ferric iron is released from the pyrite to the solution after anodic polarization. CV oxidation and reduction peaks for iron were observed with no added iron in a pH 2 solution after three successive anodic polarizations to 1.1 V. The iron must come from the electrode. The 0.15 V separation of the peaks (Figure 7) for the iron couple indicates diffusion and that the species are in solution. However, the ferric iron reduction peak also occurs for freshly polished electrodes in some AC voltammetry scans in KCl solution without added iron, indicating that ferric iron derived from the crystal surface may also be reduced after the anodic polarization. For other electrodes, the AC ferric iron reduction peak is never seen.

Evidence for surface states from the AC response

The current response from small-amplitude alternating voltage (AC voltammetry) gives information on the capacitive and resistive components of the impedance inherent in the

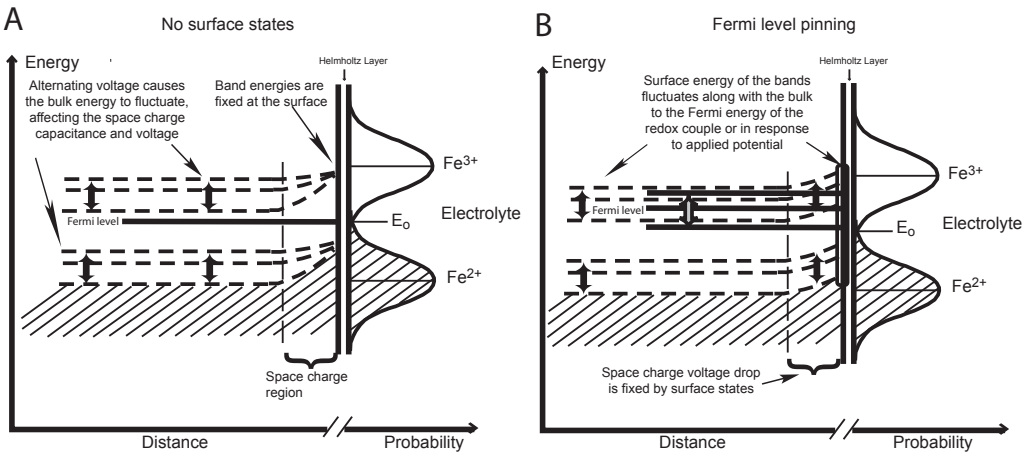

Figure 9. Gerischer model diagrams showing the difference in response to applied alternating potential when surface state density leads to Fermi level pinning. (A) No Fermi level pinning, low surface state density. (B) Fermi level pinning, high surface state density.

charge transfer reaction. The magnitude or lack of response to this sinusoidal voltage is in itself revealing. Why do some pyrite electrodes of each type respond very well to the AC experiment and others do not? While one possibility is that adsorption of organic molecules from epoxy which may have reacted with the acid cleaning etch may passivate some electrodes (Buker et al., 1996; Seeliger et al., 1995), the differences in the mean AC current peak among the different populations suggests another mechanism. Transfer of electrons from an intrinsic semiconductor to aqueous species is dependent on the relative energy levels of charge carriers in the semiconductor and acceptor orbitals in the oxidant. In order for the electron transfer to occur, it is thought that the orbital energy of the accepting species in solution must be the same or slightly lower than the energy of the electron in the semiconductor (Morrison, 1980). In the absence of surface states, the redox couple in solution may be in an unfavorable energy position with respect to the band gap and/or the space charge potential barrier is high.

When electrodes do respond to the AC signal it may be due to an abundance of surface states within the band gap leading to a metallic behavior. Metals have no forbidden zone or band gap and so electrons are free to equilibrate with the energy levels of the redox couple in solution. The Fermi level then is pinned by the energy levels of the solution redox couple (Bard

et al., 1980). It is possible that the magnitude of the AC response is sensitive to the density of surface states and may be an indicator of Fermi level pinning (Figure 9). If so the AC response score from Table 1 could be considered a proxy for high surface state density and possible Fermi level pinning. Surface states can exist as a result of impurities but, as noted above, also from other defects and lattice discontinuation.

Deep defect states of Ni and As suggest a connection between impurities and intra-band gap surface states

Our hypothesis explaining how bulk defect states result in increased surface state density is illustrated in Figure 10, the type of diagram typically used to conceptualize the semiconductor/electrolyte interface, based on the Gerischer Model (Gerischer, 1961). Energy is shown on the ordinate while the abscissa is split between distance on the semiconductor side (left) and the probability distribution of the density of states for the redox couple in solution (right). The top distribution represents ferric iron and the bottom represents ferrous iron. The probability distribution reflects fluctuating orbital energy levels as the ions react to polarized water molecules.

On the semiconductor side of the diagram, the band gap is bordered by horizontal lines representing the top of the valence band and the bottom of the conduction band, at their respective energy levels. The shaded regions represent bulk defect states introduced by the impurities according to our current understanding. Surface states within the band gap are represented by the rounded rectangles. The space charge region, where the bands bend, results from the exchange of electrons with the solution or from surface effects. The space charge region is depicted as smaller for Co, Ni, and As-doped pyrite due to surface state capacitance. The amount of bending represents a change in potential energy or voltage drop and it is a function of the electronic equilibrium between the bulk and interface. It is an energy barrier for charge transfer from the conduction band in the case of n-type conductivity.

The four Gerischer diagrams in Figure 10 all portray the situation of no applied potential, and the Fermi level is defined by the equilibrium of the redox couple. For the undoped

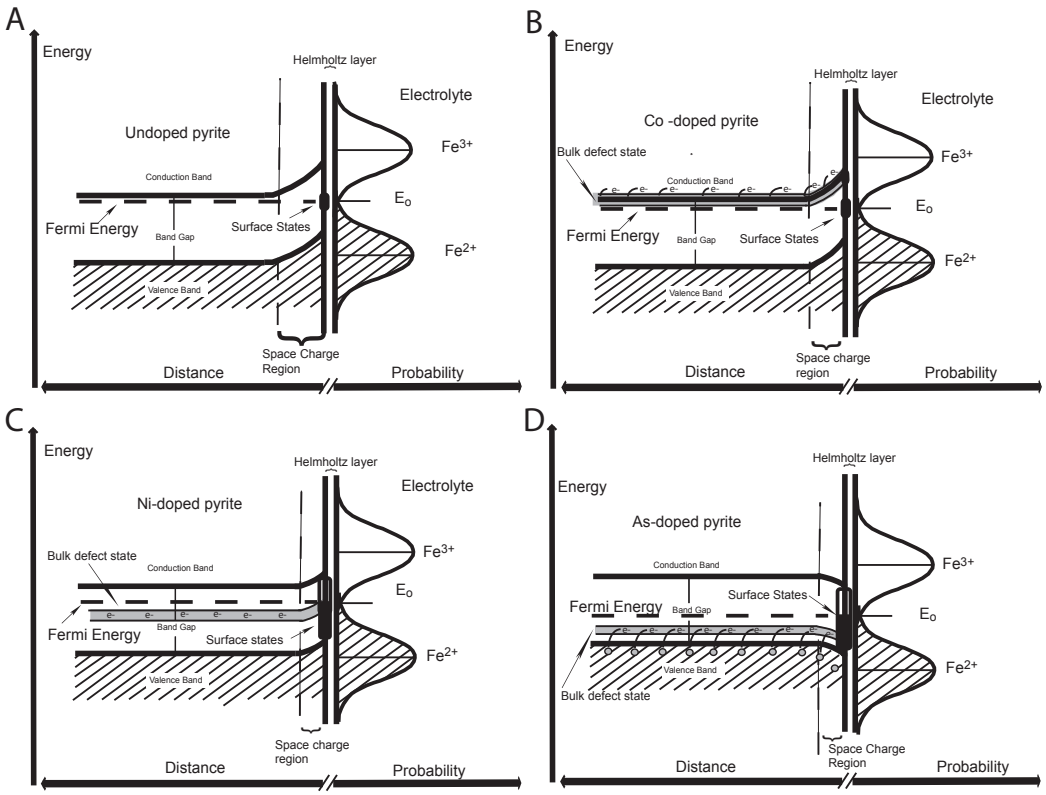

Figure 10. Gerischer model diagrams for proposed mechanism by which bulk defect states from impurities result in higher surface state density. (A) Undoped pyrite has low surface state density from mechanical defects. The space charge depletion region is deep, the potential barrier is high and there are few carriers available. Limited charge transfer can occur via the surface states (B) Co-doped pyrite has a defect state high in the bandgap overlapping the conduction band. Electrons are delocalized and free to move in response to an electric field. There is still a significant potential barrier; the extra surface states are so high in the band gap that they mirror the conduction band. Charge transfer can occur from the conduction band and through surface states. (C) The Ni-doped defect state is portrayed in the middle of the band gap. Due to the high density of surface states the space charge potential will remain constant despite applied potential as the band energies at the surface are free to move. Charge transfer can occur through surface states when applied potential raises the surface/bulk energy. (D) As-doped pyrite has a defect state low in the bandgap which is easily populated by thermally activated electrons. The bands bend down because the resulting charge carriers are positive (holes) and the depletion layer is negative in relation to the bulk. Like Ni-doped pyrite, the space charge potential will remain constant despite applied potential as the band energies at the surface are free to move and charge transfer can occur via surface states.

pyrite (Fig. 10A), the bands bend in response to the potential of the redox couple changing position with respect to the Fermi level while the band energy at the surface is fixed. The more the bands are bent, the larger the potential barrier for charge transfer from the conduction band. For As and Ni (Figs. 10C and 10D, respectively) the band bending is due to surface states

which are dense enough to control the electronic equilibrium with the bulk. Under these circumstances the Fermi level is pinned with respect to the band energies because the band energies at the surface are free to migrate to the potential of the redox couple. They also can migrate in response to applied potential (Figure 9) and the charge transfer potential barrier from the surface region is constant. Therefore they are much more likely to respond to small potential changes associated with AC voltammetry. The Co-doped electrode is depicted in a state where it is unclear if the Fermi level is pinned. Figure 1 depicts a possible equivalent circuit that could be used to model the impedance measured by AC voltammetry. The circuit inside the dashed line corresponds to the pyrite side of the Gerischer diagrams.

Impurities may increase the reactivity of pyrite by introducing bulk defect states deep within the forbidden zone that, at the pyrite surface, increase the density of occupied surface states within the bandgap energy. Evidence for this can be seen in the respective behavior of Co- and Ni-doped pyrite. Electron paramagnetic resonance studies (Chandler and Bene, 1973) suggest that Ni and Co substituting for Fe in the pyrite structure introduce defect states at different energy levels within the forbidden zone. The Co defect state occurs high in the band gap near or possibly overlapping the conduction band energy so that the extra electrons easily move into the conduction band, leaving the defect states empty (Figure 10B). This is reflected in the high mobility, high carrier concentration, and low resistivity of Co-doped pyrite. The Ni defect state occurs somewhere in the middle of the band gap where it is energetically unfavorable for the electrons to enter the conduction band (Figure 10C). The Ni defect states are most likely filled due to their distance from the conduction band and this is reflected in low carrier concentration measured for Ni-doped pyrite. When these defect states intersect with the surface they become surface states. Therefore, we would expect to see higher intra-band gap occupied surface state density in the Ni-doped pyrite. If the AC response is an indicator of occupied surface state density then we would expect higher AC response scores for the Ni-doped compared to the Co-doped pyrite. We observe that trend for the means (Table 2); however, the fraction of electrodes with scores over 1 is less for Ni-doped than for Co-doped electrodes and

there is more variability.

In the case of As substituting for S, a defect state introduced low in the band gap may become populated by valence band electrons, leaving holes for charge carriers (Moller and Kersten, 1994). At the pyrite surface these bulk defect states may also introduce additional occupied surface states within the band gap (Figure 10D). We should expect to see higher AC response scores if this were the case. We do observe the mean AC response score to be higher for As-doped than undoped and Co-doped pyrite and roughly equal to Ni-doped pyrite (Table 2) while the fraction of As-doped electrodes with response scores over 1 is highest, at 0.81.

Correlation of electrochemical reactivity and bulk electrical properties

Further evidence that Ni and As impurity may be related to increased reactivity through occupied surface states is that bulk carrier concentration is moderately correlated to the CV ferric iron reduction peak magnitude for Ni-doped and As-doped pyrite but not for Co-doped pyrite (Table 3). This is what we would expect if their carriers were helping to populate the bandgap at the surface. The Co-doped charge carriers are in the conduction band, where they are correlated with the forced anodic dissolution at 1.1 V as discussed above, but not with the surface-state-sensitive CV reduction of ferric iron.

Bulk resistivity is moderately correlated to the AC ferric iron reduction peak for As and Ni but not for Co-doped pyrite (Table 3). Resistivity is a function of carrier concentration and mobility. In the case of Ni-doped pyrite, carrier concentration is similar to undoped pyrite due to the deep levels of the defect state but the mobility is enhanced (Lehner et al., 2006; Tomm et al., 1995). While the lower resistivity for Ni-doped pyrite is due mostly to increased mobility, lower resistivity for As-doped pyrite is due to increased carrier concentration. In both cases, lower resistivity is an indication of higher bulk defect and hence surface state density. Although the resistivity is much lower for Co-doped pyrite than either Ni-doped or As-doped pyrite (Table 1) it is not correlated to increased charge transfer at the solution interface for ferric iron reduction. The Co defect state, while dramatically lowering pyrite resistivity, does

not increase the intra-band gap surface state density and hence Co-doped resistivity does not correlate to the AC ferric iron reduction peak magnitude.

Evidence from AC voltammetry phase angles and nonfaradaic capacitance

For AC voltammetry on pyrite, the measured phase angle (φ) values for the electrodes with the smallest response are usually between 45 and 60 degrees (Table 1). The large measured values for (φ) when the AC current magnitude is low suggest there is small space-charge/surface-state capacitance. If the space charge capacitance is very small and there is little surface state capacitance, the capacitive reactance will cause the imaginary component of the impedance vector to equal or dominate the resistance vector even though there may also be significant charge transfer resistance. In this case (φ) is no longer defined by only the charge transfer resistance and measured phase angles are not proportional to k^o. The measured phase angles need to be corrected for the non-faradaic capacitance associated with the Helmholtz layer, the space charge region and surface states as well as for the solution resistance. We obtained the nonfaradaic capacitance by measuring the capacitance of the pyrite electrode in the absence of the redox couple in an electrolyte solution of 0.1 M KCl.

Two problems arise for semiconducting electrodes when attempting to correct for non-faradaic capacitance and resistance with a series equivalent circuit (see Methods). One is that the resistance of the electrode, which may be a function of the electrode connection, the material itself or the surface region, behaves as uncompensated solution resistance (Bard and Faulkner, 2001). The other is that accurate measurement of the nonfaradaic capacitance may be difficult since the space charge and surface state capacitance are in parallel and occur in series with the Helmholtz capacitance (Figure 1) (Bard et al., 1980; Morrison, 1980). Adsorption of either electroactive or inactive species at the pyrite/solution interface result in further complication in that the capacitance in the absence of the solution redox couple may be different from the nonfaradaic capacitance in the presence of the couple in solution and thus impossible to measure. If these problems lead to overestimating the non-faradaic capacitance

or underestimating nonfaradaic resistance the result is a meaningless negative phase angle after applying the correction.

An accurate equivalent circuit model is needed to understand both the non-faradaic and faradaic impedance measurements. Figure 1 is an example of possible circuit elements that can lead to misinterpretation. This equivalent circuit can usually be simplified with the following assumptions: The Helmholtz capacitance can be ignored since it is large, and added in series; the contact is ohmic and the impedance negligible, the bulk sample should have little impedance except for near the surface, and there is no adsorption or oxidation impedance at the surface. Then the equivalent circuit may resemble the circuit inside the dashed line of Figure 1.

What is measured in the KCl solution with AC voltammetry is the effective non-faradaic impedance. Taking the equivalent circuit inside the dashed line of Figure 1 as a plausible model for a pyrite surface, the effective non-faradaic capacitance is given by (Morrison, 1980):

$$C_{eff} = C_{sc} + \frac{C_s}{\left(1 + \omega^2 R_s^2 C_s^2\right)} \tag{8}$$

where C_{eff} is the effective or measured non-faradaic capacitance, C_{sc} is the space charge capacitance, C_{ss} is the surface state capacitance, R_{ss} is the surface state resistance and ω is the angular frequency. In this model both the space charge and surface state impedances are a capacitance and resistance in series, however the resistive component of the space charge impedance, not seen in the equation, is equal to the effective or measured resistive component of the impedance (Morrison, 1980). This equation when applied to the data with reasonable estimates of C_{sc} and R_{ss} suggests a plausible explanation for the negative phase angles. As C_{ss} increases and R_{ss} decreases, C_{eff} plotted against the C_{ss} first rises with a slope of ~ 1 and then becomes flat in the range of values generated from the data. For small surface state capacitance the measured capacitance is nearly equal to the space charge capacitance. At larger values of C_{ss}, as R_{ss} decreas-

es, the slope flattens and C_{eff} is less affected. Therefore the non-faradaic capacitance is likely to be underestimated rather than over estimated. The magnitude of C_{eff} and C_{ss} at which the slope begins to flatten is dependent on the surface state resistance.

This equation was solved iteratively using a value of 1 μF for the C_{sc} and using both 50% and 110% of the measured resistive component of the impedance for R_{ss}. For the smaller values of R_{ss} the equation converged on a value for C_{ss} in all but two cases. For the larger R_{ss} values the equation converged 46% of the time for the population of negative phase angle corrections and 75% of the time for positive phase angle corrections. The average surface state capacitance calculated this way was higher in both cases for the electrodes with positive corrected phase angle and within that group it was higher for electrodes with impurities. The average measured resistive component of the impedance in KCl solution was less for the group of electrodes with positive phase angle corrections. This suggests that lower resistive component of the space charge impedance might be related to high surface state concentration as expected (Morrison, 1980).

The resistive component of the impedance measured in the pH 1.78 H_2SO_4 solution was also lower for the electrodes with successful phase angle corrections by about the same amount as that measured in the KCl solution. Analysis of the phase angle correction calculation suggests an underestimation of the non-faradaic resistance can result in negative phase angles. It may be that when the surface state capacitance is large, the nonfaradaic resistance associated with the pyrite electrode is small and subtracting the solution resistance produces accurate results. When the surface state capacitance is small, even though it may be measured accurately, the space charge resistance or some unknown circuit element resistance is large and needs to be subtracted from the faradaic resistance.

Of the 59 electrodes included in this study, it was possible to obtain meaningful phase angle measurements for 24. The other electrodes yielded negative values for the phase angle after subtracting the measured non-faradaic impedance. The fraction of electrodes with AC response scores over one that were successfully corrected was 0.59 while for those with scores less

then one the fraction successfully corrected was only 0.16. If meaningful phase angle corrections suggest that the solution resistance is the only non-faradaic resistance, which is likely the case when there is a high density of surface states, and the corrected phase angles correspond better to electrodes with high AC response, this suggests that the AC response may be related to large surface state capacitance and density. If we assume that As, Co, and Ni impurities do introduce surface states and that a meaningful phase angle correction is an indication of high surface state density, we should see a trend in the fraction of each type of electrode with positive phase angles. The fractions from Table 1 for positive phase angles are 0.69 for As-doped electrodes, 0.56 for Co-doped electrodes, 0.50 for Ni-doped electrodes and 0.25 for undoped electrodes. These results suggest further investigation is warranted.

In the present study the focus was on comparing many electrodes of each type and thus a representative frequency for AC voltammetry (100 Hz) was chosen. It is possible, however, to calculate k^o from curves defined by the frequency dependence of the peak AC current to background current ratio without the need for the phase angle (Creager and Wooster, 1998). To further investigate the correlation between dopant type and surface state density, analysis of the frequency dependence of the current and capacitance response from AC voltammetry and the development of an equivalent circuit from electrochemical impedance spectroscopy should be undertaken. Then electrochemical photocapacitance spectroscopy could be used to describe the bulk and surface defect energy levels. The combination of these techniques should provide a more accurate model of charge transfer mechanisms at doped pyrite electrodes.

Conclusions

In sulfuric acid solution at pH 1.78 with added ferric iron in the presence of oxygen, pyrite with impurities generates more current from the electrochemical half reactions: the reduction of ferric iron (Reaction 4) and the anodic dissolution of pyrite (Reaction 3). Pyrite containing As impurity is more reactive than pyrite containing little or no impurities. Pyrite with As is also more reactive than pyrite with either Ni or Co in the same solution. Pyrite contain-

ing the lowest impurities (undoped) is least reactive. Higher current response from pyrite with impurities to ferric iron reduction in the AC and cyclic voltammetry suggests that increased reactivity may be due to bulk defect levels within the band gap resulting in higher density of occupied surface states at the solid/solution interface, Fermi level pinning, and metallic behavior. The increased reactivity of As-doped pyrite may be related its p-type conductivity and corrosion by holes.

Acknowledgements

This manuscript benefitted from the comments of three anonymous reviewers. We thank Leonard Feldman (Vanderbilt University Physics Department) for use of the Hall effect equipment. We are grateful to John Ayers and Peixin He of CH Instruments, Inc. for helpful discussion, and to Daniela Stefan for her assistance with pyrite synthesis and for providing the Leadville, CO thick sections. We appreciate assistance from Alan Wiseman (Vanderbilt University Dept. of Earth and Environmental Sciences) with the SEM. We thank Sankaran Mahadevan for support through NSF-DGE 0114329 (Integrative Graduate Education and Research Traineeship for Reliability and Risk Engineering Management (Vanderbilt University Department of Civil and Environmental Engineering). This study was supported by NSF-EAR 0409155 and 0617396 (KSS). Portions of the research were carried out at the Stanford Synchrotron Radiation Laboratory, a national user facility operated by Stanford University on behalf of the U.S. Department of Energy, Office of Basic Energy Sciences.

References

Abraitis P. K., Pattrick R. A. D., and Vaughan D. J. (2004) Variations in the compositional, textural and electrical properties of natural pyrite: a review. *International Journal of Mineral Processing* **74**(1-4), 41-59.

Bard A. J., Bocarsley A. B., Fan F. R., Walton E. G., and Wrighton M. S. (1980) The Concept of Fermi Level Pinning at Semiconductor/Liquid Junctions. Consequences for Energy Conversion Efficiency and Selection of Useful Solution Redox Couples in Solar Devices. *Journal of the American Chemical Society* **102**(11), 3671-3677.

Bard A. J. and Faulkner L. R. (1980) *Electrochemical Methods: Fundamentals and Applications*. Wiley.

Bard A. J. and Faulkner L. R. (2001) *Electrochemical Methods: Fundamentals and Applications 2nd Edition*. John Wiley and Sons Inc.

Becker U., Rosso K. M., and Hochella J., Michael F. (2001) The proximity effect on semiconducting mineral surfaces: a new aspect of mineral surface reactivity and surface complexation theory? *Geochimica et Cosmochimica Acta* **65**(16), 2641-2649.

Biegler T. and Swift D. A. (1979) Anodic behavior of pyrite in acid solutions. *Electrochimica Acta* **24**, 415-420.

Bither T. A., Bouchard R. J., Cloud W. H., Donohue P. C., and Siemons W. J. (1968) Transition metal pyrite dichalcogenides, high-pressure synthesis and correlation of properties. *Inorganic Chemistry* **7**, 2208-2220.

Breyer B. and Bauer H. H. (1963) *Alternating current polarography and tensammetry*. Interscience Publishers.

Bronold M., Tomm Y., and Jaegermann W. (1994) Surface states on cubic d-band semiconductor pyrite (FeS2). *Surface Science* **314**(3), L931-L936.

Buker K., Alonso-Vante N., Scheer R., and Tributsch H. (1994) Influence of electrochemical activationand surface orientation on the photoresponse of single crystalline pyrite/electrolyte and pyrite/metal junctions. *Berichte Der Bunsen-Gesellschaft-Physical Chemistry Chemical Physics* **98**(5), 674-682.

Buker K., Alonso-Vante N., and Tributsch H. (1996) Photoelectrochemical investigations of complex formation phenomena on oriented n-pyrite (FeS_2) crystal surfaces. *Berichte der Bunsengesellschaft für Physikalische Chemie* **100**(11), 1808-1813.

Chandler R. N. and Bene R. W. (1973) EPR study of the solid solutions $Ni_xFe_{1-x}S_2$, $Co_xFe_{1-x}S_2$, and $Co_xNi_yFe_{1-x-y}S_2$. *Physical Review B.* **8**(11), 4979-4988.

Craig J. R., Vokes F. M., and Solberg T. N. (1998) Pyrite: physical and chemical textures. *Mineralium Deposita* **34**, 82-101.

Creager S. E. and Wooster T. T. (1998) A new way of using AC Voltammetry to study redox kinetics in electroactive monolayers. *Analytical Chemistry* **70**(20), 4257-4263.

Crundwell F. K. (1988) The influence of the electronic structure of solids on the anodic dissolution and leaching of semiconducting sulfide minerals. *Hydrometallurgy* **21**, 155-190.

Ennaoui A., Fiechter S., Jaegermann W., and Tributsch H. (1986) Photoelectrochemistry of highly quantum efficient single-crystalline n-FeS2 (pyrite). *Journal of the Electrochemical Society: Electrochemical Science and Technology* **133**(January No 1), 97-106.

Eyert V., Hock K. H., Fiechter S., and Tributsch H. (1998) Electronic structure of FeS_2: The crucial role of electron-lattice interaction. *Physical Review B.* **57**(11), 6350-6359.

Fan F. R. and Bard A. J. (1991) Scanning Tunneling Microscopy and Tunneling Spectroscopy of N-Type Iron Pyrite (N-Fes2) Single-Crystals. *Journal of Physical Chemistry* **95**(5), 1969-1976.

Fleischer M. (1955) Minor elements in some sulfide minerals. *Economic Geology* **50**, 970-1024.

Fox R. W. (1830) On the electromagnetic properties of metalliferous veins in the mines of Cornwall. *Philosophical Transactions* **pt. 2**, 399.

Gerischer H. (1961) Uber den ablauf von redoxreaktionen an metallen und halbleitern. *Zeitschrift fur Physikalische Chemie Neue Folge* **27**, 48-79.

Holmes P. R. and Crundwell F. K. (2000) The kinetics of the oxidation of pyrite by ferric ions and dissolved oxygen: an electrochemical study. *Geochimica et Cosmochimica Acta* **64**(2), 263-274.

Hung A., Muscat J., Yarovsky I., and Russo S. P. (2002a) Density-functional theory studies of pyrite FeS2 (111) and (210) surfaces. *Surface Science* **520**(1-2), 111-119.

Hung A., Muscat J., Yarovsky I., and Russo S. P. (2002b) Density-functional theory studies of pyrite FeS2(100) and (110) surfaces. *Surface Science* **513**(3), 511-524.

Jaegermann W. and Tributsch H. (1983) Photoelectrochemical reactions of FeS_2 pyrite with H_2O and reducing agents. *Journal of Applied Electrochemistry* **13**, 743-750.

Lehner S. W., Savage K. S., and Ayers J. C. (2006) Vapor growth and characterization of pyrite (FeS2) doped with Co, Ni, and As: Variations in semiconducting properties. *Journal of Crystal Growth* **286**(2), 306-317.

Li E. K., Johnson K. H., Eastman D. E., and Freeouf J. L. (1974) Localized and bandlike valence-electron states in FeS_2 and NiS_2. *Physical Review Letters* **32**(9), 470-472.

Moller P. and Kersten G. (1994) Electrochemical accumulation of visible gold on pyrite and arsenopyrite surfaces. *Mineralium Deposita* **29**, 404-413.

Morrison S. R. (1980) *Electrochemistry at semiconductor and oxidized metal electrodes*. Plenum

Press.

Nesbitt H. W., Bancroft G. M., Pratt A. R., and Scaini M. J. (1998) Sulfur and iron surface states on fractured pyrite surfaces. *American Mineralogist* **83**(9-10), 1067-1076.

Palache C., Berman H., and Frondel C. (1944) *The System of Mineralogy of James Dwight Dana and Edward Salisbury Dana Yale University 1837-1892*. John Wiley and Sons, INC.

Reedy B. J., Beattie J. K., and Lowson R. T. (1991) A vibrational spectroscopic ^{18}O tracer study of pyrite oxidation. *Geochimica et Cosmochimica Acta* **55**(6), 1609-1614.

Rimstidt J. D. and Vaughan D. J. (2003) Pyrite oxidation: a state-of-the-art assessment of the reaction mechanism. *Geochimica et Cosmochimica Acta* **67**(5), 873-880.

Rosso K. M. and Becker U. (2003) Proximity effects on semiconducting mineral surfaces II: : Distance dependence of indirect interactions. *Geochimica et Cosmochimica Acta* **67**(5), 941-953.

Rosso K. M., Becker U., and Hochella J., Michael F. (1999) The interaction of pyrite {100} surfaces with O_2 and H_2O: Fundamental oxidation mechanism. *American Mineralogist* **84**, 1549-1561.

Sato M. (1960) Oxidation of sulfide ore bodies, II. Oxidation mechanisms of sulfide minerals at 25^0 C. *Economic Geology* **55**, 1202-1231.

Schaufu[ss] A. G., Nesbitt H. W., Kartio I., Laajalehto K., Bancroft G. M., and Szargan R. (1998) Reactivity of surface chemical states on fractured pyrite. *Surface Science* **411**(3), 321-328.

Schoonen M. A. A., Elsetinow A. R., Borda M. J., and Strongin D. R. (2000) Effect of temperature and illumination on pyrite oxidation between pH 2 and 6. *Geochemical Transactions* **1**(4), 23-33.

Seeliger W., Troughton G. L., Alonso-Vante N., and Tributsch H. (1995) Evidence for site specific interaction of redox species at the FeS_2/electrolyte interface. *Journal of the Electrochemical Society* **142**(9), L166-L167.

Skey W. (1871) On the electromotive power of metallic sulfides. *New Zealand Inst. Trans. and Proc.* **3**, 2332-236.

Smith D. E. (1966) AC polarography and related techniques:Theory and practice. In *Electroanalytical Chemistry A Series of Advances*, Vol. 1 (ed. A. J. Bard), pp. 1-148. Marcel Dekker.

Springer G. (1970) Observations on the electrochemical reactivity of semiconducting minerals. *Transactions. Mineral processing & extractive metallurgy, Section C,* **79**, 11-14.

Sveshnikov G. B. and Dobychin S. L. (1956) Electrochemical solution of sulfides and dispersion aureoles of heavy metals. *Geochemistry* **4**, 413-419.

Tomm Y., Schieck R., Ellmer K., and Fiechter S. (1995) Growth mechanism and electronic properties of doped pyrite (FeS_2) crystals. *Journal of Crystal Growth* **146**(1-4), 271-276.

Wei D. and Osseo-Asare. (1996) Semiconductor electrochemistry of particulate pyrite: Dissloution via hole and electron pathways. *Journal of the Electrochemical Society: Electrochemical Science and Technology* **143**(10), 3192-3198.

Wei D. and OsseoAsare K. (1997) Semiconductor electrochemistry of particulate pyrite; mechanisms and products of dissolution. *Journal of the Electrochemical Society: Electrochemical Science and Technology* **144**(2), 546-553.

Williamson M. A. and Rimstidt J. D. (1994) The kinetics and electrochemical rate-determining step of aqueous pyrite oxidation. *Geochimica et Cosmochimica Acta* **58**(24), 5443-5454.

Wilson S. A., Ridley W. I., and Koenig A. E. (2002) Development of sulfide calibration standards for laser ablation inductively-coupled plasma mass spectrometry technique. *Journal of Analytical Atomic Spectrometry* **17**, 406-409.

Zhao G. L., Callaway J., and Hayashibara M. (1993) Electronic structures of iron and cobalt pyrites. *Physical Review B.* **48**(21), 15781-15786.

CHAPTER III

THE EFFECT OF AS, CO, AND NI IMPURITIES ON PYRITE OXIDATION KINETICS: BATCH AND FLOW-THROUGH REACTOR EXPERIMENTS WITH SYNTHETIC PYRITE

Abstract

Pyrite samples synthesized with As, Co, or Ni impurities and without added impurities were oxidized in batch and mixed flow-through reactors in the presence of 1 mM ferric iron, at pH 2. Six samples from each dopant population were used to provide a statistically robust comparison; two natural samples from Leadville, CO (major impurities Pb, As, Bi, Ag, Zn) and Elba, Italy (Co, As) were also included. In each experiment, three reaction progress variables were monitored: ferric iron, ferrous iron, and sulfate. The pyrite samples with impurities have average oxidation rates that are faster than the undoped samples, with As- and Co-doped pyrite having the highest rates. As, Co and Ni were released to solution in accordance with their concentrations in the solid samples. As concentrations in the batch reactor experiments tended to remain constant, in contrast to Co and Ni, which increased over time. Initial rates, calculated from the batch reactor experiments, were faster than the steady-state rates calculated from the mixed flow-through reactor experiments. Apparent rates calculated using sulfate were faster than apparent rates calculated using ferric and ferrous iron, reflecting oxidation of ferrous iron in solution by dissolved oxygen. The results imply that impurities in pyrite do contribute to its reactivity, in agreement with studies using electrochemical methods. Oxidation rate differences among pyrite samples with different impurities are probably too small to warrant explicit consideration in environmental modeling applications, but are important to understanding pyrite oxidation mechanisms and semiconducting properties.

Introduction

Pyrite oxidation has been studied for many decades because pyrite is a major source of acid rock drainage associated with coal, base metal, precious metal and gold mining operations. It is often a gangue mineral in metal ores, and a nuisance mineral in coal recovery and processing. Pyrite has also been studied by materials scientists as a photo-active material and for application in battery design. The focus of pyrite research, built upon fundamental studies of phase relations and behavioral properties, has been in four principle areas. (1) There are studies that emphasize the thermodynamics and oxidation behavior of pyrite to further understanding of froth flotation and other processes used in the recovery of metal sulfides (Chernyshova, 2003; Hicyilmaz et al., 2004; Reich and Becker, 2006; Tao et al., 2003; Wang, 1996); (2) There are studies of pyrite oxidation, with the aim to improve understanding and predictions of acid mine drainage generation (Brown and Jurinak, 1989; Kolker and Huggins, 2007; McKibben and Barnes, 1986; Moses et al., 1987; Singer and Stumm, 1970; Wiersma and Rimstidt, 1984; Williamson and Rimstidt, 1994); (3) There are studies that focus on pyrite's potential for solar energy conversion and use in electrochemical storage devices, on the basis of its semiconducting properties and photo potential (Abrams and Wilcoxon, 2005; Chongyang et al., 1988; Ennaoui et al., 1992; Gao et al., 2006; Wan et al., 2004; Wan et al., 2003; Wan et al., 2005); and (4) there is a body of literature on the possible role of pyrite as a substrate for the autocatalytic chain reactions that led to the spontaneous emergence of primitive organic molecules and life (Blochl et al., 1992; Huber and Wachtershauser, 1998; Tributsch et al., 2003; Wachtershauser, 1988, 1990, 1993, 1997)

Pyrite is known to contain a variety of trace metals and metalloids as impurities such as Ag, As, Au, Bi, Cd, Co, Cu, Hg, Mo, Ni, Pb, Pd, Ru, Sb, Se, Sn, Te, and Zn (Abraitis et al., 2004). A number of studies have shown that certain impurities, substituting for iron or sulfur in the pyrite crystal structure, affect the semiconducting properties of the crystal (Bither et al., 1968; Chandler and Bene, 1973; Eyert et al., 1998; Lehner et al., 2006; Li et al., 1974; Zhao et al., 1993). Arsenic, cobalt, and nickel are usually present in some combination in pyrite

(Shuey, 1975) in concentrations up to several weight percent. Arsenian pyrite has been reported to contain up to 10 weight percent As (Abraitis et al., 2004; Fleischer, 1955; Palache et al., 1944). Yet for decades, studies aimed at measuring reaction rates and understanding reaction mechanisms have not taken the impurity content of pyrite into account. This study is a complement to earlier work using the electrochemical techniques of cyclic and AC voltammetry that showed that pyrite with single impurities of As, Co, and Ni is more reactive than pyrite with little or no impurity content (Lehner et al., 2007). The work presented here uses batch and flow-through reactor experiments to statistically compare populations of synthetic pyrite either doped with As, Co, or Ni, or not doped. Two natural pyrite samples (from Leadville, CO and Elba, Italy) were also included in the experiments.

Postulated mechanisms of pyrite oxidation

One thread of ongoing queries regarding abiotic mechanism(s) of pyrite oxidation is about conditions under which the principal oxidant is dissolved oxygen or ferric iron, commonly expressed by the following reactions, respectively:

$$FeS_2 + 7/2O_2 + H_2O = Fe^{2+} + 2SO_4^{2-} + 2H^+ \quad (1)$$

$$FeS_2 + 14Fe^{3+} + 8H_2O = 15Fe^{2+} + 2SO_4^{2-} + 16H^+ \quad (2)$$

The simplified prevailing view is that under acidic conditions, ferric iron is the predominant oxidant, and the role of dissolved oxygen increases with increasing pH (Moses and Herman, 1991; Moses et al., 1987; Nicholson et al., 1988). For example, Evangelou and Zhang (1995) conclude from their comprehensive review of acid mine drainage that pyrite oxidation initially proceeds by Reaction 1 (O_2 oxidant), with subsequent oxidation and hydrolysis of the ferrous iron product releasing acid into the environment. When the pH drops below 3.5, Reaction 2 (ferric iron oxidant) becomes dominant. Rate laws for each of these oxidants under various solution conditions have been postulated, mostly on the basis of batch reactor experiments (Brown and Jurinak, 1989; Holmes and Crundwell, 2000; McKibben and Barnes, 1986; Moses and Herman, 1991; Moses et al., 1987; Nicholson et al., 1988; Wiersma and Rimstidt,

1984; Williamson and Rimstidt, 1994).

Surface spectroscopic studies have characterized surface sulfur species and oxidation products, as well as electronic surface states, relating them both to chemical species and to the band theory energy structure of bulk pyrite (Bronold et al., 1994; Doyle et al., 2004; Eggleston et al., 1996; Fan and Bard, 1991; Kendelewicz et al., 2004; Leiro et al., 2003; Mattila et al., 2004; Mattila et al., 2003; Nesbitt et al., 2004; Nesbitt et al., 2000; Nesbitt et al., 2003; Rosso et al., 2000; Schaufu[ss] et al., 1998; Uhlig et al., 2001). The work that they have done describes a molecular scale environment where the discontinuation of the pyrite crystal lattice introduces reactive surface sulfur and iron states. When S-S and Fe-S bonds are broken a suite of surface configurations emerge. There are three S surface states corresponding to S^{2-} surface states with bulk coordination, S^{2-} surface states of the first disulfide layer and S^{2-} surface states resulting from broken S-S bonds (Schaufu[ss] et al., 1998). There are also three Fe surface states: Fe^{2+} residing at bulk sites, Fe^{2+} residing on surfaces edges and corners, and Fe^{3+} surface states resulting from the reduction of S^{-} at broken S-S bonds (Nesbitt et al., 2000).

Finally, isotopic studies using labeled O_2 have been used to investigate the source of oxygen in sulfate and other sulfoxy groups that are oxidation products of pyrite. A dissolved oxygen source suggests that DO directly oxidizes the sulfur atoms in the disulfide group, whereas a water source suggests that ferric iron is the oxidant, in which case dissolved oxygen may participate in the reaction process as an oxidant to ferrous iron. Reedy et al (1991), Usher et al., (2004), and earlier studies cited by Moses et al., 1987 (Bailey and Peters, 1976; Taylor et al., 1984) all concur that most, if not all, of the oxygen in the sulfate is sourced from water, in agreement with the second scenario. Moreover, Usher et al., (2004) also found that dissolved O_2 is the source for oxygen in iron oxyhydroxides produced during oxidation. Thus the prevailing evidence is for ferric iron as the direct oxidant, with a supporting role by dissolved oxygen at higher pH. The rate-determining step was early postulated to be the oxidation of ferrous iron by dissolved oxygen (Singer and Stumm, 1970),

What is/are the molecular-scale electron transfer pathway(s) at the pyrite surface? The

view emerging from the last fifty years of pyrite oxidation studies is that there probably are multiple pathways for the charge transfer associated with pyrite oxidation to occur (Druschel and Borda, 2006). For example, Rimstidt and Vaughn (2003) concluded from their literature survey that pyrite oxidation is an electrochemical process that can be described by separate cathodic and anodic reactions, in agreement with Holmes and Crundwell (2000). These reactions may occur on physically separated surface sites, as suggested by Becker et al., (2001) and Rosso and Becker (2003). The cathodic site supports the rate-determining step where an electron is transferred from a lattice cation (assumed to be ferrous iron) to an oxidant, most commonly ferric iron or dissolved oxygen. This electron is replaced by one from the anodic sulfur site, and the positive charge resulting from delivery of electrons to the cathodic site attracts water molecules. The oxygen in the water bonds with the surface sulfur and subsequently a proton is released into the solution. As this process is repeated, the terminal S atom is progressively oxidized and more protons are released into solution. Eventually, the sulf-oxy surface complex becomes unstable and is released into solution, usually in the form of sulfate but at higher pH perhaps in the form of thiosulfate.

Others have previously suggested the progressive complexation of surface sulfur by water to form the sulf-oxy species, postulating various electron transfer mechanisms. Luther (1987) used molecular orbital theory, hypothesizing the formation of a "persulfido" bridge, where ferric iron attaches to the S_2^{2-} site on the pyrite surface via an inner sphere process. Single electron transfer steps occur between π^* S orbitals in the pyrite to lower energy π orbitals in the ferric iron via this bridge. The reaction proceeds by producing sulfoxy intermediates which are oxidized by reaction with ferric ion to ultimately form sulfate. Moses and Herman (1991) proposed a mechanism whereby aqueous ferrous iron is adsorbed onto the pyrite surface preferentially over ferric iron. This adsorbed ferrous iron is oxidized by dissolved oxygen. The resulting adsorbed ferric iron oxidizes the sulfur in pyrite, and is then cycled between valence states until a stable sulf-oxy species dissociates from the surface. Brown and Jurinak (1989) hypothesize an inner-sphere electron transfer via the disulfide surface site, promoted by a hydroxyl bridging

ligand.

Another pathway, where holes generated from light exposure or defects from impurities result in the nucleophilic attack of water and eventual breaking of bonds, was proposed by Mishra and Osseo-Asare (1992) and further investigated by Wei and Osseo-Asare (1996; 1997). It was supported by the results of Lehner et al. (2007), whose electrochemical investigation suggested that arsenian pyrite, perhaps due to its p-type conductivity (i.e., holes for majority charge carriers), oxidizes faster than pyrite with no impurities or pyrite with Co or Ni.

Pyrite oxidation rate dependencies

Oxidation rate laws reflecting dependencies on various parameters are usually based on results obtained using either iron (ferric or ferrous) or sulfur (total sulfur or sulfate) as a reaction progress variable. For example, Weirsma and Rimstidt (1984) measured rates of reaction of pyrite and marcasite at pH 2 using ferric iron as both the oxidant and the reaction progress variable. They found the reaction to conform to a rate law: $-\frac{dm_{Fe^{3+}}}{dt} = k\left(\frac{A}{M}\right)m_{Fe^{3+}}$,

where $m_{Fe^{3+}}$ is the molal concentration of ferric iron, k is the rate constant, A is the surface area of the pyrite and M is the mass of the solution. McKibben and Barnes (1986) derived rate laws in dilute acidic chloride solutions for the reaction of pyrite with ferric ion $\left(R_{Fe^{3+}} = -10^{-9.74} M_{Fe^{3+}}^{0.5} M_{H^+}^{-0.5}\right)$, dissolved oxygen $\left(R_{O_2} = -10^{-6.77} M_{O_2}^{0.5}\right)$, and hydrogen peroxide $\left(R_{H_2O_2} = -10^{-1.43} M_{H_2O_2}\right)$.

Moses et al., (1987) explored pyrite reaction rates in solutions from pH 2 to 9 containing both dissolved oxygen and ferric iron. Using total sulfur and sulfate as reaction progress variables, they determined that the rate of oxidation was more dependent on the ferric iron concentration than on the presence of dissolved oxygen. At higher pH the role of oxygen became more important as an oxidant for ferrous iron, thereby providing a supply of ferric iron for the pyrite oxidation. Brown and Jurinak also (1989) found that ferric iron is the rate-controlling oxidant even at high pH by observing the effect of DTPA on the reaction. Furthermore they report that the presence of Cl^- and SO_4^{2-} slow the rate of pyrite reaction and

speculate that this is due to the complexing of ferric ion. In contrast, Nicholson et al. (1988) dismiss the role of ferric iron in carbonate-buffered solutions in the pH range 6.7 to 8.5. They found a non-linear relation with the oxygen concentration, being limited by the adsorption of O_2 and decomposition of oxidation products on the surface. Williamson and Rimstidt (1994) compiled rate data from the literature and produced rate laws for the oxidation of pyrite by dissolved oxygen, and by ferric iron in the presence and absence of dissolved oxygen. Their rate law for reaction with ferric iron in the presence of dissolved oxygen is:

$$R = 10^{-6.07} \frac{m_{Fe^{3+}}^{0.93}}{m_{Fe2+}^{0.40}} \qquad (3)$$

where R represents the destruction of pyrite in mol m^{-2} s^{-1}. They considered the fractional orders of reaction to indicate an electrochemical oxidation mechanism involving non-site-specific anodic and cathodic reactions. Holmes and Crundwell (2000) used electrochemical techniques to derive a generalized rate law and their results support this hypothesis.

In addition to addressing the roles of ferric iron and dissolved oxygen, oxidation rate studies performed with wet chemical methods have been used to investigate rate dependencies on temperature (Nicholson et al., 1988), surface area, and time. Weirsma and Rimstidt's (1984) law implies that the rate of reaction is directly proportional to the pyrite surface area. Likewise, Nicholson et al. (1988) found a linear dependence of oxidation rate on the surface area in studies at near-neutral pH in carbonate-buffered solutions. However, McKibben and Barnes (1986) report that reactive surface area is less than total surface area and question the assumption of a first order dependence of oxidation rates on surface area.

Brown and Jurinak (1989) studied pyrite oxidation in acid and alkaline solutions for up to 3 weeks and found the rate to be independent of time. However, Nicholson et al. (1990) ran oxidation experiments in carbonate buffered solutions for 10,000 hours and report the rate decreasing with time. On the basis of surface analysis by XPS that revealed a ferric oxide coating on the pyrite samples, they speculated that pyrite oxidation at near-neutral pH can be modeled by a "shrinking-core" concept whereby the grains become coated with ferric hydrox-

ide, limiting the transport of H^+ ions and the reactivity of the pyrite surface. Williamson and Rimstidt (1994) performed experiments where a single pyrite sample, repeatedly reacted under identical solution conditions, showed the rate of oxidation slowing.

Only a few studies have considered pyrite composition explicitly as an influence on oxidation rates. Weirsma and Rimstidt (1984) compared oxidation rates of early diagenetic pyrite formed at low temperature to those of high-temperature hydrothermal pyrite. They report higher rate constants for oxidation of the pyrite formed at higher temperatures but concluded that, geologically, the rate differences were insignificant. Nicholson et al. (1988) studied five different types of pyrite and found the same rate of oxidation within 25%. They provide some trace element concentrations, though they were unable to determine if the trace elements were in the pyrite or secondary phases; arsenic was not reported. Manaka (2007) focused on the effect of impurities on oxidation rates of five pyrites from different locations using dissolved oxygen as a reaction progress variable, at pH 4. Impurities distributed in secondary sulfide phases were treated analytically in the same way as those in solid solution. Manaka reports that the oxidation rate was positively correlated with impurity concentrations.

To date there hasn't been a study using wet chemical methods aimed at determining the effect of individual common impurities, substituting for iron and sulfur in the pyrite lattice, on the rate of pyrite oxidation. In the study described here, temperature was held constant. Representative sub-samples of material from each dopant type were analyzed repeatedly for surface area and the different types were determined to be statistically the same.

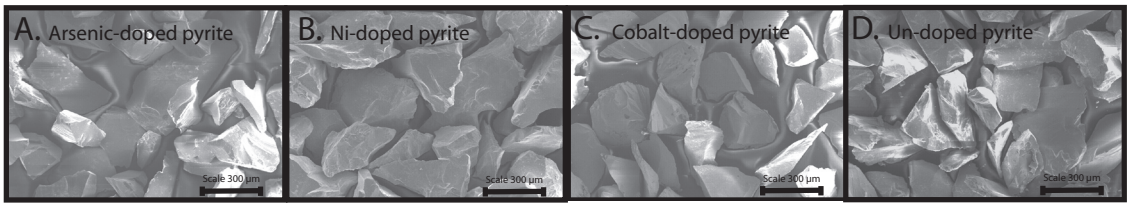

Figure 1. SEM secondary electron images showing the samples of synthetic pyrite from each doped population that were used for surface area measurements.

Experimental procedures using batch and flow-through reactors were also consistent for all of the samples. Hence, the rates reported below reflect differences in pyrite composition, tracked with three reaction progress variables: ferric iron, ferrous iron, and sulfate.

Methods

Samples

The pyrite used in this study was synthesized in our laboratory with chemical vapor transport (CVT) in sealed evacuated quartz tubes that were placed in a temperature gradient of ~700 to 550 °C over 16 cm, with $FeBr_3$ as a transport agent (Lehner et al., 2006). The synthesized pyrite was doped with either As, Co, Ni or nothing at all and exhibited a range of electrical properties. Pyrite from the Black Cloud Mine (Leadville, CO) found to contain primarily As, Pb, Bi, and Ag impurities was also studied, along with one sample from Elba (Italy) found to contain a heterogeneously distributed combination of As, Co and Ni (Savage et al., in review). The experiments were conducted for six different samples of each kind of synthetic material: Undoped, Co-doped, Ni-doped and As-doped as well as for one natural sample from Leadville, CO and one natural sample from Elba, Italy.

Synthetic crystals were first cleaned with acetone followed by 5M HCl and then DI water. Residues from the synthesis process were removed by soaking in ethylenediamine until visual inspection under a light microscope revealed clean surfaces. Then the crystals were ground with a mortar and pestle and sieved to a size fraction of 150 to 250 ≤m. The sieved material was subjected to the following cleaning procedure: Soak in 1M HCl for 30 minutes, rinse three times with DI water, submerge sample in organic solvent (acetone, ethanol or methanol), swirl or agitate/stir and decant cloudy liquid – repeat until liquid remains clear; soak in 0.5M $HNO_{3,}$ rinse 3 times in DI water, rinse once again with solvent, dry at 40 degrees C in glove box with 98.5 % N_2 atmosphere.

The sieved and cleaned pyrite (see Figure 1) was sealed between two circular pieces of 150 μm plastic mesh with silicone aquarium sealant. The sealed pyrite bags and sieved pyrite

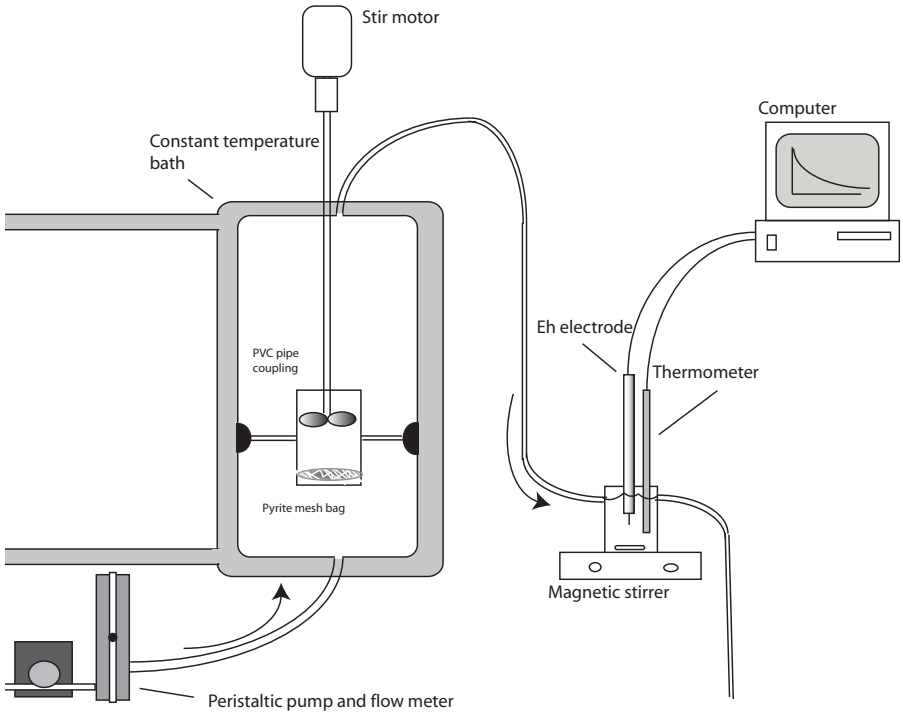

Figure 2. Schematic showing mixed flow reactor setup.

were stored in a glove box under a predominantly nitrogen atmosphere. The sieved material < 150 μm was analyzed by ALS Chemex Laboratories for trace element concentration using ICP-AES following digestion in aqua-regia.

Reactor set-up

The oxidation experiments were carried out in a 0.01M NaCl solution of deionized water equilibrated with atmospheric oxygen and carbon dioxide and acidified with HCl to pH 2, to which 1mM ferric iron was added as $FeCl_3$, resulting in a solution with an ionic strength of 0.026. The procedure was to run the mixed flow experiment to steady state and then immediately run the batch reactor experiment with the same pyrite sample. The flow-through reactor capacity was ~ 950 mL (see Figure 2). Run fluid was pumped through a flow meter into the bottom of the reactor at a rate of 4.71 mL min^{-1} with a standard deviation of 0.12 mL min^{-1} with a peristaltic pump. The fluid exited at the top and flowed to a 50 mL beaker containing

a magnetic stir bar where the temperature and Eh were monitored. The pyrite mesh bags were mounted in a 2 inch PVC pipe coupling suspended in the center of the reactor with aquarium suction cups. An overhead stirring motor with a glass stir rod to which a Teflon propeller blade was attached forced the solution through the PVC pipe and the pyrite mesh bag (see Figure 2). The run solution for the mixed flow experiments was measured for pH, ionic conductivity, dissolved oxygen with HACH DR2400 spectrophotometer (Hach method 8166, program 455) and for ferrous iron using a 1, 10 phenanthroline method (Hach method 8146, program 255), and total iron (Hach method 8008, program 265). Dye tests showed a well mixed solution in the main body of the reactor.

Each batch reaction experiment was conducted using 650 mL of the same batch of initial run solution that had been used for the corresponding mixed flow experiment. The pyrite bag was suspended in the bottom of the reactor by the same method described above. An overhead stir motor was employed as above. Eight 10 mL aliquots were withdrawn from the initial volume of the batch reactor at 5, 10, 15, 20, 30, 40, 50, and 65 minutes, after which the experiment was terminated. The temperature, Eh and pH were monitored. The 10 mL aliquots were divided as follows: 5 mL was used for HACH DR2400 spectrophotometer measurements of ferrous iron, 1 mL was used for spectrophotometer measurements of total iron, 1 mL was used for ICPMS trace element analysis, and 3 mL were used for sulfate analysis with ion chromatography. The solution emf was measured electronically with a either a platinum or gold redox electrode and recorded (see ferric iron RPV, below).

BET and particle size analysis

Samples weighing 4 grams of each doped type of ground and cleaned synthetic pyrite were analyzed for surface area using a 7 point BET method. Each sample was analyzed either six or seven times. The resulting populations were statistically analyzed to determine the standard deviation, median and mean of the results. The populations were tested using ANOVA to determine if differences in the means were statistically significant. The mean value of the all the BET measurements was used to calculate the reaction rates. The samples were also analyzed

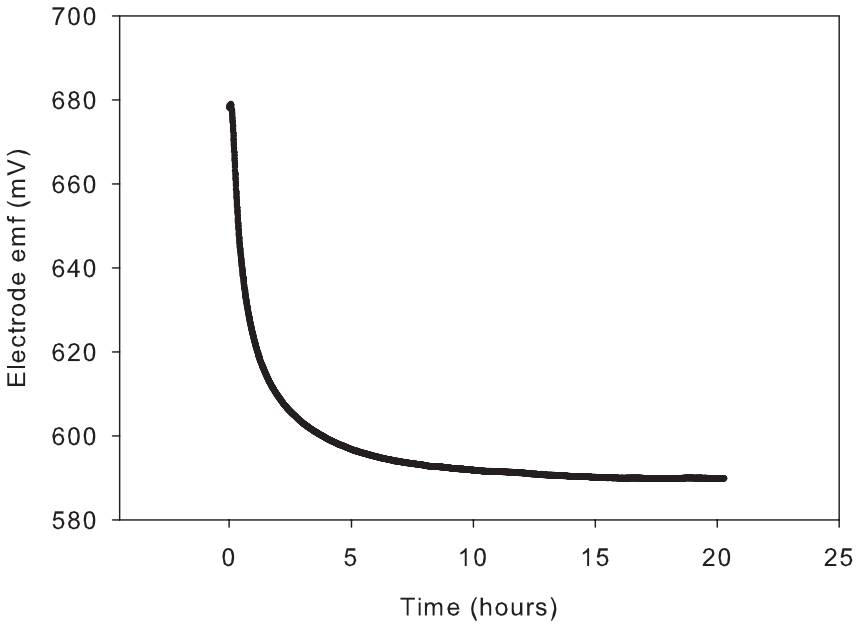

Figure 3. Example illustrating achievement of steady state conditions according to emf readings of effluent solution during the course of a typical mixed-flow reactor experiment.

with a Malvern Hydro 2000 MU (A) general purpose particle size analyzer.

Reaction progress variables (RPVs)

The rates of reaction were calculated with three reaction progress variables: Free ferric iron concentration, total ferrous iron concentration and sulfate concentration.

The free ferric iron concentration was calculated from the emf measured using either a gold (Radiometer M241AU2-8) or platinum (Radiometer MC3501Pt) Ag/AgCl redox electrode and a Radiometer 856 Titramaster titration workstation. The electrodes were calibrated using a standard Zobels solution and by the method of Nordstrom (1977). The potential of the redox electrode vs the Standard Hydrogen Electrode was added to the measured emf value to obtain the Eh at measured value. The values were recorded every 8 seconds for the mixed flow experiments (Figure 3) and every 2 seconds for the batch reactor experiments. The free ferric iron concentration was calculated using the Nernst Equation and a reaction path model created using Phreeqc (Parkhurst and Appelo, 1999) that simulated the reaction of a small amount of pyrite with the run solution in 500 time steps (Appendix I). This way a value for molal concen-

tration of ferric iron could be assessed for any Eh value. This method was employed to determine the uncomplexed ferric iron concentration of the initial run solution as well.

The ferrous iron concentrations of the steady state mixed flow-through reactor effluent and the aliquots withdrawn from the batch reactor experiments were measured by the same method as the run solution; 5 mL aliquots were diluted 5 times to be within the method detection range of 0.02-3.00 mg/L. The sulfate concentration was measured with a Dionex ion chromatography set-up using an LC25 chromatographic oven with an ED50 electrochemical detector and a GP50 gradient pump. The analysis was calibrated using Dionex 7 ion standard #056933 diluted 5, 10, 50, and 100 times and checked against an SPEX 7 ion standard diluted 10 times. A de-ionized water blank and a sample of the Dionex 7 ion standard solution, diluted 10x, was run after every 11 samples.

Concentration of As, Co and Ni in sample and solution

The solid pyrite sample concentration of As, Co, and Ni as well as a suite of other trace elements was measured with ICP-AES by ALS Chemex Corporation using their MEICP-41 method. The error for this method is ±7%. The concentration of As, Co, and Ni in the end solution from the mixed-flow reactor experiments and in aliquots withdrawn from the batch reactor experiments was measured with inductively coupled plasma mass spectrometry (ICPMS) using a Perkin Elmer Elan DRC ICPMS with Ar plasma. For every 11-22 samples, a de-ionized water blank and a standard calibration solution with elemental concentrations of 50 µg/L was analyzed for quality control and error estimation. We also ran a run solution blank, i.e. a sample of run solution that hadn't been in contact with pyrite.

Rate calculations

Rates were calculated from the mixed flow-through (MF) reactor data by multiplying the difference between the initial and steady state fluid concentrations of the reaction progress variable (RPV) by the flow rate of the run solution (Rimstidt and Newcomb, 1993). The concentrations of each RPV were measured in both the influent and effluent solutions in the same

manner. The batch reactor rates were calculated according to the initial rate method (Rimstidt and Newcomb, 1993). The RPV concentrations from aliquots taken at 5, 10, 15, 20, 30, 40, 50, and 65 minutes were fit to a linear and a polynomial function, and the apparent rate was obtained by taking the derivatives with respect to time (Appendix I). All rates were normalized to a $1m^2$ surface area per kilogram of solution system using the mean BET surface area.

Data analysis

Experiments were performed on four populations (six samples each) of synthetic pyrite, plus two natural pyrite samples. The synthetic samples were undoped, Ni-doped, Co-doped and As-doped pyrite, and the natural samples were from Elba (Italy) and Leadville, CO. For each population there were three sets of rate data generated from three reaction progress variables: ferric iron, ferrous iron and sulfate. In order to compare the different populations, the set of rates obtained for the samples in each population was analyzed with the Shapiro-Wilk normality test. Those that failed were compared with non-parametric Wilcoxon signed rank test. The populations that were normally distributed were compared with ANOVA and the independent samples T-test.

Results

Overview

The rate data is given in Table 1 with the rates expressed in nmol of RPV m^{-2} s^{-1}. In general, the samples with impurities average somewhat faster oxidation rates than the undoped samples. This is in agreement with the results of the electrochemical study (Lehner et al., 2007). The rates calculated from the batch reactor experiments were faster than the rates calculated from the mixed flow-through reactor experiments. Differences were also observed in the rates calculated using different reaction progress variables. The mean of the ratio $\frac{rSO_4^{2-}}{rFe^{2+}}$, i.e. the rate of sulfate increase divided by the rate of ferrous iron increase, was 1.45 ± 0.53 for all 24 synthetic pyrite mixed flow reactor experiments. The mean of the ratio $\frac{rSO_4^{2-}}{-rFe^{3+}}$, i.e. the rate of sulfate increase divided by the rate of ferric iron decrease, was 1.93 ± 0.66. The mean of

Table 1. Calculated rates in nmol RPV $m^{-2}s^{-1}$ for mixed flow and batch experiments.

	Mixed flow reactor			Batch reactor		
RPV Sample	SO_4^{2-} (nmol $m^{-2}s^{-1}$)	Fe^{2+} (nmol $m^{-2}s^{-1}$)	Fe^{3+} (nmol $m^{-2}s^{-1}$)	SO_4^{2-} (nmol $m^{-2}s^{-1}$)	Fe^{2+} (nmol $m^{-2}s^{-1}$)	Fe^{3+} (nmol $m^{-2}s^{-1}$)
Un4	10	32	25	96	91	88
Un5	44	31	24	92	69	66
Un6	32	30	22	116	26	59
Un7	34	19	14	80	33	41
Un8	62	27	18	117	81	64
Un9	62	39	25	58	90	66
As3	26	19	14	77	69	19
As4	47	58	40	87	108	58
As5	39	46	34	108	68	46
As6	56	30	22	90	90	30
As7	68	47	36	105	88	47
As8	55	46	29	93	61	46
Co3	46	62	48	106	115	80
Co4	41	25	17	102	94	86
Co5	46	27	21	113	47	73
Co6	63	54	35	177	95	74
Co7	66	53	35	132	87	62
Co8	56	28	23	125	80	71
Ni3	36	28	20	136	83	28
Ni4	51	51	38	106	83	51
Ni5	59	53	39	93	76	53
Ni6	43	26	17	106	83	26
Ni7	47	27	19	107	91	27
Ni8	50	24	20	132	75	24
Elba	61	46	34	62	41	45
Leadville	69	49	37	100	85	74

$\frac{-rFe^{3+}}{rFe^{2+}}$ was 0.75 ± 0.06. These ratios were all normally distributed.

BET surface area and particle size distribution

All populations of surface area measurements were normally distributed. The overall mean was 0.0869 m^2g^{-1}. The 4g samples measured were a subset of the material used in the experiments. Though in these subsets there were slight differences among the populations, the analysis of variance indicated they weren't significant enough to extrapolate to the rest of the material. The ANOVA probability for accepting the null hypothesis (that the true means were the same) was 0.217; to reject the null hypothesis the probability would have to be 0.05 or less.

Table 2. Impurity concentrations in pyrite samples (parts per million)

Sample	As	Co	Ni	Cr	Cu	Pb	Sb	V	Ag	Bi	Mn	W	Zn
Un4	7	3	2	7	1	5	<2	2	<0.2	<2	<5	<10	<2
Un5	6	1	10	8	1	<2	<2	1	<0.2	2	<5	<10	<2
Un6	6	1	10	8	1	<2	<2	1	<0.2	2	<5	<10	<2
Un7	<2	1	3	5	1	4	<2	2	<0.2	<2	<5	<10	<2
Un8	<2	<1	4	10	1	2	<2	2	<0.2	2	<5	<10	<2
Un9	<2	<1	4	10	1	2	<2	2	<0.2	2	<5	<10	<2
Ni3	4	1	7090	14	1	<2	<2	1	<0.2	<2	<5	<10	<2
Ni4	3	2	>10000	11	1	<2	<2	1	0.3	2	<5	<10	<2
Ni5	3	2	>10000	11	1	<2	<2	1	0.3	2	<5	<10	<2
Ni6	14	2	>10000	12	<1	<2	<2	2	<0.2	<2	<5	<10	<2
Ni7	7	<1	5180	12	1	<2	<2	2	<0.2	2	<5	<10	<2
Ni8	6	63	5310	17	1	<2	<2	2	<0.2	2	<5	<10	<2
Co3	6	6415	34	26	1	<2	<2	1	0.3	<2	7	<10	<2
Co4	6	6415	34	26	1	<2	<2	1	0.3	<2	7	<10	<2
Co5	6	5750	19	10	1	<2	<2	1	<0.2	<2	<5	<10	<2
Co6	34	>10000	18	19	1	2	<2	2	<0.2	<2	<5	<10	<2
Co7	16	8430	20	27	1	<2	<2	2	<0.2	<2	<5	<10	<2
Co8	16	8430	20	27	1	<2	<2	2	<0.2	<2	<5	<10	<2
As3	472	8	9	3	1	2	<2	2	<0.2	2	<5	<10	<2
As4	1240	2	14	16	4	4	3	2	<0.2	2	<5	<10	<2
As5	1240	2	14	16	4	4	3	2	<0.2	2	<5	<10	<2
As6	8360	1	12	17	1	<2	22	2	<0.2	6	<5	<10	<2
As7	7730	20	17	13	2	<2	18	1	<0.2	5	<5	<10	<2
As8	7730	20	17	13	2	<2	18	1	<0.2	5	<5	<10	<2
Leadville	644	28	30	12	66	>10000	7	2	>100	879	12	30	246
Elba	429	535	71	<1	5	9	<2	1	0.3	5	34	<10	5

Nonetheless, this is a potential source of error in the rate calculation. The particle sizes in each subset were nearly identically distributed between ~ 98 and 590 μm.

Impurity concentration in solid pyrite

All the synthetic pyrite samples were shown to contain the impurities they were intended to have. Concentrations range from 472 to 8360 ppm (Table 2). The Leadville, CO sample had Pb concentration above the detection limits of the method (> 10,000ppm). It also contained As, Bi, Ag and Zn in significant concentration though inspection under visible light microscope, reflected light microscope, and SEM magnification reveals no inclusions or secondary phases. The Elba sample contained As, Co and Ni and a small amount of Mn (Table 2).

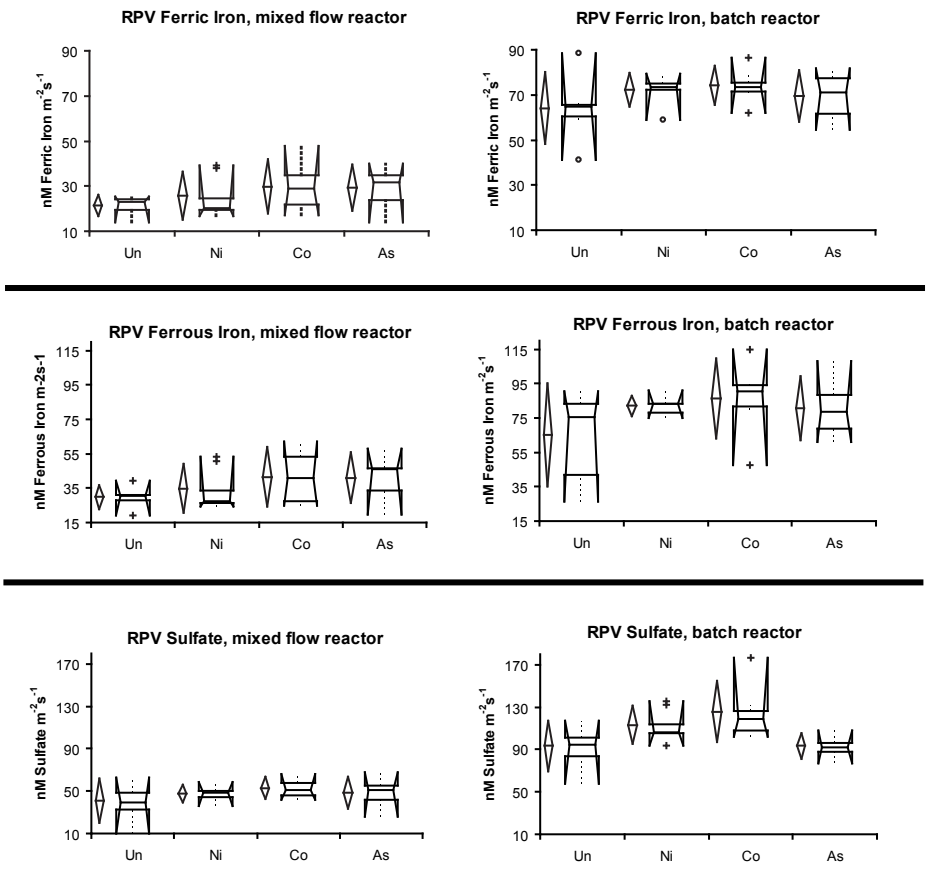

Figure 4. Results of statistical analyses of reaction rates for each population of synthetic pyrite samples, expressed in terms of three reaction progress variables: ferric iron reduction, production of ferrous iron, and production of sulfate. Rate distributions are shown for both mixed-flow experiments (left column) and batch reactor experiments (right column). The diamonds represent the 95% confidence interval for the mean from parametric analysis. The notched box and whisker plots represent Wilcoxon signed rank test. The notch is the 95% confidence interval for the median. The top and bottom of the box represents the inter-quartile range.

MF reactor rates with ferric and ferrous iron as reaction progress variables (RPV)

The pyrite oxidation rates calculated with ferric iron as RPV are shown in Figure 4. The 2 sample T-test showed that the oxidation rate for undoped pyrite was less than that for As-doped pyrite at the 95% confidence level and less than that for Co-doped pyrite at the 94% confidence level; the Ni-doped population failed the normality test and was not compared with this method. All the populations passed the F test for equal variance, enabling the use of the Wilcoxon signed rank test. The MF reactor results for the Wilcoxon signed rank test for all re-

action progress variables are given in Table 3. The rates obtained from the ferrous iron concentrations (measured by spectrophotometer) are very close to those calculated from the free ferric iron (from emf measurement). Again the Ni-doped population failed the normality test but all populations passed the F-test. The 2 sample T-test showed that the rate for undoped pyrite was less than that for As-doped pyrite at the 86% confidence level and less than that for Co-doped pyrite at the 90% confidence level.

For the mixed flow reactor, the emf measurement of the influent run solution and the spectrophotometer results always indicated a small amount of ferrous iron even though only ferric chloride was added at 1mM. The free ferric iron concentration of the run solution after considering the results of the speciation model was approximately 0.5mM.

Table 3. One-sided statistical probabilities that pairs of synthetic pyrite populations differ in oxidation rates, calculated from mixed flow reactor results

	Wilcoxon signed rank test probability						
RPV	Un<Ni	Un<Co	Un<As	Ni<Co	Co<As	Ni<As	As<Co
Fe^{3+}	0.72	0.78	0.92	0.66	0.50	0.78	0.42
Fe^{2+}	0.72	0.78	0.92	0.72	0.58	0.72	0.50
SO_4^{2-}	0.72	0.89	0.92	0.72	0.11	0.58	0.69

The values represent the confidence level of the hypothesis represented by the < symbol

MF reactor rates with sulfate as RPV

All populations passed both the normality test and the F-test for equal variance. The parametric comparisons using the T-test are given below along with the results from the Wilcoxon signed rank test. The trend is for doped populations to have faster rates than the undoped population (Figure 4) but it is not as pronounced with the parametric comparison as it is with the nonparametric analysis. The Wilcoxon comparison is given in Table 3.

Batch reactor rates

Each synthetic pyrite dopant group's population of oxidation rates determined from batch reaction experiments passed the normality test. The trend for the rates from the batch

Table 4. One-sided statistical probabilities that pairs of synthetic pyrite populations differ in oxidation rates, calculated from 2nd order polynomial fit of batch reactor results

	T Test probability					
RPV	Un<Ni	Un<Co	Un<As	Ni<Co	Ni<As	As<Co
Fe^{3+}	0.87	0.91	0.75	0.68	0.31	0.80
Fe^{2+}	0.91	0.82	0.86	0.67	0.44	0.68
SO_4^{2-}	0.89	0.95	0.51	0.81	0.02	0.99

The values represent the confidence level of the hypothesis represented by the < symbol

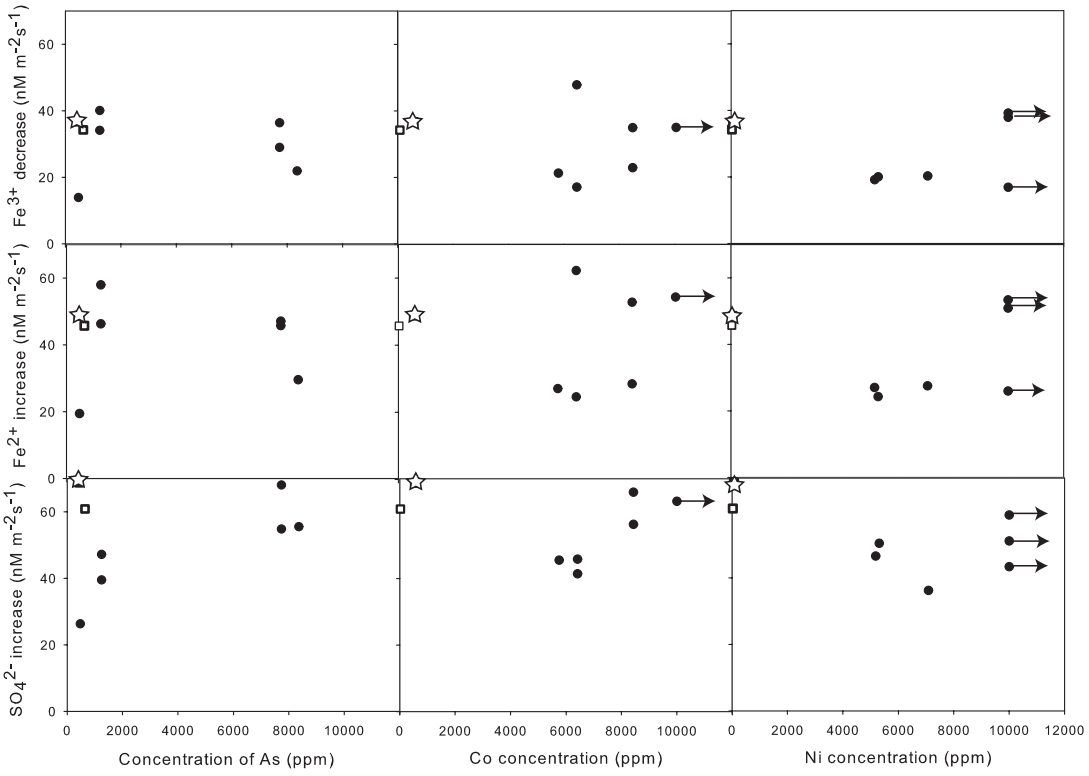

Figure 5. Reaction rates for each pyrite sample determined from mixed flow reactor experiments, plotted against the concentration of impurity elements in the solid. Results for each reaction progress variable are shown. Each point represents one experiment. Arrows indicate concentration is 10,000 ppm or greater. The star represents the Leadville natural sample and the open square represents the Elba sample.

reaction experiments was similar to that from the MF experiments though less pronounced (see Table 4). However, for sulfate as RPV the As-doped population was statistically the same as the undoped population (Figure 4). The populations of rates calculated from the linear fit of the first four data points at 5, 10, 15, and 20 minutes showed much less variability than the

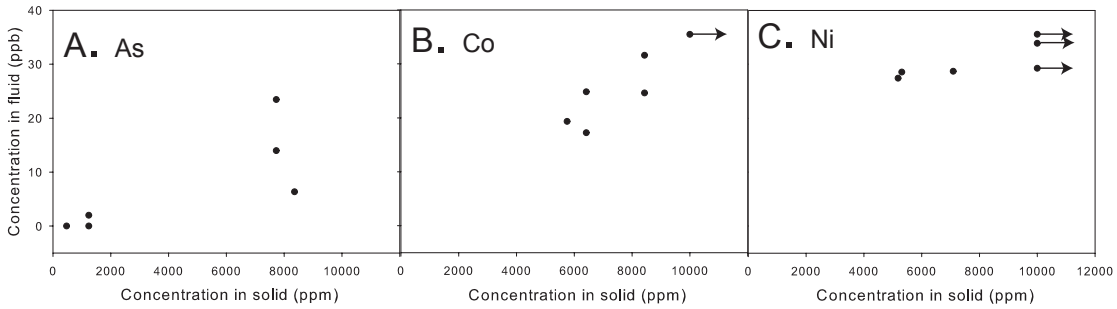

Figure 6. Solution concentrations of minor elements released from pyrite, after achievement of steady state in mixed flow reactor experiments, plotted against the concentration of impurity elements in the solid. Each point represents one experiment. Arrows indicate concentration is 10,000 ppm or greater.

rates calculated from the polynomial fit of the full 65 minute experiment. This is reflected in their respective ANOVA probabilities. The probability of the means being the same drops from 50% to ~40% and 30% for the linear-fit ferric and ferrous iron RPV data respectively, while the probability drops from 69% to 0.03% for the sulfate RPV data.

Reaction rates as a function of impurity concentration in pyrite

The impurity concentration in the pyrite is not controllable in the synthesis process and therefore the spread in concentrations is not ideal for defining a correlation between pyrite impurity concentration and oxidation rate. However, in mixed flow experiments, reaction rates calculated with sulfate as the RPV appear correlated with solid impurity concentration for As and Co with R^2 values of 0.71and 0.81 respectively (Figure 5). No correlation is observed between solid impurity concentration and reaction rates calculated from the batch reactor experiments. The two natural pyrite samples from Elba and Leadville plot near the top of the rate axis and near the bottom of the impurity concentration axis.

Trace element concentration in solution (ICPMS)

The concentrations of As, Co, and Ni in the solutions sampled at the end of the MF

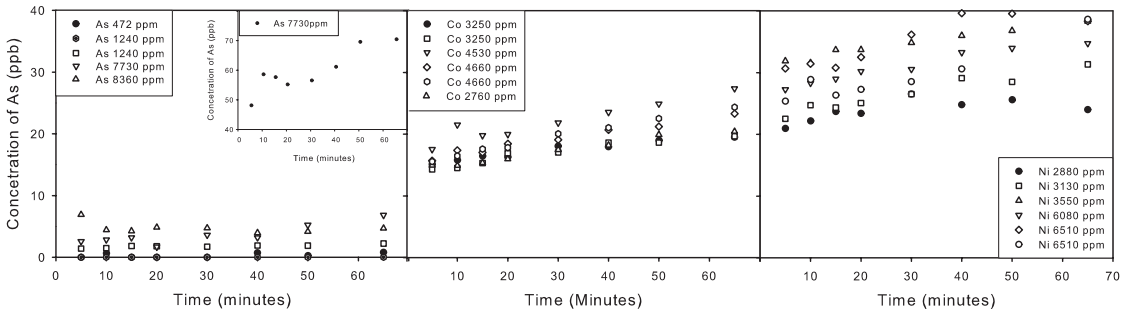

Figure 7. Solution concentrations of minor elements released from pyrite over the course of batch reactor experiments. Values in legends represent the concentration of the impurity element in the reacting pyrite sample.

reactor experiments are loosely correlated with their concentrations in the reacted material (Figure 6). The data from the batch reaction experiments clearly shows increasing Co and Ni concentrations as the reaction progresses (Figure 7). The trend is not seen for most As-doped samples except for one with anomalously high values, possibly due to incomplete cleaning whereby some secondary As-containing phase from the synthesis process (Lehner et al., 2006) was not completely removed (Figure 7A). The Leadville sample contributed significant

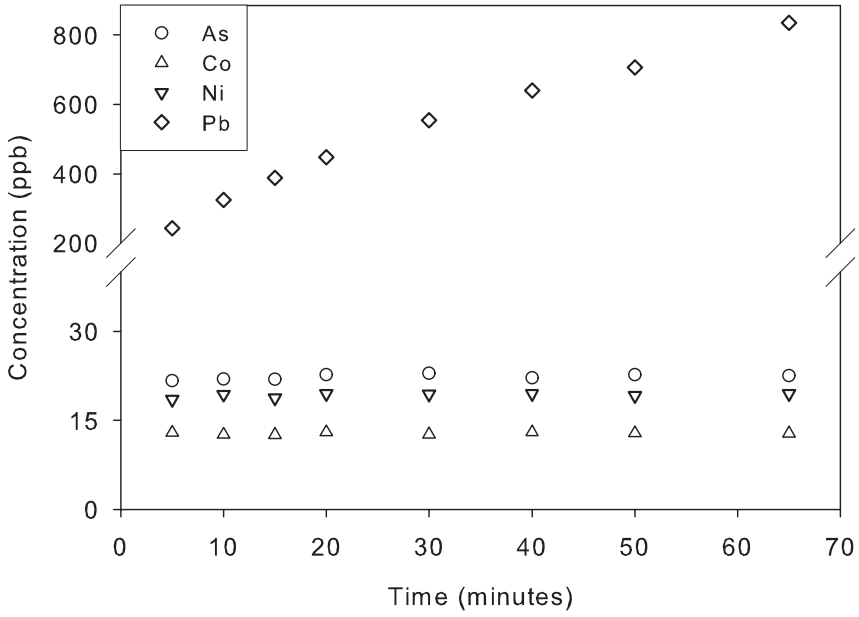

Figure 8. Solution concentrations of minor elements released from the Leadville, CO pyrite sample over the course of a batch reactor experiment.

Pb to the solution as it reacted (see Figure 8) though the As concentration in the solution is unaffected by the extent of the reaction.

Discussion

Overall, the trend in reactivity for the different impurity types is very similar to what was observed by Lehner et al., (2007). There are considerably more sources for error in these experiments than in the electrochemical experiments, including the potential analytical error in measuring the RPV concentrations, the pyrite surface area, weighing and loading the sample bags, and error from the changing mass of solution in the batch experiments due to the withdrawal of fluid. Nevertheless, the results are fairly consistent with the electrochemistry experiments in that the pyrite with impurities is more reactive than the undoped pyrite. The order of which impurity type is most reactive is different. In the electrochemical experiments the As-doped pyrite was always the most reactive. The Ni-doped was second most reactive most of the time, followed by the Co-doped pyrite. In this study the Co-doped pyrite most often has the highest oxidation rates but it is statistically equal with the As-doped population. The Leadville sample rate was near the top of the As-doped and Co-doped population while the Elba sample, though lower, was also in the top of the population (Figure 5).

The size of our experimental population (26) allows statistical comparison of different parameters enabling the visualization of trends that might not be apparent from fewer experiments. For example, when mixed flow rates of reaction calculated with the three different reaction progress variables are normalized to moles of pyrite oxidized according to the stoichiometry of Reaction 2, the rate of sulfate increase appears approximately an order of magnitude higher than the rates calculated from ferrous and ferric iron as RPVs. Furthermore, the rate calculated from ferrous iron as RPV is higher than the rate calculated from ferric iron as RPV. This discrepancy can be explained by the oxidation of ferrous iron by dissolved oxygen. The recycling of ferrous iron lowers both the rate of ferric iron decrease and the rate of ferrous iron increase relative to the rate of sulfate increase. Evidence for this iron recycling is the mean ratio of ferric iron decrease to ferrous iron increase. It is consistently near 0.75 when, according to

the stoichiometry of Reaction 2, it should be 0.93. The ratios between the observed rates from the three reaction progress variables can be explained if approximately 2/3 of the ferrous iron is oxidized in the mixed flow reactor experiment.

Another observation is the higher rates for batch reactor experiments than for MF experiments by a factor of about two for sulfate and ferrous iron and approximately three for ferric iron (Figure 4). One explanation is that the pyrite grains in the mixed flow reactor are stationary once the experiment begins and they react over 18 to 24 hours before the rate is measured by taking steady state fluid samples. The batch reactor is then set up and the grains are reoriented in the process of removing the bag and installing it into the batch reactor. Thus fresh surfaces that may be more reactive are exposed, and the measured rates are initial rates. Also, it is possible that there is a buildup of reaction products lodged between the grains that the stirring in the mixed flow reactor is not able to remove, but once the grains are reoriented they give up these products in the initial part of the batch experiment. This could account for the observation that the batch reaction rates calculated from a linear fit of the first four data points show almost no variability between populations, but the rates calculated from the polynomial fit over the full 65 minutes of the experiment diverge as the grain configuration and reactive surface area is exposed without disruption to the solution.

When the rates are plotted against the pyrite impurity concentration very little trend is observed for any impurity at the range of concentrations available in this study except for the rates calculated from the sulfate RPV (Figure 5); however, the amount of each impurity released to solution in the mixed flow experiments is clearly related to the pyrite impurity concentration (Figure 6).

The measured oxidation rates of natural samples with multiple impurities fall within the higher end of oxidation rates for the synthetic pyrite with impurity populations (Figure 5), while pyrite with the fewest impurities is least reactive. Therefore, our results indicate that impurities, which are nearly ubiquitous in pyrite found in all geologic settings, are in part responsible for measured pyrite reaction rates.. Mechanisms posed for pyrite oxidation that do not

account for their contribution are possibly incomplete. Of course other natural pyrite features such as inclusions, cracks, and secondary sulfide phases also influence oxidation rates. However, in prior studies, this was usually addressed by choosing high quality pyrite grains. Studies (in progress) that use electrochemical impedance spectroscopy to compare the different pyrite populations provide further evidence that impurities in pyrite affect charge transfer, by introducing additional occupied surface states within the bandgap energy region at the pyrite/solution interface. While geologically, the difference in the reaction rate for the populations with different impurities is probably insignificant, the implication that charge transfer mechanisms may be affected by the amount and type of impurity in pyrite has important consequences for materials applications and studies addressing pyrite's possible role in the origin of life.

Conclusion

Results from the mixed flow and batch reactor experiments indicate that pyrite with As, Co, or Ni impurities oxidizes slightly faster than pyrite with very low impurity concentrations at pH 2. The results from mixed flow-through reactor experiments are more consistent than batch reactor experiments. This conclusion is in accordance with the results from electrochemical studies suggesting that bulk defect states introduced in pyrite by impurities increase the density of occupied surface states at the pyrite/electrolyte interface, and that charge transfer is mediated by the surface state concentration.

Acknowledgements

This material is based upon work supported by the National Science Foundation under Grant No. NSF-EAR 0409155. We thank Sankaran Mahadevan for support through NSF-DGE 0114329 (Integrative Graduate Education and Research Traineeship for Reliability and Risk Engineering Management -- Vanderbilt University Department of Civil and Environmental Engineering). We appreciate technical support by Alan Wiseman, Rossane DeLapp, Andrew Garrabrants, Charles Lukehart, Lang Li, and Jiang Li, and helpful discussion with John Ayers, all of Vanderbilt University. We also gratefully acknowledge contributions to sample

preparation by undergraduate students Charles Marcrum III, Stephen Arndt, Mary Dean, and Rebecca Panter.

References

Abraitis, P. K., Pattrick, R. A. D., and Vaughan, D. J., 2004, Variations in the compositional, textural and electrical properties of natural pyrite: a review: International Journal of Mineral Processing, v. 74, no. 1-4, p. 41-59.

Abrams, B. L., and Wilcoxon, J. P., 2005, Nanosize Semiconductors for Photooxidation.: Critical Reviews in Solid State & Materials Science, v. 30, no. 3, p. 153-182.

Bailey, L. K., and Peters, E., 1976, Decomposition of pyrite in acids by pressure leaching and anodization: The case for an electrochemicla mechanism: Canadian Metalurgy Quarterly, v. 15, p. 333-344.

Becker, U., Rosso, K. M., and Hochella, J., Michael F., 2001, The proximity effect on semiconducting mineral surfaces: a new aspect of mineral surface reactivity and surface complexation theory?: Geochimica et Cosmochimica Acta, v. 65, no. 16, p. 2641-2649.

Bither, T. A., Bouchard, R. J., Cloud, W. H., Donohue, P. C., and Siemons, W. J., 1968, Transition metal pyrite dichalcogenides, high-pressure synthesis and correlation of properties: Inorganic Chemistry, v. 7, p. 2208-2220.

Blochl, E., Keller, M., Wachtershauser, G., and Stetter, K. O., 1992, Reactions Depending on Iron Sulfide and Linking Geochemistry with Biochemistry: Proceedings of the National Academy of Sciences of the United States of America, v. 89, no. 17, p. 8117-8120.

Bronold, M., Tomm, Y., and Jaegermann, W., 1994, Surface states on cubic d-band semiconductor pyrite (FeS2): Surface Science, v. 314, no. 3, p. L931-L936.

Brown, A. D., and Jurinak, J. J., 1989, Mechanism of Pyrite Oxidation in Aqueous Mixtures: Journal of Environmental Quality, v. 18, no. 4, p. 545-550.

Chandler, R. N., and Bene, R. W., 1973, EPR study of the solid solutions $Ni_xFe_{1-x}S_2$, $Co_xFe_{1-x}S_2$, and $Co_xNi_yFe_{1-x-y}S_2$: Physical Review B., v. 8, no. 11, p. 4979-4988.

Chernyshova, I. V., 2003, An in situ FTIR study of galena and pyrite oxidation in aqueous solution: Journal of Electroanalytical Chemistry, v. 558, p. 83-98.

Chongyang, L., Pettenkoffer, C., and Tributsch, H., 1988, Enhancement of photoactivity in pyrite (FeS_2) interfaces by photoelectrochemical processes: Surface Science, v. 204, p. 537-554.

Doyle, C. S., Kendelewicz, T., Bostick, B. C., and Brown, G. E., 2004, Soft X-ray spectroscopic studies of the reaction of fractured pyrite surfaces with Cr(Vl)-containing aqueous

solutions: Geochimica Et Cosmochimica Acta, v. 68, no. 21, p. 4287-4299.

Druschel, G., and Borda, M., 2006, Comment on "Pyrite dissolution in acidic media" by M. Descostes, P. Vitorge, and C. Beaucaire: Geochimica Et Cosmochimica Acta, v. 70, no. 20, p. 5246-5250.

Eggleston, C. M., Ehrhardt, J.-j., and Stumm, W., 1996, Surface structural controls on pyrite oxidation kinetics: An XPS-UPS, STM, and modeling study: American MIneralogist, v. 81, no. Sept-Oct, p. 1036-1056.

Ennaoui, A., Schlichthorl, G., Fiechter, S., and Tributsch, H., 1992, Vapor phase epitaxial growth of FeS_2 pyrite and evaluation of the carrier collection in liquid-junction solar cell: Solar Energy Materials and Solar Cells, v. 25, p. 169-178.

Evangelou, V. P., and Zang, Y. L., 1995, A review: pyrite oxidation mechanisms and acid mine drainage prevention: Critical Reviews in Environmental Science and Technology, v. 25, no. 2, p. 141-199.

Eyert, V., Hock, K. H., Fiechter, S., and Tributsch, H., 1998, Electronic structure of FeS_2: The crucial role of electron-lattice interaction: Physical Review B., v. 57, no. 11, p. 6350-6359.

Fan, F. R., and Bard, A. J., 1991, Scanning Tunneling Microscopy and Tunneling Spectroscopy of N-Type Iron Pyrite (N-Fes2) Single-Crystals: Journal of Physical Chemistry, v. 95, no. 5, p. 1969-1976.

Fleischer, M., 1955, Minor elements in some sulfide minerals: Economic Geology, v. 50, p. 970-1024.

Gao, P., Xie, Y., Ye, L., Chen, Y., and Guo, Q., 2006, From 2D Nanoflats to 2D Nanowire Networks: A Novel Hyposulfite Self-Decomposition Route to Semiconductor FeS₂ Nanowebs: Crystal Growth & Design, v. 6, no. 2, p. 583-587.

Hicyilmaz, C., Altun, N. E., Ekmekci, Z., and Gokagac, G., 2004, Pyrite-DTPI interaction as a function of pulp potential and pH: Colloids and Surfaces a-Physicochemical and Engineering Aspects, v. 233, no. 1-3, p. 11-24.

Holmes, P. R., and Crundwell, F. K., 2000, The kinetics of the oxidation of pyrite by ferric ions and dissolved oxygen: an electrochemical study: Geochimica et Cosmochimica Acta, v. 64, no. 2, p. 263-274.

Huber, C., and Wachtershauser, G., 1998, Peptides by activation of amino acids with CO on (Ni,Fe)S surfaces: Implications for the origin of life: Science, v. 281, no. 5377, p. 670-672.

Kendelewicz, T., Doyle, C. S., Bostick, B. C., and Brown, G. E., 2004, Initial oxidation of fractured surfaces of FeS_2(100) by molecular oxygen, water vapor, and air: Surface Science, v. 558, no. 1-3, p. 80-88.

Kolker, A., and Huggins, F. E., 2007, Progressive oxidation of pyrite in five bituminous coal samples: An As XANES and 57Fe Mossbauer spectroscopic study: Applied Geochemistry, v. 22, no. 4, p. 778-787.

Lehner, S., Savage, K., Ciobanu, M., and Cliffel, D. E., 2007, The effect of As, Co, and Ni impurities on pyrite oxidation kinetics: An electrochemical study of synthetic pyrite: Geochimica et Cosmochimica Acta, v. 71, no. 10, p. 2491-2509.

Lehner, S. W., Savage, K. S., and Ayers, J. C., 2006, Vapor growth and characterization of pyrite (FeS2) doped with Co, Ni, and As: Variations in semiconducting properties: Journal of Crystal Growth, v. 286, no. 2, p. 306-317.

Leiro, J. A., Mattila, S. S., and Laajalehto, K., 2003, XPS study of the sulphur 2p spectra of pyrite: Surface Science, v. 547, no. 1-2, p. 157-161.

Li, E. K., Johnson, K. H., Eastman, D. E., and Freeouf, J. L., 1974, Localized and bandlike valence-electron states in FeS_2 and NiS_2: Physical Review Letters, v. 32, no. 9, p. 470-472.

Luther, I., George W., 1987, Pyrite oxidation and reduction: Molecular orbital theory considerations: Geochimica et Cosmochimica Acta, v. 51, no. 12, p. 3193-3199.

Manaka, M., 2007, Comparison of rate laws for the oxidation of five pyrites by dissolved oxygen in acidic solution: Journal of Mineralogical and Petrological Sciences, v. 102, no. 1, p. 24-38.

Mattila, S., Leiro, J. A., and Heinonen, M., 2004, XPS study of the oxidized pyrite surface: Surface Science, v. 566, p. 1097-1101.

Mattila, S., Leiro, J. A., and Laajalehto, K., 2003, Surface XPS core-level shifts of FeS_2: Applied Surface Science, v. 212-213, p. 97-100.

McKibben, M. A., and Barnes, H. L., 1986, Oxidation of pyrite in low temperature acidic solutions: Rate laws and surface textures: Geochimica et Cosmochimica Acta, v. 50, no. 7, p. 1509-1520.

Mishra, K. K., and Osseo Asare, K., 1992, Fermi Level Pinning at Pyrite (FeS_2) Electrolyte Junctions: Journal of the Electrochemical Society, v. 139, no. 3, p. 749-752.

Moses, C. O., and Herman, J. S., 1991, Pyrite oxidation at circumneutral pH: Geochimica et Cosmochimica Acta, v. 55, no. 2, p. 471-482.

Moses, C. O., Kirk Nordstrom, D., Herman, J. S., and Mills, A. L., 1987, Aqueous pyrite oxidation by dissolved oxygen and by ferric iron: Geochimica et Cosmochimica Acta, v. 51, no. 6, p. 1561-1571.

Nesbitt, H. W., Berlich, A. G., Harmer, S. L., Uhlig, I., Bancroft, G. M., and Szargan, R., 2004, Identification of pyrite valence band contributions using synchrotron-excited X-ray

photoelectron spectroscopy: American Mineralogist, v. 89, no. 2-3, p. 382-389.

Nesbitt, H. W., Scaini, M., Hochst, H., Bancroft, G. M., Schaufuss, A. G., and Szargan, R., 2000, Synchrotron XPS evidence for Fe^{2+}-S and Fe^{3+}-S surface species on pyrite fracture-surfaces, and their 3D electronic states: American Mineralogist, v. 85, no. 5-6, p. 850-857.

Nesbitt, H. W., Uhlig, I., Bancroft, G. M., and Szargan, R., 2003, Resonant XPS study of the pyrite valence band with implications for molecular orbital contributions: American Mineralogist, v. 88, no. 8-9, p. 1279-1286.

Nicholson, R. V., Gillham, R. W., and Reardon, E. J., 1988, Pyrite oxidation in carbonate-buffered solution: 1. Experimental kinetics: Geochimica et Cosmochimica Acta, v. 52, no. 5, p. 1077-1085.

-, 1990, Pyrite oxidation in carbonate-buffered solution: 2. Rate control by oxide coatings: Geochimica et Cosmochimica Acta, v. 54, no. 2, p. 395-402.

Nordstrom, D. K., 1977, Thermochemical redox equilibria of ZoBell's solution: Geochimica et Cosmochimica Acta, v. 41, p. 1835-1841.

Palache, C., Berman, H., and Frondel, C., 1944, The System of Mineralogy of James Dwight Dana and Edward Salisbury Dana Yale University 1837-1892: New York, John Wiley and Sons, INC, 834 p.

Parkhurst, D. L., and Appelo, C. A. J., 1999, User's guide to PHREEQC (version 2); a computer program for speciation, batch-reaction, one-dimensional transport, and inverse geochemical calculations: U. S. Geological Survey, WRI 99-4259.

Reich, M., and Becker, U., 2006, First-principles calculations of the thermodynamic mixing properties of arsenic incorporation into pyrite and marcasite: Chemical Geology, v. 225, no. 3-4, p. 278-290.

Rimstidt, J. D., and Newcomb, W. D., 1993, Measurement and analysis of rate data: The rate of reaction of ferric iron with pyrite: Geochimica et Cosmochimica Acta, v. 57, no. 9, p. 1919-1934.

Rimstidt, J. D., and Vaughan, D. J., 2003, Pyrite oxidation: a state-of-the-art assessment of the reaction mechanism: Geochimica et Cosmochimica Acta, v. 67, no. 5, p. 873-880.

Rosso, K. M., and Becker, U., 2003, Proximity effects on semiconducting mineral surfaces II: : Distance dependence of indirect interactions: Geochimica et Cosmochimica Acta, v. 67, no. 5, p. 941-953.

Rosso, K. M., Becker, U., and Hochella, J., Michael F., 2000, Surface defects and self difusion on pyrite {100}: An ultra-high vacuum scanning tunneling microscopy and theoretical modeling study: American MIneralogist, v. 85, p. 1428-1436.

Schaufu[ss], A. G., Nesbitt, H. W., Kartio, I., Laajalehto, K., Bancroft, G. M., and Szargan, R., 1998, Reactivity of surface chemical states on fractured pyrite: Surface Science, v. 411, no. 3, p. 321-328.

Shuey, R. T., 1975, Semiconducting Ore Minerals, Developments in Economic Geology, 4: Amsterdam, Elsevier Scientific Publishing Co.

Singer, P. C., and Stumm, W., 1970, Acidic Mine Drainage: The Rate-Determining Step: Science, v. 167, no. 3921, p. 1121-1123.

Tao, D. P., Richardson, P. E., Luttrell, G. H., and Yoon, R. H., 2003, Electrochemical studies of pyrite oxidation and reduction using freshly-fractured electrodes and rotating ring-disc electrodes: Electrochimica Acta, v. 48, no. 24, p. 3615-3623.

Taylor, B. E., Wheeler, M. C., and Nordstrom, D. K., 1984, Stable isotope geochemistry of acid mine drainage: Experimental oxidation of pyrite: Geochimica et Cosmochimica Acta, v. 48, no. 12, p. 2669-2678.

Tributsch, H., Fiechter, S., Jokisch, D., Rojas-Chapana, J., and Ellmer, K., 2003, Photoeletrochemical power, chemical energy and catalytic activity for organic evolution on natural pyrite interfaces: Origins of Life and Evolution of the Biosphere, v. 32, p. 129-162.

Uhlig, I., Szargan, R., Nesbitt, H. W., and Laajalehto, K., 2001, Surface states and reactivity of pyrite and marcasite: Applied Surface Science, v. 179, no. 1-4, p. 223-230.

Wachtershauser, G., 1988, Pyrite Formation, the 1st Energy-Source for Life - a Hypothesis: Systematic and Applied Microbiology, v. 10, no. 3, p. 207-210.

-, 1990, The Case for the Chemoautotrophic Origin of Life in an Iron- Sulfur World: Origins of Life and Evolution of the Biosphere, v. 20, no. 2, p. 173-176.

-, 1993, The Cradle Chemistry of Life - on the Origin of Natural- Products in a Pyrite-Pulled Chemo-Autotrophic Origin of Life: Pure and Applied Chemistry, v. 65, no. 6, p. 1343-1348.

-, 1997, The origin of life and its methodological challenge: Journal of Theoretical Biology, v. 187, no. 4, p. 483-494.

Wan, D., He, Q., Zhang, L., Jia, Q., Zhang, R., Zhang, H., Wang, B., and Wei, L., 2004, Study on pyrite FeS2 films deposited on Si(1 0 0) substrate by synchrotron radiation surface X-ray diffraction method: Journal of Crystal Growth, v. 268, no. 1-2, p. 222-226.

Wan, D., Wang, Y., Wang, B., Ma, C., Sun, H., and Wei, L., 2003, Effects of the crystal structure on electrical and optical properties of pyrite FeS2 films prepared by thermally sulfurizing iron films: Journal of Crystal Growth, v. 253, no. 1-4, p. 230-238.

Wan, D., Wang, Y., Zhou, Z., Yang, G., Wang, B., and Wei, L., 2005, Fabrication of the or-

dered FeS2 (pyrite) nanowire arrays in anodic aluminum oxide: Materials Science and Engineering: B, v. 122, no. 2, p. 156-159.

Wang, X. H., 1996, Interfacial electrochemistry of pyrite oxidation and flotation .1. Effect of borate on pyrite surface oxidation: Journal of Colloid and Interface Science, v. 178, no. 2, p. 628-637.

Wei, D., and Osseo-Asare, 1996, Semiconductor electrochemistry of particulate pyrite: Dissolution via hole and electron pathways: Journal of the Electrochemical Society: Electrochemical Science and Technology, v. 143, no. 10, p. 3192-3198.

Wei, D., and OsseoAsare, K., 1997, Semiconductor electrochemistry of particulate pyrite; mechanisms and products of dissolution: Journal of the Electrochemical Society: Electrochemical Science and Technology, v. 144, no. 2, p. 546-553.

Wiersma, C. L., and Rimstidt, J. D., 1984, Rates of reaction of pyrite and marcasite with ferric iron at pH 2: Geochimica et Cosmochimica Acta, v. 48, no. 1, p. 85-92.

Williamson, M. A., and Rimstidt, J. D., 1994, The kinetics and electrochemical rate-determining step of aqueous pyrite oxidation: Geochimica et Cosmochimica Acta, v. 58, no. 24, p. 5443-5454.

Zhao, G. L., Callaway, J., and Hayashibara, M., 1993, Electronic structures of iron and cobalt pyrites: Physical Review B., v. 48, no. 21, p. 15781-15786.

CHAPTER IV

ELECTROCHEMICAL IMPEDANCE SPECTROSCOPY OF SYNTHETIC PYRITE DOPED WITH AS, CO, AND NI: THE EFFECT OF IMPURITIES ON CHARGE TRANSFER KINETICS

Abstract

Electrochemical impedance spectroscopy data were collected in pH 1.87 HCl solution with 0.005 M ferric and 0.005 M ferrous iron on a set of synthetic pyrite electrodes previously studied with cyclic and AC voltammetry. The electrodes were either undoped or doped with As, Co, or Ni. Data was also collected on 5 natural pyrite samples. All the EIS spectra were modeled with the equivalent circuit: $R_1(Q_1R_2)(Q_2(C_1(C_2(R_3W))))$ where R_1 is solution/sample resistance, Q_1 is space charge/Hemholtz capacitance, R_2 is charge transfer resistance, Q_2 is frequency dependent surface state capacitance, C_1 is pure surface state capacitance, C_2 is secondary faradaic pseudo-capacitance, R_3 is secondary faradaic resistance, and W is Warburg impedance. The electrodes were grouped according to their response to AC voltammetry and according to dopant type for statistical comparison of the equivalent circuit element values. In light of previous work, evidence suggests that defect states in the bulk pyrite arising from impurity atoms become surface states at the interface and affect oxidation kinetics by mediating charge transfer. Charge transfer resistance is greatest for electrodes that respond with higher current to AC voltammetry scans at 100 Hz. A two step charge transfer mechanism with carrier recombination mediated by surface states is proposed.

Introduction

Pyrite (FeS_2), being the most abundant sulfide phase near Earth's surface, has been extensively studied for its role in the production of acid drainage from mining wastes as well as for applications in photovoltaic cell and battery design. Pyrite is a semiconductor with a band gap of 0.95 eV and commonly contains As, Co, and Ni as trace element impurities. We have synthesized large crystals with chemical vapor transport and performed solid state character-

ization of these doped and undoped pyrite crystals. This has revealed systematic differences in the semiconducting electrical properties associated with each of these impurities (1).We then studied the oxidation kinetics of pyrite with no added impurities and pyrite doped with As, Co, and Ni in an ongoing effort to understand the effect of common impurities on pyrite acid producing potential (2).

Acid production from the aqueous oxidation of pyrite accelerates below pH 3 where ferric iron becomes the dominant oxidant (3, 4). We have studied the kinetics of this reaction with cyclic and AC voltammetry (2) as well as with batch and flow-through reactor kinetic experiments (5). The electrochemical investigation revealed that pyrite oxidizes faster when impurities are present and the rate is fastest when As is present followed by Ni and Co. The results from batch and flow-through experiments were similar to the electrochemical results except that pyrite with As and Co impurities were equally reactive followed by Ni-doped and undoped pyrite.

In order to gain more insight into the mechanism by which these impurities are affecting charge transfer at the pyrite/electrolyte interface, we have gathered electrochemical impedance spectroscopy (EIS) data on electrodes previously studied with AC and cyclic voltammetry. Our analysis of this data along with evidence form the earlier study suggest that impurity atoms introduce defect states in the bulk pyrite that manifest as increased surface state concentration at the semiconductor/electrolyte interface and that charge transfer is mediated by these surface states.

The effect of As, Co and Ni impurities on surface state energy

Impurities may increase the reactivity of pyrite by introducing bulk defect states within the forbidden zone that, at the pyrite surface, increase the density of occupied surface states within the bandgap energy. Evidence for this can be seen in the respective behavior of Co- and Ni-doped pyrite. Electron paramagnetic resonance studies (6) suggest that Ni and Co substituting for Fe in the pyrite structure introduce defect states at different energy levels within the

forbidden zone. The Co defect state with a donor electron occurs high in the band gap, near or possibly overlapping the conduction band energy, so that the extra electrons easily move into the conduction band. This is reflected in the high mobility, high carrier concentration, and low resistivity of Co-doped pyrite (1). The Ni defect state with two donor electrons occurs near the middle of the band gap where it is energetically unfavorable for the electrons to enter the conduction band. The Ni defect states are most likely filled due to their distance from the conduction band and this is reflected in low carrier concentration measured for Ni-doped pyrite. When these defect states intersect with the surface they become surface states. Therefore, we would expect to see higher intra-band gap occupied surface state density in the Ni-doped pyrite. We reported evidence suggesting this is the case (2).

Arsenic substituting for S in the pyrite structure introduces a vacant defect state low in the band gap which may become populated by valence band electrons, leaving holes for charge carriers (7). As-doped synthetic pyrite is most often p-type, i.e., has holes for charge carriers (1) as is natural pyrite with As as the main impurity (8, 9). At the pyrite surface this defect state may also introduce additional occupied surface states within the band gap. We have observed higher response to AC voltammetry for As-doped and Ni-doped pyrite than for undoped and Co-doped pyrite, suggesting that the intra-band-gap defect states resulted in higher occupied surface state density and increased charge transfer (2).

The evidence from the solid state electrical characterization, combined with AC and cyclic voltammetry, plus results of other studies (6, 10), seem to confirm that defect states within the band gap introduced by impurities substituting for iron and sulfur in the pyrite crystal structure to affect the surface state concentration and energy at the electrolyte-semiconductor interface, leading in some cases to Fermi level pinning (2). The surface state concentration seems to be positively correlated with reactivity or charge transfer. EIS is a tool well suited to increase understanding of this relation and to further investigate charge transfer in this system. Therefore, we have gathered EIS spectra on a previously studied (2) set of the pyrite electrodes as well as on additional electrodes prepared from natural pyrite.

The mathematical analysis of EIS data can be very complex and therefore the interpretation of results usually takes the form of empirical fitting of the data to an equivalent circuit model. The circuit elements are then related to physical phenomena, often with the help of other analytical techniques and theory. It has been recognized that ideal circuit elements such as pure resistance, capacitance or inductance are often inadequate to fit experimental data from semiconductors (11-13). It is also well accepted that the surface of semiconductors is characterized by a region of charge depletion, known as the space charge layer or depletion region, which may behave as a parallel plate capacitor. Much work has been done on the role of surface electronic states within the semiconductor bandgap energy (12, 14-23). Surface states are thought to serve as a conduit for charge transfer and as recombination centers for minority carrier capture (14). Surface states have been modeled by a series capacitance and resistance in parallel to the depletion layer or space charge capacitance.

Semiconductor experimental data is often best modeled with frequency-dependent elements referred to as constant phase elements (CPE or Q). In studying materials for photogeneration of electricity, materials scientists have made significant progress in understanding charge transfer at semiconductor/electrolyte interfaces. In particular, the role of surface states, the physical interpretation of CPE's, and dissolution behavior are addressed in a review by Gomes and Vanmaekelelberg (12).

There is a substantial body of literature on the characterization of the semiconductor/electrolyte interface with electrochemical techniques including the development of equivalent circuit models for EIS data and their physical interpretation. Also, there have been a number studies using EIS to investigate the mechanisms and kinetics of pyrite oxidation. However, most of the pyrite EIS studies have not considered the semiconducting nature of pyrite and therefore have not incorporated theory from semiconductor electrochemistry. They have been done at pH 9.2 and 9.3 (11, 24), seeking to understand processes critical to ore refinement and recovery of precious metals in contrast to studies at low pH aimed at understanding mechanisms of acid production for environmental remediation.

Pang et al. (24) studied the pyrite/solution interface in sodium carbonate solution at pH 9.3 during galvanic oxidation of the pyrite electrode with EIS. They report that the impedance spectra and thus the electrical properties of the interface change as the oxidation proceeds. They attribute the change at the interface to the build-up of a porous Fe and S rich coating of reaction products. They were able to fit their data with a number of equivalent circuits using elements such as pore resistance, coating layer capacitance, double layer capacitance, constant phase elements due to surface roughness and Warburg diffusion, but no circuit elements were attributed to the semiconductor depletion layer or to surface states. The semiconductor nature of pyrite was not considered.

Velasquez et al. (11) investigated both pyrite and chalcopyrite with surface characterization and electrochemical techniques including EIS in a borate buffer solution at pH 9.2. They gathered impedance spectra at different potentials where, according to cyclic voltammetry curves, electro-dissolution and electro-reduction were interpreted to be taking place. The parameters of the equivalent circuit models and the models themselves changed depending on the potential set for the scan, as expected. The elements that were interpreted to be capacitances were modeled with constant phase elements. Like Pang et al. (1990), they interpret a coating layer capacitance-CPE, pore resistance, charge transfer resistance, double layer capacitance-CPE, Warburg impedance and adsorption impedance but neglect pyrite semiconducting properties.

Lin and Say (25) performed cyclic voltammetry and EIS on pyrite electrodes in a 4.5 M NaCl solution with 0.5M HCl. EIS scans were performed at 0.9 and 1.1V vs SHE based on two reactions interpreted to be occurring from the cyclic voltammetry scans. The first was a direct oxidation of pyrite S (-1) to S^o and the second reaction was the oxidation of the elemental sulfur to sulfate. They postulated an equivalent circuit that included solution resistance, resistance to assumed reactions, a capacitance referred to as the pseudo-capacitance of a surface film, and a double layer capacitance. Instead of a constant phase element they added a corrective resistance to account for uneven distribution of the electrical field. This resistance contained a constant

that was related to the angle of depression of the impedance semicircle. None of the circuit elements were attributed to a depletion region or surface states. Although they mention the semiconducting nature of pyrite, they speculate that semiconducting properties are unlikely to have a significant impact on AC impedance measurements when a large potential is applied to the electrode.

In contrast, Gomes and Vanmaekelbergh (12) review impedance spectroscopy at semiconductor electrodes such as GaAs, CdS and CdSe. They and Morrison (26), report that the double layer capacitance on the electrolyte side of the semiconductor interface is very large and thus can be ignored as an element in semiconductor equivalent circuit models. Therefore, the capacitive reactance in a simple semiconductor system is primarily due to the depletion layer capacitance and the pseudo-capacitance of the faradaic process.

We have studied synthetic undoped pyrite and pyrite doped with As, Co, and Ni, as well as three natural pyrite samples from Leadville, CO found to contain primarily As, Pb, Ag, and Bi impurities, using cyclic, AC and potential step voltammetry (2). We reported highest reactivity for As-doped pyrite followed by Ni- and Co-doped pyrite. We observed that some electrodes respond well to the AC voltammetry at 100 Hz while others do not. An AC response score was calculated as: $\frac{|i_P - i_{B_P}|}{|i_{B_1} - i_{B_2}|}$ where i_P is the peak current value, i_B represents the background current with B_1 being the background current at the beginning of the scan, B_2 the background current at the end of the scan and B_P the background current at the peak potential. If the value was less than one, the magnitude of the AC peak was less than the background fluctuation. The magnitude or lack of AC response was used to compare the reactivity of different electrodes and pyrite types.

To calculate k^o, the standard heterogeneous rate constant, from the phase angle we subtracted the non-faradaic capacitance of the electrodes measured in 0.1 M KCl solution without the redox couple. For many electrodes this method led to an underestimation of the non-faradaic impedance and the phase angle correction gave meaningless values. We postulated the difference in behavior among the electrodes as being related to differing surface state density.

We also correlated semiconducting properties of doped pyrite with oxidation behavior, further suggesting that surface states are an important component of charge transfer across the pyrite/solution interface at low pH (2).

Though pyrite oxidation can most likely proceed by several pathways or mechanisms, over 50 years of oxidation experiments suggest that, at pH below 3, ferric iron is the primary oxidant and pyrite oxidation is primarily an electrochemical reaction (27). We have gathered EIS data and performed our previous studies in solutions near pH 2 simulating the acid mine drainage environment. The results of the current study indicate that the semiconducting nature of pyrite is central to understanding its oxidation behavior.

Methods

Samples

Both natural and synthetic pyrites were used in this study. Most samples were synthesized in our laboratory, where pyrite crystals are grown with chemical vapor transport in sealed evacuated quartz tubes in a temperature gradient of 700 to 550 °C over 16 cm using $FeBr_3$ as a transport agent (1). The synthesized pyrite was doped with either As, Co, Ni or nothing at all (Table 1). Also, five samples of natural pyrite were studied, which have been described further in Savage et al. (9). Pyrite from the Black Cloud Mine (Leadville, CO) found to contain primarily As, Pb, and Bi impurity was also used in previous studies (2, 5, 9). The other four consist of a sample from Brazil containing approximately equal concentration by mass of Co and As, a sample from Missouri with a larger molar concentration of Ni but with significant Co and As, and two samples from the Vanderbilt collection of unknown origin; one Vanderbilt contained all three impurities but was dominated by Co, and the other contained low amounts of impurities but was dominated by As (see Table 2). Crystals that were at least 2 mm in two dimensions were mounted in epoxy and cut into sections approximately 1 mm thick with a slow speed diamond saw.

Composition

The thick sections were analyzed for dopant concentration using laser ablation inductively coupled plasma mass spectrometry (LA-ICPMS) with a New Wave UP 213 laser ablation system coupled with a Perkin Elmer Elan Dynamic Reaction Chamber ICPMS using Ar plasma. Laser ablation scans were typically collected along a line from the epoxy near the edge of the mounted crystal to the center of the specimen. The scans were pre-ablated at 50% power at a rate of 70 μm/sec over a swath of 160 μm width to remove any residue. The analysis scan ablated an 80 μm swath down the middle of the pre-ablation path at a rate of 10 μm/sec at 65% power (2). Concentration and error were calculated as described in (1) using a United States Geological Survey prepared sulfide standard (28).

Bulk electrical properties

The resistivity, carrier concentration, and mobility were measured by a four probe van der Pauw/Hall set up as described in (1). For the electrical measurement, the mounted pyrite surface was cleaned with methanol and left rough to facilitate ohmic contact with the gold probes. To ensure repeatability, a series of 6 to 12 measurements was performed. To avoid distortion from applying more current than the sample could conduct, the current was increased in equal steps through an order of magnitude in range ending approximately 50% below the maximum current that the sample would transmit, with applied potentials of up to 2.4 V.

Electrochemical cell and electrode preparation

The solution was prepared by mixing equimolar amounts of ferric and ferrous chloride in a 0.1 M KCl solution acidified to pH 1.87 with HCl. The solution was analyzed with a Hach Dr2400 spectrophotometer for ferric and ferrous iron and was found to be 0.0005 M in each. Electrochemical experiments were conducted in a standard three electrode cell with approximately 4 mL of solution. The counter electrode was a platinum wire mesh. The reference electrode was the Ag/AgCl, 3M KCl. The working electrode, counter electrode and reference

electrode were each situated against the edge of the beaker to insure the same spatial relation in each experiment, resulting in a distance between any two electrodes of approximately one centimeter. All voltages reported in this manuscript are reported versus Ag/AgCl, 3M KCl. The pyrite working electrode was formed from previously analyzed thick sections by attaching copper wires with silver epoxy. The surface to which the wires were attached was first cleaned and etched for several hours with a 50% solution of H_2SO_4 or HCl. Once the epoxy had set, the back of the electrode with the contact was enclosed in sealing epoxy followed by silicone aquarium sealant, leaving only one surface of the pyrite in contact with the solution in the electrochemical cell. The exposed surface was polished to 3 μm roughness with 600 grit silicon carbide sandpaper followed by a 3 μm diamond polishing compound. The flat surface area was calculated from digital photographs of the electrodes next to a precision scale.

Impedance measurements

Electrochemical measurements were made with a CHI660 potentiostat controlled by CHI version 5.02 software. The cyclic voltammetry (CV) was performed over the potential region of 0 to 1.1 V with a scan rate of 0.01 V s^{-1}. The initial scan polarity was positive and the sampling interval was 0.001 V. The EIS was performed at a DC potential of 0.1V over the frequency range of 10^{-4} to 10^{5} Hz with an amplitude of 0.005 V. The preparation consisted of re-polishing the electrode with 3 μm diamond paste for approximately 5 minutes. The electrode was then washed in alconox solution and rinsed with acetone followed by de-ionized water. This washing and rinsing sequence was performed twice followed by wiping with a fresh Kim-wipe™. The electrodes were then etched with 50% HCl solution for 5 minutes after which they were again rinsed with de-ionized water and placed in the electrochemical cell. The procedure for these measurements was to polish, wash, and etch the pyrite electrode followed by the CV scan which had the effect of electrochemically etching the pyrite. Then the EIS scan was performed.

Equivalent circuit analysis

The impedance data was modeled to an equivalent circuit (EC) using the software program Zsimpwin 3.21(29) after subtracting the background impedance. The software uses a non-linear least squares fitting procedure. The background impedance was acquired by running an impedance scan 6 times with the electrode leads short circuited and then using the average value. The circuit model was arrived at by an iterative process of empirical fitting of the data combined with trial of circuits and circuit elements chosen from theoretical considerations.

The first approach was to let all parameters float and to try as many plausible circuits as possible looking for the closest fit and lowest χ^2 value. χ^2 is the sum of the squares of the residuals from the least squares fitting procedure. Once the simplest circuit was found that consistently fit all the electrodes, the model was constrained by the measured solution resistance. The value for the solution resistance was taken from the intercept of the high frequency impedance data with the Z_{real} axis of the Nyquist plot (Figure 1). Next the model was constrained by the best estimate of the charge transfer resistance by extrapolating the intersection of the impedance data with the low frequency Z_{real} axis (30). Model fits that gave unreasonable parameter values were rejected. In some cases the inner faradaic resistance and Warburg impedance were fit with unrealistically high values in which case one or the other was constrained by trial and error until the best fit was obtained. The other values were allowed to float. All data was normalized to the planar surface area of the electrode.

Data analysis

The synthetic electrodes were categorized as populations according to three different criteria: by dopant type, by their high or low response to AC voltammetry in (2) and by whether or not the non-faradaic impedance was successfully subtracted from the AC voltammetry data from the previous study to yield the peak phase angle of the ferric iron reduction reaction (2) (Appendix II). Samples with impurity concentrations less than 50 ppm were grouped with

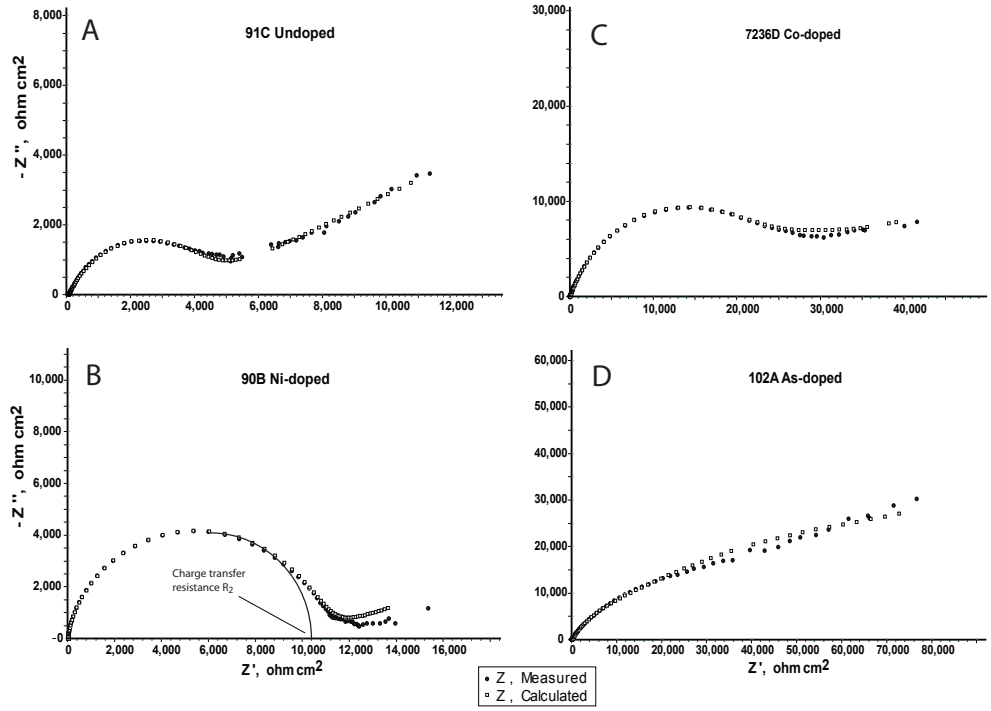

Figure 1. Nyquist plots showing the fit of the equivalent circuit model to the impedance data. The closed circles are the measured data and the open squares are the calculated fit. The solid line intersecting the Zreal axis is an example of the extrapolation of the semi-circle to obtain the charge transfer resistance. Values for other elecrodes constrained by the fitting procedure. A. Undoped sample. B. Ni-doped sample. C. Co-doped sample. D. As-doped sample.

undoped samples in statistical comparisons. There were 6 undoped, 4 Ni-doped, 3 Co-doped, and 5 As-doped synthetic electrodes. There were 14 electrodes with high AC response including the Leadville natural sample and 5 with low AC response. There were 9 electrodes each with corrected and uncorrected phase angles. The respective populations were analyzed with statistical software to determine the significance of observed differences in values of the EC parameters.

Results and discussion

The resulting equivalent circuit $R_1(Q_1R_2)(Q_2(C_1(C_2(R_3W))))$ (Figure 2) is similar to equivalent circuits showing two faradaic processes (11, 24, 31, 32). It is also similar to some circuits proposed by Oskam et al. (20) who modeled carrier recombination via introduced

gold-related surface states on p-GaAs electrodes. In our model, the charge transfer resistance R_2 is in parallel with a CPE, in series with the solution resistance and the remaining circuit described above. However, since the capacitance C_1 is in parallel with Q_2, we speculate that Q_2

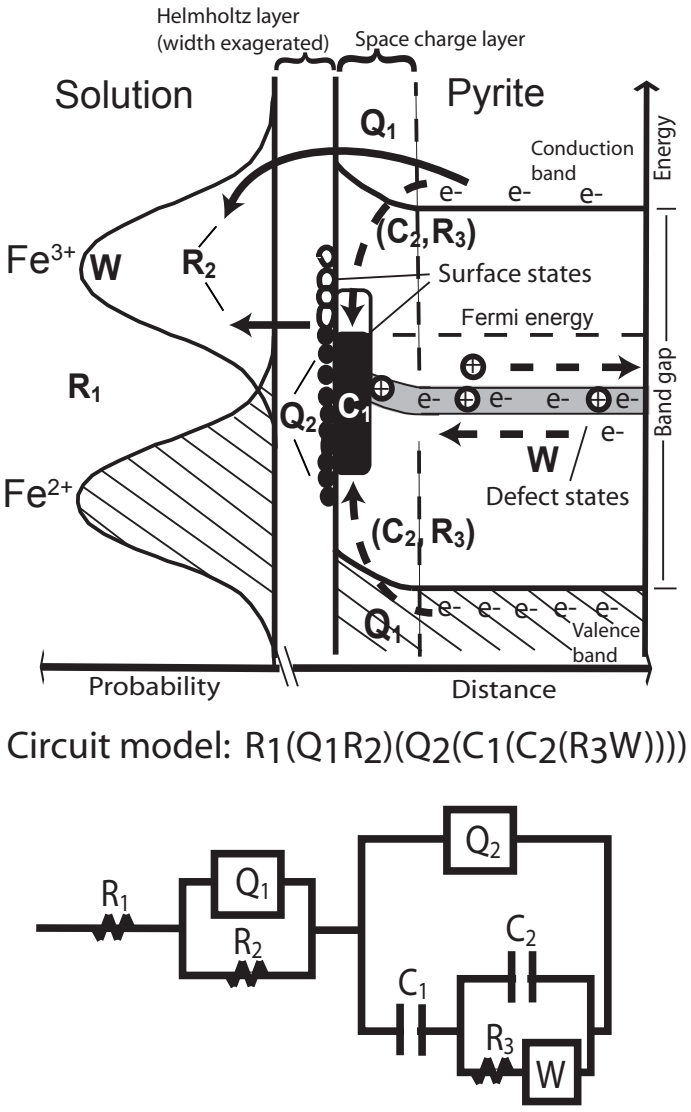

Figure 2. Schematic relating the equivalent circuit elements to physical components and processes. The equivalent circuit is below the Gerischer diagram depicting a Ni-doped pyrite/solution interface. Energy is on the Y axis and the X-axis is split between distance on the pyrite electrode side and probability on the solution side. The bell curves represent the distribution of allowed energy levels of the oxidized and reduced iron species in solution. The grey-shaded area represents the bulk defect state in the center of the bandgap energy of the Ni-doped pyrite. The solid arrows indicate charge transfer between the pyrite and solution while the dashed arrows indicate charge transfer between the bulk pyrite and the surface states.

Table 1. EIS model parameters for synthetic pyrite

Model R(QR)(Q(C(C(RW)))) synthetic pyrite

Electrode	Impurity (ppm)	Error (ppm)	R_1 (ohms-cm^2)	Q_1 (S*s^{n}cm^{-2})	(n)	R_2 (ohms-cm^2)	Q_2 (S*s^{n}cm^{-2})	(n)	C_1 F cm^{-1}	C_2 F cm^{-1}	R_3 (ohms-cm^2)	Warburg, Yo (S*s$^{0.5}$cm^{-2})	X^2	Bulk R (ohms-cm^2)
Un 7280B, As	4	1	38.84	2.1E-04	0.59	33700	5.7E-05	0.25	2.8E-05	5.9E-06	18.15	6.36E-02	9.97E-03	17
Un 72, Ni	4	0.4	21.38	1.1E-04	0.70	13000	7.7E-04	0.30	1.1E-02	1.9E-07	505.20	8.85E-07	2.32E-03	12
Un 7279B, As	5	1	29.32	1.5E-04	0.78	30000	6.6E-05	0.33	1.1E-05	1.8E-05	0.00	1.68E-03	3.00E-03	11
As T110	5	2	10.12	2.9E-04	0.66	42000	3.6E-05	0.08	2.4E-05	8.7E-06	8.73	5.64E-05	4.41E-03	1.5
As 91C	11	1	44.33	6.8E-05	0.77	3775	9.6E-04	0.28	3.4E-03	2.3E-07	27.22	4.16E-04	1.78E-03	90
As T112	35	3	13.77	4.1E-04	0.57	40000	1.5E-05	0.00	1.8E-04	9.7E-06	0.00	1.71E-05	4.71E-03	9
As 3A	100	3	24.81	3.1E-04	0.60	45000	2.3E-05	0.20	1.5E-05	2.5E-05	0.00	3.71E-05	2.37E-03	1.1
As T102A	132	5	20.78	3.5E-04	0.57	35000	8.8E-05	0.26	5.5E-05	7.7E-06	0.00	1.60E-04	9.21E-04	9
As 7332A	145	8	2.19	3.4E-04	0.95	1200	1.2E-03	0.19	4.4E-03	1.3E-04	1.33	3.96E-04	2.95E-03	6.5
As 7326	236	29	17.58	6.6E-04	0.55	36000	2.8E-05	0.08	4.4E-05	3.3E-05	0.00	6.98E-05	3.55E-03	6.5
As 7331A	251	11	31.69	8.7E-05	0.82	6451	1.1E-03	0.26	9.6E-02	3.1E-07	21.67	1.61E-02	4.74E-03	3.2
As 96B	356	48	29.21	5.2E-04	0.54	40000	1.8E-04	0.38	3.9E-05	7.6E-06	0.00	2.10E-04	2.57E-03	17
Co 7272	452	6	18.24	1.8E-03	0.50	60000	3.0E-05	0.20	4.3E-05	8.5E-06	1.00	3.90E-05	2.45E-03	0.0035
Co 7236D	507	10	9.60	4.2E-05	0.77	25000	2.4E-04	0.25	1.5E-03	4.6E-06	0.70	1.15E-02	1.77E-03	0.018
Co 7228A	1406	68	14.06	1.4E-02	0.33	5300	2.0E-04	0.05	6.0E-05	1.5E-05	0.00	2.26E-04	2.32E-03	0.0091
Ni 85B	195	6	13.76	3.0E-03	0.45	14000	7.1E-05	0.11	6.0E-05	7.8E-06	124.30	1.39E-04	1.26E-03	700
Ni 90B	1071	26	15.37	6.7E-03	0.36	10200	9.5E-05	0.03	1.2E-05	1.2E-05	488.10	1.00E-04	1.28E-03	2.2
Ni 7296	2183	30	27.79	6.9E-03	0.38	56000	3.6E-05	0.17	2.3E-05	1.0E-05	226.00	6.15E-05	1.10E-02	3.2
Ni 7290B	2812	13	11.52	6.3E-04	0.65	73000	1.9E-05	0.07	4.4E-05	1.1E-05	0.49	7.00E-05	7.10E-03	2

Table 2. EIS model parameters for natural pyrite

Model R(QR)(Q(C(C(RW)))) Natural pyrite

Electrode	1st Impurity (ppm)	2nd impurity (ppm)	3rd impurity (ppm)	R_1 (ohms-cm^2)	Q_1 (S*s^{n}cm^{-2})	(n)	R_2 (ohms-cm^2)	Q_2 (S*s^{n}cm^{-2})	(n)	C_1 F cm^{-1}	C_2 F cm^{-1}	R_3 (ohms-cm^2)	Warburg, Yo (S*s$^{0.5}$cm^{-2})	X^2 Chi^2	Bulk R (ohms-cm^2)
L3B As	As 35	Co 3	Ni 2	5.31	3.13E-04	0.94	1843.0	1.67E-03	0.29	1.60E-02	5.83E-05	3.03	5.09E-01	4.85E-03	31.4
3A Pb, Bi, As	Pb >1wt%	Bi 879	As 644	24.81	2.89E-04	0.60	71420	2.17E-05	0.17	2.25E-05	1.62E-05	0.00	2.01E-05	2.35E-03	0.66
9D Co	Co 315	As 101	Ni 2	24.60	7.69E-04	0.55	30000	8.56E-05	0.26	5.15E-05	1.14E-05	141.50	1.12E-04	8.29E-03	0.19
6000C Co	Co 3314	Ni 656	As 285	17.05	7.00E-04	0.58	28000	5.25E-05	0.10	9.04E-05	1.02E-05	1.00	1.27E-04	2.68E-03	0.01
M3F Ni	Ni 96	Co 52	As 7	43.81	5.20E-05	0.83	90000	7.73E-05	0.10	9.23E-03	1.21E-06	2.53	2.96E-04	1.32E-03	64.66

represents a non-ideal capacitance and the two elements are closely related. Therefore, our circuit is not dissimilar from a traditional two faradaic process circuit except that Q_1 and (Q_2C_1) are possible capacitances in series. R_2 is in series as it would be if it were in the position of C_1. We experimented with a resistance in the position of C_1 but the fit was not as good. Also, we experimented with many possible circuit positions for Warburg impedance but the best fit was in the inner circuit as illustrated in Figure 2. All 23 electrodes were fit to this model. The values for the parameters are given in Table 1.

The quality of the fits (see Figure 1 and Appendix II) expressed as chi-squared (χ^2) values are given in Tables 1 and 2. The χ^2 values ranged from 9.21×10^{-4} to 9.97×10^{-3} with a mean of 3.75×10^{-3} and a standard deviation of 2.75×10^{-3}. These values were not normally distributed with the distribution skewed to lower values. The median was 2.63×10^{-3}. The χ^2 values tended to be higher for the undoped and Ni-doped electrode populations as well as for the population of electrode that showed a higher AC response, and the population with corrected AC phase angles.

Pyrite oxidation mechanisms

A current hypothesis for the mechanism of pyrite oxidation by ferric iron at low pH has the electron being transferred from a dangling bond surface state on an iron atom followed by electron transfer from a sulfur atom involving attachment and degeneration of water at the sulfur site with oxygen atoms progressively bonding to the sulfur (27, 33, 34). This process is repeated until the sulfur is oxidized from a -1 to +6 valence state in sulfate with the sulfate oxygen originating in water according to:

$$FeS_2 + 14Fe^{3+} + 8H_2O = 15Fe^{2+} + 2SO_4^{2-} + 16H^+ \text{ (27)}.$$

A comprehensive review of pyrite oxidation mechanisms can be found in (5). This mechanism has two faradaic processes for each electron transferred from the pyrite.

The EC model $R_1(Q_1R_2)(Q_2(C_1(C_2(R_3W))))$ is consistent with two faradaic processes taking place (11). In terms of the above mechanism the two faradaic processes could be the

transfer of an electron from the dangling Fe^{2+} bond at the pyrite surface to the ferric ion in solution followed by the transfer of an electron from surface sulfur to the resulting Fe^{3+} atom and the attachment of H_2O. In terms of the energy band model this could be transfer of an electron from the valence band Fe 4d orbitals (hole injection) followed by charge transfer from the valence band sulfur orbitals to the Fe atom (33). However, the dangling bond Fe 4d orbital, as well as surface S orbitals, are likely to be within the band gap energy due to non-coordination from the discontinuation of the lattice at the surface (35, 36). Therefore, the above mechanism could be described as charge transfer from surface states within the band gap energy to the ferric ion in solution followed by transfer from the bulk energy bands to the surface state in a recombination reaction. If additional surface states are associated with impurities we might expect to see an increase in reactivity due to this type of mechanism.

Equivalent circuit elements

Solution sample resistance

The high frequency intersection of the impedance vector with the Z_{real} axis represents the overall cell resistance (R_1). The resistance intrinsic to the semiconductor material is measured as uncompensated solution resistance (30). Therefore, the R_1 element of the equivalent circuit is interpreted to be the solution and pyrite sample resistance. This view is bolstered by the correlation between the measured solution resistance and the solid state pyrite resistivity measured with the van der Pauw/Hall set up (Figure 3). In the case of Co-doped pyrite the bulk resistivity is on the order of 10^{-3} ohm*cm; low enough to be considered a semi-metal (1, 6). Therefore the true value of the solution resistance is likely to be near the mean for the Co-doped electrodes, about 10 to 15 ohm-cm^2. R_1 is highest for undoped pyrite and lowest for Co-doped pyrite followed by Ni-doped and then As-doped pyrite. R_1 is higher for non-corrected phase angle populations and for the population with low AC response (2). This implies that kinetic facility of the pyrite oxidation reaction may be related to the bulk resistivity of the material. However, evidence from (2) indicates that it is not a simple relationship.

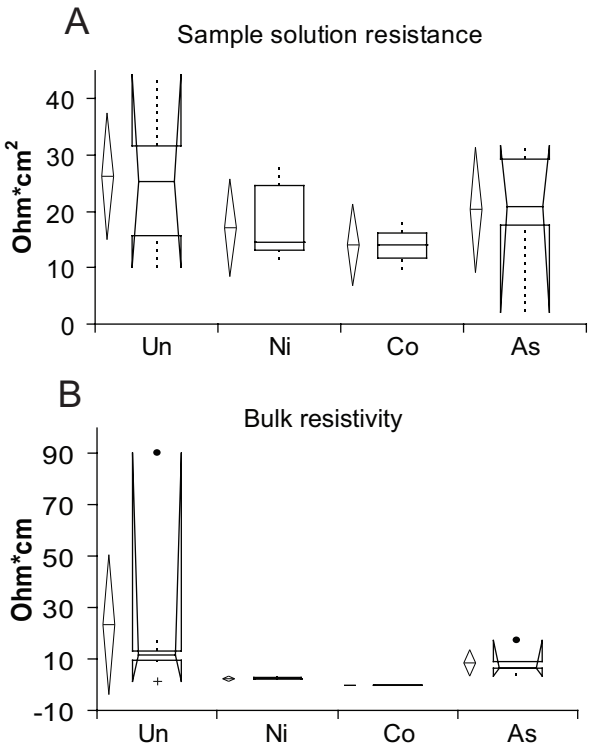

Figure 3. A. Statistical comparison of the equivalent circuit element R_1 for synthetic electrodes grouped according to dopant type. The diamonds represent the 90% confidence interval for the mean from parametric analysis. The notched box and whisper plots represent Wilcoxon signed rank test. The notch is the 90% confidence interval for the median for populations with sufficient number of samples. The top and bottom of the box represents the inter-quartile range. B. Statistical comparison of the bulk resistivity values for electrodes from (2)

The natural sample L3B with the lowest impurity concentration (Table 2) also had the lowest value for R_1 while the Ni-dominated natural sample had the highest. The As-dominated and Co-dominated natural samples were comparable to their respective synthetic counterparts. However, with few samples and factors associated with mixed impurities it is difficult to draw any conclusions concerning the natural samples.

Charge transfer to ferric iron in solution

The first process (reading the circuit from left to right) is the charge transfer from both the surface states and conduction band to the ferric ions in solution (Q_1 and R_2). The other faradaic process, represented by the inner circuit containing elements C_2, R_3, and the Warburg

impedance (Figure 2), is interpreted as being associated with a charge transfer reaction (carrier recombination) taking place between the surface states and the bulk pyrite. The two-processes, overall charge transfer and surface state carrier recombination, are related by a complex two component capacitance arising from the surface states, C_1 and Q_2 (see Figure 2). We speculate that charge transfer is occurring through the surface states and from the pyrite conduction band simultaneously.

The charge transfer to ferric iron in solution is represented in the EC by the CPE Q_1 and a resistance R_2 in parallel. Q_1 is interpreted as representing the space charge capacitance with a contribution from surface roughness and the Hemholtz double layer. The Q_1 admittance is highest for the Ni-doped pyrite, most variable and next highest for Co-doped pyrite and lowest for the undoped pyrite, with the As doped pyrite not far above (Figure 4A). The higher values are interpreted as evidence for the effect of additional surface states and possible Fermi-level pinning on the capacitance of the depletion region. The lower admittance for the As-doped pyrite may be related to its p-type conductivity. For the populations of corrected vs. non-corrected phase angles and for the high and low AC response scores (2) this admittance is statistically the same. For the natural samples Q_1 is higher for those with higher impurity content (Table 2).

The charge transfer resistance, R_2, is defined as the negative reciprocal slope of the current overpotential curve near the origin (30, 37). The value for R_2 was constrained by the inferred low frequency intersection of the impedance semicircle with the Z_{real} axis (Figure 1B). In cases where the extrapolated value was vague, values were arrived at by adjusting plausible values until the best calculated fit to the data was obtained. In the case of semiconductor electrodes and electrodes with non-ideal behavior, the impedance semicircle is often depressed. Nevertheless, it is often interpreted that the intersection of the depressed semicircle with the Z_{real} axis represents the charge transfer resistance or the overall faradaic resistance associated with the system (25, 38). The variation in R_2 is normally distributed and statistically equal for the different dopant populations. However, when the electrodes are grouped according to their behavior in the AC voltammetry experiment (2)(see Appendix II) we find the predicted true

mean for the corrected phase angle group and for the high AC response group to be higher than the non-corrected and low AC response group at the 99% confidence level (Figure 4B, Appendix II). Charge transfer resistance can be used as a measure of kinetic facility. Interestingly, R_2 is statistically higher for the electrodes that respond well to the AC voltammetry experiment. These two phenomena seem to contradict each other for, on one hand, the charge transfer resistance is a measure of kinetic facility but so is the magnitude of the AC response (30, 39). Therefore one would expect low charge transfer resistance to correlate with high AC response. One explanation could be that the EIS data was gathered over a longer time span than the AC voltammetry scan at 100 Hz allowing a surface build up of reaction product perhaps containing elemental sulfur (34). Thus electrodes with higher AC response would also be

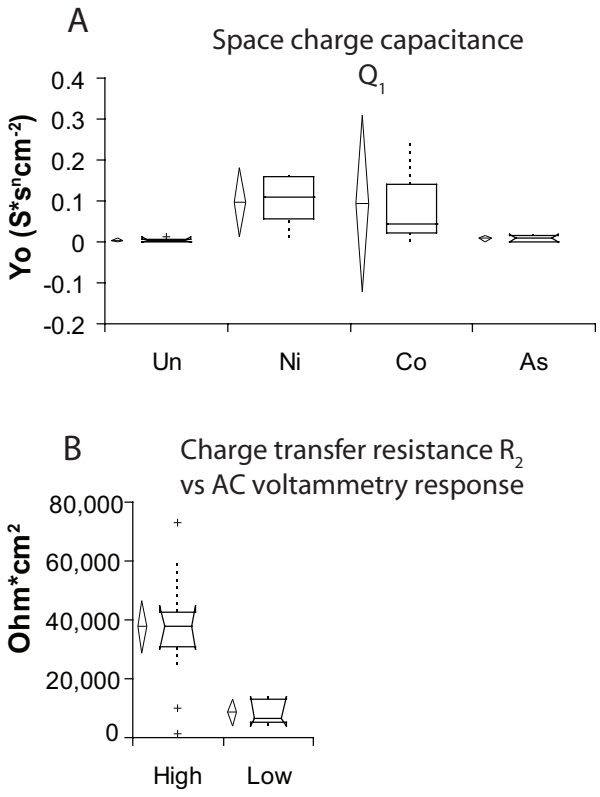

Figure 4. A. Statistical comparison of the equivalent circuit element values for Q_1 with the electrodes grouped according to dopant type. B. Comparison of the charge transfer resistance values for the electrodes grouped according to their relative response to the AC voltammetry (2)

the ones to accumulate more reaction product resulting in higher charge transfer resistance.

An alternate interpretation for this reverse correlation is to postulate that the electrodes with high AC response also have high surface state mediated charge transfer. According to Marcus theory (30, 37), electron transfer occurs when the energy level of a transmitting and accepting orbital in contact are the same. Therefore, if the accepting orbitals of the oxidant (ferric iron) are located in the band gap of the pyrite electrode, charge transfer can not occur in the absence of surface states. Since the energy levels of the aqueous species fluctuate in response to polarized water molecules, the accepting energy levels have a probability distribution that may extend to the conduction band (see Figure 2). This would allow limited charge transfer to occur even when the mean accepting orbital energy of the ferric iron is in the band gap. Most likely though, the reduction of ferric iron at n-type pyrite occurs by transfer of electrons directly from the conduction band and in a two step process via surface states. The correlation of high charge transfer resistance with high AC response current can be explained if charge transfer directly from the conduction band, though limited, would have less resistance than two-step processes mediated by surface states. The high AC response is only possible when there is an abundance of surface state mediated charge transfer and, in this case, the charge transfer resistance is higher. Hens and Gomes (40) report the recombination resistance, such as that associated with a hole injection into a surface state followed by the capture of a conduction band electron and hole injection into the valence band, is identical to the faradaic resistance of a direct charge transfer process in the high frequency limit.

Charge transfer resistance is also higher for the electrodes that were successfully corrected for the non-faradaic current in calculation of their peak phase angles (2)(Appendix II). The results of the AC voltammetry suggest that failure to obtain meaningful phase angles after subtracting the measured non-faradaic impedance is related to an unknown or underestimated impedance element. We speculate that additional space charge impedance would need to be subtracted for the electrodes with meaningless phase angles. The impedance measured in the solution without the redox couple (non-faradaic) underestimated the space charge capacitance

that was present with the redox couple. For the electrodes with corrected phase angles, higher charge transfer resistance combined with lower space charge impedance due to surface states enabled the system to behave more like a metal (2) and thus the non-faradaic impedance was accurately measured in the solution without the redox couple. Therefore, high charge transfer resistance may be correlated with high surface state density. For the natural samples R_2 was highest for the Ni-dominated and As dominated samples (Table 2).

Surface state capacitance

The two circuit elements, Q_2 and C_1, are in parallel and are interpreted as representing a complex capacitance exhibiting both ideal and non-ideal behavior. We interpret these elements to be associated with surface states. Surface states are often invoked to describe processes at the semiconductor/electrolyte interface but they are often poorly defined. Surface electronic states can arise from solution species adsorbed at the surface or from lattice defects in the surface material. They can be thought of as being in equilibrium, through charge transfer, with the solution or with the electrode material depending upon the medium with which the charge transfer is fastest (14). The Q_2 admittance is interpreted to be from the non-ideal behavior associated with surface states communicating with the solution species, such as sulfur states bonding with the oxygen in water molecules. The ideal capacitance C_1 is interpreted to represent the surface states arising from defects in bulk pyrite intersecting the surface. Capacitance C_1 is lowest for As-doped and Ni-doped electrodes as would be expected for a higher density of occupied surface states. Lower capacitance (C_1) for both high AC response and corrected phase angle electrode populations (2) also fits with the hypothesis that defect states within the bandgap lead to occupied surface states is. Also, C_1 is two to three orders of magnitude lower for the natural samples with higher impurity content possibly indicating high surface state density (Table 2).

The median for Q_2 is highest for As-doped and Ni-doped pyrite which supports the hypothesis that surface states from these defects may contribute to charge transfer. Q_2 is the same, however, for populations of electrodes with corrected and non-corrected phase angles

and for electrodes with high and low AC response. This is interpreted to mean that surface state capacitance on the solution side of the interface is relatively unaffected by the capacitance due to electrode defect surface states. Q_2 values are close for the natural samples and similar to the synthetic samples (Table 2).

Recombination in the inner circuit loop

The mechanism described above could be modeled as hole injection with carrier recombination by electrons from the valence or conduction band. In terms of band theory, a ferric ion from solution injects a hole into an occupied surface state in the band gap which then recombines with an electron from the valence or conduction band in a two step charge transfer process. Another proposed mechanism has either impurity or photo-activated holes from the pyrite valence band engaged in nucleophilic attack of water molecules with subsequent adsorption of OH radicals and the progression of sulfur to sulfate (33). This could involve a recombination reaction as valence band holes interact with occupied surface states, for example, in As-doped pyrite. Both processes have been modeled with an equivalent circuit similar to the inner faradaic loop of our model but without the Warburg impedance (12). However, the Warburg impedance in our model improved the fit to the experimental data.

Therefore, C_2, R_3 are a capacitance and resistance in parallel interpreted to represent charge transfer from bulk pyrite to surface states. All populations of C_2 are normally distributed and statistically equal, though the As-doped population is the highest followed by Ni-doped pyrite as would be expected if these impurities increase the surface state mediated charge transfer. A further indication that this capacitance might be related to surface state recombination is that for the high AC response and corrected phase angle electrode populations (2) C_2 is statistically higher at the 94% and 99% confidence level respectively (see Figure 5). For the natural samples C_2 is highest for sample L3B with the lowest impurity content and lowest for the sample M3F with second lowest impurity content but all samples are within an order of magnitude. Again, no significance can be drawn due to few samples and multiple impurities.

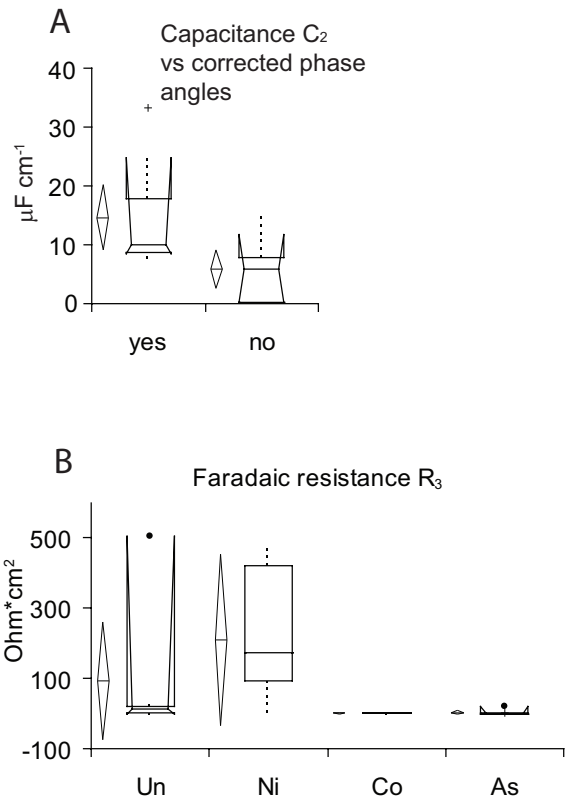

Figure 5. A. statistical comparison of values for element C_2 for electrodes grouped according to whether their AC voltammetry data gave meaningful phase angle values after subtracting the non faradaic impedance measured in the absence of the redox couple. B. Comparison of the values for element R_3 for electrodes grouped according to dopant type.

The resistance R_3, is substantially higher for the Ni-doped electrodes and lowest for the As-doped followed by the Co-doped electrodes (see Figure 5). We interpret high Ni-doped electrode resistance for R_3 as indicating carrier recombination at surface states arising from the defect state deep in the Ni-doped pyrite band gap. In the case of As and Co, the defect states are near the valence and conduction bands, respectively, facilitating carrier recombination. For Ni-doped and undoped electrodes the injected holes at the surface are most likely recombined with electrons from the valence band. The undoped electrodes primarily have surface state defects associated with lattice discontinuation. The result is a spread of energy levels from different lattice orientations. Though the surface state density is less for the undoped electrode, the energy levels are spread out. The same is true for the doped electrodes but the effect is domi-

nated by the defect surface state density. Therefore, the Ni-doped electrodes with their defect states farthest away from the bulk energy bands have the highest recombination resistance (R_3). Overall the recombination resistance is lower for the more reactive electrodes. R_3 is lower at the 97 % and 90 % confidence levels respectively for the high AC response electrodes (2) and the group with corrected phase angles. For the natural electrodes the highest R_3 value is for sample 9D with Co as the dominant impurity. This value is of the same order of magnitude as the synthetic Ni-doped electrodes. Electrode M3F with low impurity content but with Ni the highest has a low value for R_3 while the value for sample 3A, dominated by As, Bi and Pb, is 1 x 10^{-7}, essentially zero.

The Warburg impedance may be associated with diffusion of the electro-active species to the interface from the bulk pyrite or with diffusion of ferric ions to the interface from the solution. Though it might be assumed that diffusion of ferric ions from solution should be modeled by placing the Warburg impedance next to C_2, its position in the inner circuit gave the best fit to the data. The natural samples have higher Warburg impedance for low impurity samples which could indicate diffusion of charge carriers from the bulk pyrite. The Warburg impedance is statistically the same for all synthetic populations implying that differences in observed reactivity of the various synthetic electrodes is not due to either the supply of ionic species or of charge carriers but is the result of a charge transfer mechanism that varies with impurity type.

While interpretation of an EC is speculative, insights gained from comparing the circuit elements in this study are based on the previous work characterizing the electrical properties, impurity concentrations, and electrochemical oxidation behavior of these electrodes (2) as well as semiconductor electrochemical theory (12, 26). The fact that all the electrodes could be modeled by the same circuit lends credence to the model.

Conclusions

All the electrodes were modeled with the equivalent circuit: $R_1(Q_1R_2)$

$(Q_2(C_1(C_2(R_3W))))$ where R_1 is solution/sample resistance, Q_1 is space charge/Hemholtz capacitance, R_2 is charge transfer resistance, Q_2 is frequency dependent surface state capacitance, C_1 is pure surface state capacitance, C_2 is secondary faradaic pseudo-capacitance, R_3 is secondary faradaic resistance, and W is Warburg impedance. The elements are interpreted and explained, according to semiconductor/electrolyte interface theory, to suggest that defect states in the bulk pyrite arising from impurity atoms become surface states at the interface and affect oxidation kinetics by mediating charge transfer. The data clearly show that charge transfer resistance is greatest for electrodes that also respond with higher current to AC voltammetry scans at 100 Hz. Though this may be due to the build up of reaction products during the time span of collecting the EIS data it could also be interpreted to indicate a two step charge transfer mechanism mediated by surface states.

Acknowledgements

I would like to thank Daniela Stefan for her assistance with pyrite synthesis, for providing the natural pyrite thick sections and for work on the natural pyrite characterization. We thank Sankaran Mahadevan for support through NSF-DGE 0114329 (Integrative Graduate Education and Research Traineeship for Reliability and Risk Engineering Management (Vanderbilt University Department of Civil and Environmental Engineering). This study was supported by NSF-EAR 0409155 and 0617396 (KSS).

References

1. S. W. Lehner, K. S. Savage and J. C. Ayers, *Journal of Crystal Growth*, 286, 306 (2006).

2. S. Lehner, K. Savage, M. Ciobanu and D. E. Cliffel, *Geochimica et Cosmochimica Acta*, 71, 2491 (2007).

3. M. A. Williamson and J. D. Rimstidt, *Geochimica et Cosmochimica Acta*, 58, 5443 (1994).

4. C. O. Moses, D. Kirk Nordstrom, J. S. Herman and A. L. Mills, *Geochimica et Cosmochimica Acta*, 51, 1561 (1987).

5. S. W. Lehner and K. S. Savage, *Geochimica et Cosmochimica Acta* (In review).

6. R. N. Chandler and R. W. Bene, *Physical Review B.*, 8, 4979 (1973).

7. P. Moller and G. Kersten, *Mineralium Deposita*, 29, 404 (1994).

8. R. T. Shuey, *Semiconducting Ore Minerals*, Elsevier Scientific Publishing Co, Amsterdam (1975).

9. K. S. Savage, D. Stefan and S. W. Lehner, *Applied Geochemistry* (In review).

10. K. S. Savage, T. N. Tingle, P. A. O'Day, G. A. Waychunas and D. K. Bird, *Applied Geochemistry*, 15, 1219 (2000).

11. P. Velasquez, L. Dietmar, J. Pascual, J. R. Ramos-Barrado, P. Grez, H. Gomez, R. Schrebler, R. Del Rio and R. Cordova, *Journal of Physical Chemistry B*, 109, 4977 (2005).

12. W. P. Gomes and D. Vanmaekelburg, *Electrochimica Acta*, 41, 967 (1995).

13. J. F. McCann and S. P. S. Badwal, *Journal of the Electrochemical Society*, 129, 551 (1982).

14. L. M. Peter, J. Li and R. Peat, *Journal of Electroanalytical Chemistry*, 165, 29 (1984).

15. J. Li and L. M. Peter, *Journal of Electroanalytical Chemistry*, 193, 27 (1985).

16. J. Li and L. M. Peter, *Journal of Electroanalytical Chemistry*, 199, 1 (1986).

17. R. Peat and L. M. Peter, *Journal of Electroanalytical Chemistry*, 209, 307 (1986).

18. K. Rajeshwar, *Journal of the Electrochemical Society*, 129, 1003 (1982).

19. J. J. Kelly and R. Memming, *Journal of the Electrochemical Society*, 129, 730 (1982).

20. G. Oskam, D. Vanmaekelbergh and J. J. Kelly, *Electrochimica Acta*, 38, 301 (1993).

21. J. N. Chazalviel, *Journal of the Electrochemical Society*, 129, 963 (1982).

22. A. Goossens and J. Schoonman, *Journal of the Electrochemical Society*, 139, 893 (1992).

23. M. Tomkiewicz, *Electrochimica Acta*, 35, 1631 (1990).

24. J. Pang, Briceno and S. Chander, *Journal of the Electrochemical Society*, 137, 3447 (1990).

25. H. K. Lin and W. C. Say, *Journal of Applied Electrochemistry*, 29, 987 (1999).

26. S. R. Morrison, *Electrochemistry at semiconductor and oxidized metal electrodes*, p. 401, Plenum Press, New York and London (1980).

27. J. D. Rimstidt and D. J. Vaughan, *Geochimica et Cosmochimica Acta*, 67, 873 (2003).

28. S. A. Wilson, W. I. Ridley and A. E. Koenig, *Journal of Analytical Atomic Spectrometry*, 17, 406 (2002).

29. B. Yeum, ZsimpWin Version 3.20, in, Princeton Applied Research (2004).

30. A. J. Bard and L. R. Faulkner, *Electrochemical Methods: Fundamentals and Applications 2nd Edition*, p. 833, John Wiley and Sons Inc., Hoboken, New Jersey (2001).

31. C. Liu, Q. Bi, A. Leyland and A. Matthews, *Corrosion Science*, 45, 1243 (2003).

32. N. Takami and N. Koura, *Electrochimica Acta*, 33, 69 (1988).

33. K. K. Mishra and K. Osseo Asare, *Journal of the Electrochemical Society*, 139, 749 (1992).

34. G. H. Kelsall, Q. Yin, D. J. Vaughan, K. E. R. England and N. P. Brandon, *Journal of Electroanalytical Chemistry*, 471, 116 (1999).

35. A. Hung, J. Muscat, I. Yarovsky and S. P. Russo, *Surface Science*, 520, 111 (2002).

36. A. Hung, J. Muscat, I. Yarovsky and S. P. Russo, *Surface Science*, 513, 511 (2002).

37. R. A. Marcus, *The Journal of Chemical Physics*, 43, 679 (1965).

38. J. R. Macdonald, *Impedance spectroscopy emphasizing solid materials and systems*, p. 346, John Wiley & Sons, New York (1987).

39. P. M. Marcus, *IBM Journal*, November, 496 (1964).

40. Z. Hens and W. P. Gomes, *Journal of Electroanalytical Chemistry*, 437, 77 (1997).

CHAPTER V

IMPLICATIONS AND RECOMENDATIONS

These studies have shown that the electrochemical oxidation of pyrite near pH 2 is affected by impurity concentration. Since most natural pyrite contains impurities in comparable concentration to the synthetic pyrite used in this work, it probably safe to say that most pyrite oxidation studies have been affected by impurities without understanding the nature of this effect. The importance of my research is in furthering the understanding of the role of impurities and the nature of charge transfer at the pyrite/solution interface in acid environments. It is important to understand the mechanisms of a process so critical to the environmental health of mining-impacted watersheds. Pyrite is known to contain a wide variety of impurities and my research has only opened the door for future studies. It may well be that there exists some critical combination of impurities that results in drastically increased rates of charge transfer and acid production but we have not found that increase with As, Co, or Ni individually.

Nevertheless, our research was a critical first step because we have been able to document effects of these three widespread minor elements on pyrite's oxidation behavior. What we have shown is that pyrite without significant impurities oxidizes more slowly than pyrite with any one of these three minor elements. We have also shown that typical examples of natural pyrite with combinations of impurities oxidize approximately at the same rate as the As-doped, Ni-doped or Co-doped synthetic pyrite. In addition it appears that the forced anodic dissolution of pyrite is the best proxy for pyrite oxidation occurring in the absence of applied potential. Our studies have shown that arsenic in the pyrite crystal structure produces holes for charge carriers which enhance the reactivity of such pyrite, perhaps by an alternate charge transfer pathway known as corrosion by holes (Morrison, 1980).

There are a number of possible directions for future research on the relation of impurities to pyrite oxidation. One is to explore the effect of various combinations of impurities on pyrite oxidation using synthetic and natural samples. Another direction would be to con-

centrate on the role of As and try to synthesize a wider range of As concentrations in order to define a rate law with As concentration as an argument. Further work needs to be done to determine the fate of the As released to solution as arsenian pyrite is oxidized. It is possible that we didn't detect As release in the experiments described in Chapter II because it was below the detection limit of our method. It is also possible that As is released as some secondary insoluble phase or that it preferentially remains in the pyrite during an incongruent dissolution reaction. Characterization of reaction products on the surface of As-bearing pyrite or improved methods of solution analysis would shed light on this question.

Another direction for future research would be to explore the consequences of pyrite with both n-and p-type conducting regions. Do such pyrites become galvanic cells in contact with an electrolyte solution? It has been shown that certain such natural pyrites have been able to generate an electrical current from the exposure to sunlight in a similar mechanism to photovoltaic cells (Tributsch et al., 2003). Is it possible that life evolved from constituent elements on the surface of such pyrite in the anoxic CO_2 rich Archean atmosphere? Can inexpensive and relatively non-toxic pyrite be developed into a photovoltaic collector material?

The energy of the conduction band in pyrite has been determined to be – 4.92 eV below the energy of an electron in a vacuum (Xu and Schoonen, 2000). The energy of an electron in a vacuum is taken to be 4.5eV above the standard hydrogen electrode. This would put the conduction band of pyrite at approximately 0.02 to 0.22 eV above the Ag/AgCl 3M KCl reference electrode used in our studies. However, the energy of the conduction band of pyrite undergoing a redox reaction is a function of the electrochemical system and it will vary depending on the ratio of ferric to ferrous iron, the concentration of surface states and the nature and species of the adsorbed ions at the surface. The potential-determining ions for pyrite in a solution with high concentration of iron have yet to be confirmed. Exchange of electrons with the solution will result in lowering the energy of the bands in the bulk as the space charge region becomes depleted of charge carriers in n-type pyrite. If surface state concentration is high enough to define the equilibrium with the bulk pyrite then the Fermi level will be pinned in re-

lation to the conduction band and the energy level is free to equilibrate with the redox ratio of the iron couple in solution. The peak potential of the ferric iron reduction reaction in both the cyclic voltammetry and AC voltammetry experiments was around 0.44 V vs Ag/AgCl 3M KCl. The standard reduction potential of the iron couple is 0.771V above the SHE or about 0.57 V above the Ag/AgCl reference electrode, with which our results are in relatively good agreement. However, the reduction potential for a multi-electron transfer reaction is more complicated (Xu and Schoonen, 2000). Our experiments are carried out in near pH 2 acid. The pH of zero charge for pyrite is 1.4 (Xu and Schoonen, 2000) suggesting that our pyrite electrodes are negatively charged at rest potential though the space charge region may be positive with respect to the bulk solid.

The diagrams drawn in this study to conceptualize the charge transfer processes at the semiconductor/electrolyte interface have the iron redox couple in the energy range of the pyrite band gap. The theoretical considerations described above combined with experimental evidence that the reaction easily takes place indicate that these conceptual diagrams are reasonable. The hypothesis that intra-bandgap surface states introduced by bulk impurity defect states (or "gap states") foster increased charge transfer can neither be fully accepted nor refuted by the available evidence. Therefore, it would be desirable to measure the energy levels of the gap states and the intra-gap surface states with electrochemical photo-capacitance spectroscopy.

Another direction for future research would be to correlate the electronic charge transfer mechanisms with elemental species and specific crystallographic sites. While work has been done on the possible surface species and chemical mechanisms involved in pyrite oxidation, there are some unanswered questions. Where are the impurity orbitals in relation to derived molecular orbital theory positions for the pyrite crystal structure? How might they affect the postulated chemical mechanisms of pyrite oxidation? By correlating the energy of the redox couple, the band structure and the molecular orbitals with their associated species and crystallographic position perhaps an understanding of the potential pathways for charge transfer involved in pyrite oxidation could be achieved.

We have shown, using synthetic and natural pyrite, that impurity elements affect its semiconducting properties which vary orders of magnitude and display either positive or negative charge carriers depending on the impurity. Furthermore, these differences affect pyrite oxidation behavior. Therefore, variability in the chemical composition of pyrite has potentially wide ranging implications, from the spontaneous evolution of life to the development of solar energy, in addition to affecting the production rate of acid drainage and the release of potentially toxic elements in the many environments where naturally occurring pyrite is exposed to oxidizing conditions.

References

Morrison, S. R., 1980, Electrochemistry at semiconductor and oxidized metal electrodes: New York and London, Plenum Press, 401 p.

Tributsch, H., Fiechter, S., Jokisch, D., Rojas-Chapana, J., and Ellmer, K., 2003, Photoeletrochemical power, chemical energy and catalytic activity for organic evolution on natural pyrite interfaces: Origins of Life and Evolution of the Biosphere, v. 32, p. 129-162.

Xu, Y., and Schoonen, M. A. A., 2000, The absolute energy of conduction and valence bands of selected semiconducting minerals: American Mineralogist, v. 85, p. 543-556.

APPENDIX I

Program script for Phreeqc[1] ferric iron concentration and speciation calculation

```
SOLUTION 1
  temp     25
  pH       2
  pe       15
  redox    pe
  units    mmol/kgw
  density  1
  Fe(2)    0 pe
  Fe(3)    1 pe
  Na       10
  Cl       14.2 charge
  O(0)     0.00036 pe
  -water   1 # kg
INCREMENTAL_REACTIONS True
REACTION 1
  Pyrite   1
  0.00001 moles in 500 steps
```

Data from Chapter III experiments

Table 1. Concentrations of reaction progress variables (RPV) in solutions collected from batch reactor experiments

Batch reactor data

* calculated surface area of pyrite sample, ** mass of solution = 0.6 kg

Sample	Time (seconds)	Ferric iron (molal)	Ferrous iron (molal)	Sulfate (molal)	A* (m^2)	A/M** (m^2kg^{-1})
Undoped 4					0.113	0.189
	300	5.54E-4	2.33E-5	3.10E-5		
	600	5.48E-4	2.78E-5	3.73E-5		
	900	5.44E-4	3.31E-5	4.90E-5		
	1200	5.39E-4	3.76E-5	4.74E-5		
	1800	5.32E-4	4.83E-5	5.40E-5		
	2400	5.25E-4	5.28E-5	6.09E-5		
	3000	5.18E-4	6.00E-5	6.53E-5		
	3900	5.09E-4	7.16E-5	7.36E-5		

1 http://wwwbrr.cr.usgs.gov/projects/GWC_coupled/phreeqc/

Batch reactor data

* calculated surface area of pyrite sample, ** mass of solution = 0.6 kg

Sample	Time (seconds)	Ferric iron (molal)	Ferrous iron (molal)	Sulfate (molal)	A* (m^2)	A/M** (m^2kg^{-1})
Undoped 5					0.113	0.189
	300	5.55E-4	3.13E-5	1.54E-5		
	600	5.52E-4	2.33E-5	1.94E-5		
	900	5.48E-4	2.78E-5	4.54E-5		
	1200	5.45E-4	3.04E-5	2.89E-5		
	1800	5.39E-4	3.85E-5	3.73E-5		
	2400	5.33E-4	3.94E-5	4.14E-5		
	3000	5.28E-4	4.75E-5	5.37E-5		
	3900	5.21E-4	5.46E-5	5.72E-5		
Undoped 6					0.120	0.200
	300	5.55E-4	2.60E-5	1.77E-5		
	600	5.52E-4	3.22E-5	1.85E-5		
	900	5.48E-4	2.95E-5	2.72E-5		
	1200	5.45E-4	3.13E-5	3.49E-5		
	1800	5.39E-4	3.67E-5	4.15E-5		
	2400	5.34E-4	4.21E-5	4.65E-5		
	3000	5.29E-4	4.57E-5	5.74E-5		
	3900	5.22E-4	5.37E-5	5.71E-5		
Undoped 7					0.113	0.189
	300	5.57E-4	1.97E-5	1.63E-5		
	600	5.55E-4	2.06E-5	1.87E-5		
	900	5.52E-4	2.33E-5	2.33E-5		
	1200	5.50E-4	2.60E-5	3.07E-5		
	1800	5.46E-4	3.04E-5	2.85E-5		
	2400	5.42E-4	3.22E-5	3.74E-5		
	3000	5.38E-4	3.49E-5	3.82E-5		
	3900	5.33E-4	4.30E-5	4.73E-5		
Undoped 8					0.113	0.189
	300	5.56E-4	2.15E-5	1.60E-5		
	600	5.53E-4	2.60E-5	2.33E-5		
	900	5.49E-4	3.13E-5	3.10E-5		
	1200	5.46E-4	3.40E-5	3.67E-5		
	1800	5.40E-4	4.12E-5	5.03E-5		
	2400	5.35E-4	4.83E-5	5.70E-5		
	3000	5.30E-4	5.28E-5	6.51E-5		
	3900	5.24E-4	6.09E-5	8.41E-5		

Batch reactor data

* calculated surface area of pyrite sample, ** mass of solution = 0.6 kg

Sample	Time (seconds)	Ferric iron (molal)	Ferrous iron (molal)	Sulfate (molal)	A* (m^2)	A/M** (m^2kg^{-1})
Undoped 9					0.118	0.197
	300	5.55E-4	2.42E-5	5.40E-5		
	600	5.51E-4	2.86E-5	4.79E-5		
	900	5.47E-4	4.21E-5	5.29E-5		
	1200	5.44E-4	4.03E-5	5.65E-5		
	1800	5.38E-4	4.66E-5	6.39E-5		
	2400	5.33E-4	5.19E-5	6.56E-5		
	3000	5.28E-4	5.55E-5	1.01E-4		
	3900	5.21E-4	6.36E-5	8.28E-5		
As-doped 3					0.191	0.319
	300	5.52E-4	2.78E-5	2.96E-5		
	600	5.45E-4	3.40E-5	3.69E-5		
	900	5.41E-4	4.12E-5	4.46E-5		
	1200	5.37E-4	4.75E-5	4.80E-5		
	1800	5.29E-4	5.64E-5	5.81E-5		
	2400	5.22E-4	6.54E-5	5.42E-5		
	3000	5.16E-4	7.34E-5	7.09E-5		
	3900	5.07E-4	8.51E-5	7.62E-5		
As-doped 4					0.116	0.194
	300	5.55E-4	lost	1.71E-5		
	600	5.50E-4	2.33E-5	2.36E-5		
	900	5.46E-4	2.86E-5	3.46E-5		
	1200	5.42E-4	lost	6.32E-5		
	1800	5.35E-4	4.30E-5	4.41E-5		
	2400	5.28E-4	4.75E-5	5.23E-5		
	3000	5.22E-4	5.19E-5	5.78E-5		
	3900	5.14E-4	6.18E-5	7.57E-5		
As-doped 5					0.143	0.238
	300	5.53E-4	2.15E-5	1.96E-5		
	600	5.48E-4	2.51E-5	2.52E-5		
	900	5.44E-4	3.13E-5	3.85E-5		
	1200	5.41E-4	3.31E-5	4.10E-5		
	1800	5.34E-4	4.39E-5	4.98E-5		
	2400	5.28E-4	4.57E-5	5.49E-5		
	3000	5.22E-4	5.28E-5	6.05E-5		
	3900	5.14E-4	5.91E-5	6.65E-5		

Batch reactor data

* calculated surface area of pyrite sample, ** mass of solution = 0.6 kg

Sample	Time (seconds)	Ferric iron (molal)	Ferrous iron (molal)	Sulfate (molal)	A* (m^2)	A/M** (m^2kg^{-1})
As-doped 6					0.114	0.190
	300	5.55E-4	2.06E-5	1.97E-5		
	600	5.50E-4	2.60E-5	2.22E-5		
	900	5.46E-4	3.22E-5	2.83E-5		
	1200	5.42E-4	3.49E-5	3.21E-5		
	1800	5.35E-4	4.03E-5	3.94E-5		
	2400	5.29E-4	4.83E-5	5.12E-5		
	3000	5.24E-4	5.28E-5	6.28E-5		
	3900	5.16E-4	5.82E-5	6.90E-5		
As-doped 7					0.128	0.214
	300	5.53E-4	2.42E-5	2.58E-5		
	600	5.48E-4	lost	3.40E-5		
	900	5.43E-4	3.58E-5	4.14E-5		
	1200	5.38E-4	3.85E-5	4.54E-5		
	1800	5.30E-4	4.75E-5	5.93E-5		
	2400	5.23E-4	5.64E-5	6.55E-5		
	3000	5.17E-4	6.18E-5	7.59E-5		
	3900	5.08E-4	6.98E-5	9.04E-5		
As-doped 8					0.163	0.271
	300	5.51E-4	2.60E-5	6.65E-5		
	600	5.46E-4	3.22E-5	3.81E-5		
	900	5.41E-4	3.76E-5	5.00E-5		
	1200	5.37E-4	4.03E-5	5.14E-5		
	1800	5.28E-4	5.01E-5	6.40E-5		
	2400	5.21E-4	5.64E-5	7.39E-5		
	3000	5.15E-4	6.45E-5	8.18E-5		
	3900	5.06E-4	7.52E-5	9.17E-5		
Co-doped 3					0.114	0.190
	300	5.54E-4	2.24E-5	1.99E-5		
	600	5.49E-4	2.69E-5	2.59E-5		
	900	5.44E-4	3.22E-5	3.14E-5		
	1200	5.41E-4	3.67E-5	3.65E-5		
	1800	5.34E-4	5.28E-5	6.77E-5		
	2400	5.27E-4	5.10E-5	4.91E-5		
	3000	5.22E-4	5.55E-5	5.65E-5		
	3900	5.14E-4	6.36E-5	5.15E-5		

Batch reactor data

* calculated surface area of pyrite sample, ** mass of solution = 0.6 kg

Sample	Time (seconds)	Ferric iron (molal)	Ferrous iron (molal)	Sulfate (molal)	A* (m^2)	A/M** (m^2kg^{-1})
Co-doped 4					0.114	0.190
	300	5.53E-4	2.24E-5	2.82E-5		
	600	5.48E-4	2.69E-5	3.22E-5		
	900	5.43E-4	3.22E-5	5.17E-5		
	1200	5.39E-4	3.67E-5	4.28E-5		
	1800	5.31E-4	4.48E-5	5.12E-5		
	2400	5.25E-4	5.19E-5	6.34E-5		
	3000	5.19E-4	5.73E-5	6.49E-5		
	3900	5.11E-4	6.54E-5	7.64E-5		
Co-doped 5					0.148	0.246
	300	5.52E-4	2.42E-5	2.02E-5		
	600	5.47E-4	3.22E-5	3.27E-5		
	900	5.42E-4	3.22E-5	3.21E-5		
	1200	5.38E-4	3.58E-5	4.35E-5		
	1800	5.30E-4	4.39E-5	5.47E-5		
	2400	5.23E-4	5.55E-5	6.38E-5		
	3000	5.17E-4	6.09E-5	7.15E-5		
	3900	5.11E-4	6.63E-5	7.92E-5		
Co-doped 6					0.140	0.233
	300	5.53E-4	2.33E-5	1.60E-5		
	600	5.48E-4	3.04E-5	2.84E-5		
	900	5.43E-4	3.67E-5	5.03E-5		
	1200	5.39E-4	4.21E-5	5.12E-5		
	1800	5.31E-4	5.19E-5	6.65E-5		
	2400	5.24E-4	6.00E-5	7.50E-5		
	3000	5.18E-4	6.80E-5	8.65E-5		
	3900	5.10E-4	7.79E-5	9.69E-5		
Co-doped 7					0.132	0.219
	300	5.55E-4	4.48E-5	2.22E-5		
	600	5.50E-4	2.78E-5	2.78E-5		
	900	5.47E-4	3.22E-5	3.53E-5		
	1200	5.43E-4	3.58E-5	4.05E-5		
	1800	5.37E-4	4.57E-5	5.69E-5		
	2400	5.31E-4	5.01E-5	6.08E-5		
	3000	5.26E-4	5.55E-5	7.24E-5		
	3900	5.19E-4	6.36E-5	7.55E-5		

Batch reactor data

* calculated surface area of pyrite sample, ** mass of solution = 0.6 kg

Sample	Time (seconds)	Ferric iron (molal)	Ferrous iron (molal)	Sulfate (molal)	A* (m^2)	A/M** (m^2kg^{-1})
Co-doped 8					0.138	0.230
	300	5.53E-4	2.69E-5	2.47E-5		
	600	5.48E-4	2.95E-5	3.22E-5		
	900	5.43E-4	3.13E-5	3.77E-5		
	1200	5.39E-4	3.94E-5	4.79E-5		
	1800	5.32E-4	4.92E-5	5.79E-5		
	2400	5.25E-4	5.64E-5	7.00E-5		
	3000	5.19E-4	6.00E-5	7.71E-5		
	3900	5.11E-4	6.63E-5	8.64E-5		
Ni-doped 3					0.151	0.251
	300	5.54E-4	2.24E-5	1.69E-5		
	600	5.50E-4	3.31E-5	2.93E-5		
	900	5.45E-4	3.49E-5	3.62E-5		
	1200	5.41E-4	3.85E-5	4.49E-5		
	1800	5.34E-4	4.66E-5	5.43E-5		
	2400	5.28E-4	5.64E-5	6.51E-5		
	3000	5.22E-4	5.64E-5	6.50E-5		
	3900	5.15E-4	6.18E-5	7.51E-5		
Ni-doped 4					0.117	0.195
	300	5.54E-4	2.42E-5	2.98E-5		
	600	5.50E-4	2.95E-5	4.06E-5		
	900	5.46E-4	3.40E-5	4.29E-5		
	1200	5.41E-4	3.85E-5	4.62E-5		
	1800	5.34E-4	4.48E-5	5.62E-5		
	2400	5.27E-4	5.73E-5	6.36E-5		
	3000	5.21E-4	5.73E-5	6.54E-5		
	3900	5.12E-4	7.07E-5	7.29E-5		
Ni-doped 5					0.113	0.189
	300	5.55E-4	2.06E-5	1.52E-5		
	600	5.51E-4	2.51E-5	1.85E-5		
	900	5.47E-4	2.78E-5	2.05E-5		
	1200	5.44E-4	3.58E-5	2.96E-5		
	1800	5.37E-4	4.12E-5	3.45E-5		
	2400	5.30E-4	4.30E-5	5.00E-5		
	3000	5.25E-4	5.01E-5	5.75E-5		
	3900	5.17E-4	5.82E-5	6.69E-5		

Batch reactor data

* calculated surface area of pyrite sample, ** mass of solution = 0.6 kg

Sample	Time (seconds)	Ferric iron (molal)	Ferrous iron (molal)	Sulfate (molal)	A* (m^2)	A/M** (m^2kg^{-1})
Ni-doped 6					0.122	0.203
	300	5.54E-4	2.24E-5	2.20E-5		
	600	5.49E-4	2.60E-5	2.44E-5		
	900	5.45E-4	3.13E-5	3.39E-5		
	1200	5.41E-4	3.58E-5	4.46E-5		
	1800	5.34E-4	4.30E-5	4.92E-5		
	2400	5.28E-4	5.10E-5	5.74E-5		
	3000	5.22E-4	5.55E-5	7.14E-5		
	3900	5.14E-4	6.36E-5	8.25E-5		
Ni-doped 7					0.148	0.247
	300	5.53E-4	2.15E-5	2.32E-5		
	600	5.47E-4	3.04E-5	3.14E-5		
	900	5.42E-4	3.49E-5	3.86E-5		
	1200	5.37E-4	3.94E-5	4.43E-5		
	1800	5.29E-4	5.10E-5	5.55E-5		
	2400	5.22E-4	5.46E-5	6.71E-5		
	3000	5.16E-4	6.18E-5	7.45E-5		
	3900	5.07E-4	6.80E-5	8.47E-5		
Ni-doped 8					0.124	0.207
	300	5.53E-4	2.33E-5	1.67E-5		
	600	5.48E-4	3.04E-5	2.32E-5		
	900	5.44E-4	3.31E-5	3.24E-5		
	1200	5.40E-4	3.76E-5	3.79E-5		
	1800	5.33E-4	4.39E-5	5.03E-5		
	2400	5.27E-4	5.01E-5	6.29E-5		
	3000	5.21E-4	5.82E-5	6.61E-5		
	3900	5.13E-4	6.45E-5	8.01E-5		
Elba					0.137	0.228
	300	5.55E-4	2.15E-5	1.94E-5		
	600	5.52E-4	2.24E-5	2.32E-5		
	900	5.48E-4	2.60E-5	2.81E-5		
	1200	5.46E-4	2.95E-5	2.92E-5		
	1800	5.40E-4	3.49E-5	4.05E-5		
	2400	5.35E-4	3.85E-5	4.94E-5		
	3000	5.31E-4	4.48E-5	1.42E-4		
	3900	5.25E-4	4.66E-5	6.88E-5		

Batch reactor data

* calculated surface area of pyrite sample, ** mass of solution = 0.6 kg

Sample	Time (seconds)	Ferric iron (molal)	Ferrous iron (molal)	Sulfate (molal)	A* (m^2)	A/M** (m^2kg^{-1})
Leadville					0.110	0.183
	300	5.54E-4	2.15E-5	3.09E-5		
	600	5.50E-4	2.86E-5	3.45E-5		
	900	5.45E-4	3.22E-5	4.03E-5		
	1200	5.41E-4	3.58E-5	4.57E-5		
	1800	5.34E-4	4.30E-5	5.47E-5		
	2400	5.28E-4	5.10E-5	6.22E-5		
	3000	5.22E-4	5.64E-5	6.90E-5		
	3900	5.14E-4	6.27E-5	7.92E-5		

Table 2. Concentrations of RPV in solutions collected from mixed flow-through reactor data

Mixed flow-through reactor data

Flow rate = 7.84E-5 kg s^{-1}

Sample	RPV	Initial conc. (molal)	Steady state conc. (molal)	Surface area (m2)
Undoped 4				0.1131
	Ferric iron	5.598E-4	5.243E-4	
	Ferrous iron	0.000	5.999E-5	
	Sulfate	6.035E-5	7.491E-5	
Undoped 5				0.1131
	Ferric iron	5.607E-4	5.262E-4	
	Ferrous iron	0.000	5.909E-5	
	Sulfate	1.201E-5	7.557E-5	
Undoped 6				0.1201
	Ferric iron	5.600E-4	5.260E-4	
	Ferrous iron	0.000	5.999E-5	
	Sulfate	2.475E-5	7.426E-5	
Undoped 7				0.1131
	Ferric iron	5.605E-4	5.402E-4	
	Ferrous iron	0.000	4.208E-5	
	Sulfate	6.847E-6	5.652E-5	
Undoped 8				0.1131
	Ferric iron	5.602E-4	5.338E-4	
	Ferrous iron	0.000	5.551E-5	
	Sulfate	6.163E-6	9.619E-5	

Mixed flow-through reactor data

Flow rate = 7.84E-5 kg s^{-1}

Sample	RPV	Initial conc. (molal)	Steady state conc. (molal)	Surface area (m2)
Undoped 9				0.1185
	Ferric iron	5.611E-4	5.229E-4	
	Ferrous iron	1.343E-5	7.252E-5	
	Sulfate	1.851E-5	1.119E-4	
As-doped 3				0.1914
	Ferric iron	5.602E-4	5.262E-4	
	Ferrous iron	1.612E-5	6.357E-5	
	Sulfate	8.046E-6	7.219E-5	
As-doped 4				0.1162
	Ferric iron	5.604E-4	5.010E-4	
	Ferrous iron	1.432E-5	1.003E-4	
	Sulfate	2.547E-5	9.541E-5	
As-doped 5				0.1427
	Ferric iron	5.598E-4	4.977E-4	
	Ferrous iron	1.432E-5	9.848E-5	
	Sulfate	3.359E-5	1.054E-4	
As-doped 6				0.1141
	Ferric iron	5.598E-4	5.279E-4	
	Ferrous iron	1.343E-5	5.640E-5	
	Sulfate	9.256E-7	8.165E-5	
As-doped 7				0.1282
	Ferric iron	5.600E-4	5.006E-4	
	Ferrous iron	1.612E-5	9.311E-5	
	Sulfate	5.379E-6	1.167E-4	
As-doped 8				0.1626
	Ferric iron	5.606E-4	5.006E-4	
	Ferrous iron	1.522E-5	1.101E-4	
	Sulfate	1.135E-5	1.250E-4	
Co-doped 3				0.1140
	Ferric iron	5.595E-4	4.900E-4	
	Ferrous iron	1.880E-5	1.092E-4	
	Sulfate	2.392E-5	9.053E-5	

Mixed flow-through reactor data

Flow rate = 7.84E-5 kg s^{-1}

Sample	RPV	Initial conc. (molal)	Steady state conc. (molal)	Surface area (m2)
Co-doped 4				0.1142
	Ferric iron	5.605E-4	5.356E-4	
	Ferrous iron	1.074E-5	4.656E-5	
	Sulfate	6.446E-6	6.681E-5	
Co-doped 5				0.1478
	Ferric iron	5.595E-4	5.194E-4	
	Ferrous iron	1.612E-5	6.715E-5	
	Sulfate	1.258E-7	8.594E-5	
Co-doped 6				0.1396
	Ferric iron	5.595E-4	4.971E-4	
	Ferrous iron	1.253E-5	1.092E-4	
	Sulfate	1.164E-5	1.242E-4	
Co-doped 7				0.1316
	Ferric iron	5.608E-4	5.021E-4	
	Ferrous iron	1.522E-5	1.039E-4	
	Sulfate	1.458E-5	1.253E-4	
Co-doped 8				0.1382
	Ferric iron	5.603E-4	5.199E-4	
	Ferrous iron	1.970E-5	6.983E-5	
	Sulfate	1.243E-5	1.116E-4	
Ni-doped 3				0.1505
	Ferric iron	5.582E-4	5.193E-4	
	Ferrous iron	1.522E-5	6.804E-5	
	Sulfate	1.564E-5	8.513E-5	
Ni-doped 4				0.1173
	Ferric iron	5.595E-4	5.028E-4	
	Ferrous iron	1.432E-5	9.043E-5	
	Sulfate	1.348E-5	8.988E-5	
Ni-doped 5				0.1131
	Ferric iron	5.600E-4	5.035E-4	
	Ferrous iron	1.432E-5	9.132E-5	
	Sulfate	1.039E-5	9.527E-5	
Ni-doped 6				0.1218
	Ferric iron	5.600E-4	5.338E-4	
	Ferrous iron	1.432E-5	5.461E-5	
	Sulfate	2.818E-6	7.015E-5	

Mixed flow-through reactor data

Flow rate = 7.84E-5 kg s^{-1}

Sample	RPV	Initial conc. (molal)	Steady state conc. (molal)	Surface area (m2)
Ni-doped 7				0.1481
	Ferric iron	5.607E-4	5.245E-4	
	Ferrous iron	1.343E-5	6.446E-5	
	Sulfate	8.937E-6	9.684E-5	
Ni-doped 8				0.1244
	Ferric iron	5.598E-4	5.280E-4	
	Ferrous iron	1.701E-5	8.505E-5	
	Sulfate	5.862E-6	8.581E-5	
Elba				0.1366
	Ferric iron	5.602E-4	5.006E-4	
	Ferrous iron	1.522E-5	9.490E-5	
	Sulfate	2.134E-5	1.273E-4	
Leadville				0.1096
	Ferric iron	5.597E-4	5.083E-4	
	Ferrous iron	1.701E-5	8.505E-5	
	Sulfate	1.568E-5	1.117E-4	

APPENDIX II

Supplemental information for the EIS study (Chapter IV)

Correlation of EIS and AC voltammetry scans

The diagrams below are useful to visualize the correspondence of the AC voltammetry scans at 100 Hz from Chapter II with the EIS spectra. The frequency of 100Hz in the EIS scan occurs very near to the high frequency intersection with the Z_{real} axis in the Nyquist plots (Figure 1). For a more sluggish reaction the kinetic impedance begins at lower frequency. The onset

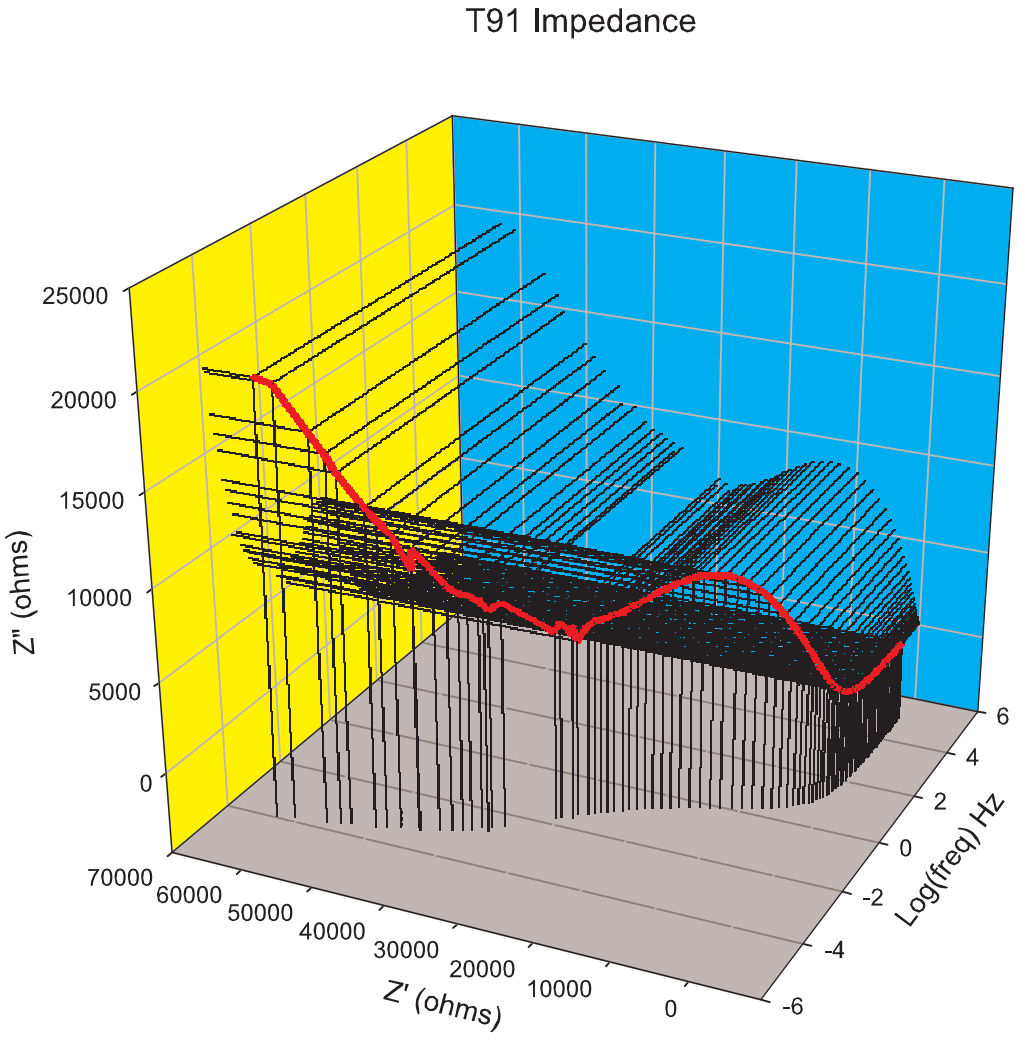

Figure 1. EIS impedance spectra displayed in three dimensions

of kinetic impedance is correlated with increasing phase angles in the EIS scan (Figure 2). The electrodes with high AC response scores described in Chapter II have higher phase angles in the EIS scan at 100Hz with a statistical probability of 99%, meaning that the kinetic impedance starts at a higher frequency. Also, AC response score is higher for electrodes with corrected phase angles at 99% probability. Table 1 reports the total impedance value and phase angle at 100 Hz for the different electrodes. Tables 2, and 3 show the electrode populations grouped according to high or low AC response and to AC voltammetry phase angle correction.

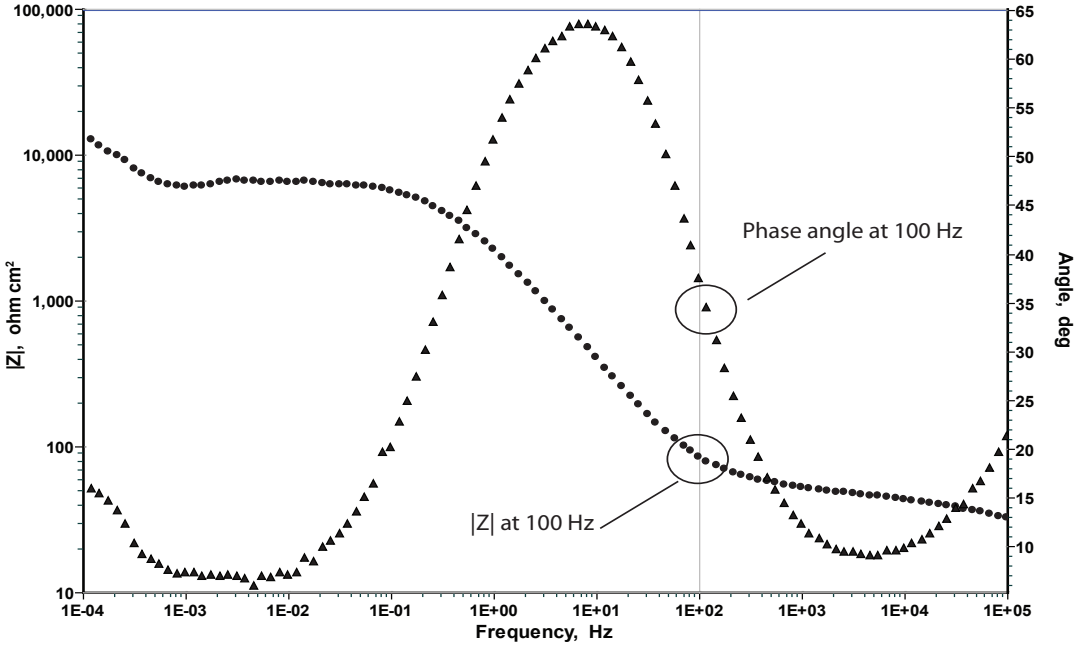

Figure 2. Bode plot for EIS scan of 7331a As-doped electrode with low AC response score

Table 1. The absolute value of total impedance and the phase angle from EIS spectra at ~ 100Hz

Electrode	$\|Z\|$ (ohms-cm^2)	Phase angle (deg)	AC response score
Un 7280B, As	188	47.8	6.1
Un 72, Ni	246	33.0	0.1
Un 7279B, As, Ni	214	69.1	12.1
As T110	269	75.3	6.2
As 91C	197	42.6	0
As T112	227	74.6	2.7
As 3A	230	71.2	8.1
As T102A	222	58.6	7.9
As 7332A	7.92	58.4	4.7
As 7326	126	67.4	3.6
As 7331A	86.1	37.5	0.6
As 96B	191	50.5	7
Co 7272	226	74.7	6.1
Co 7236D	169	65.6	3.7
Co 7228A	108	65.0	0
Ni 85B	197	64.9	0
Ni 90B	268	77.4	6.7
Ni 7296	236	71.8	6.6
Ni 7290B	185	75.6	11.7
L3B As	12.3	40.6	na
3A Pb, Bi, As	230	71.2	8.1
9D Co	163	63.8	na
6000C Co	166	64.8	na
M3F Ni	113	51.5	na

Table 2. Identity of electrodes with high and low AC response scores

High AC score	Low AC score
7280B	Un 72
7279B	91C
T110	7331A
T112	7228A
As 3A	Ni 85B
T102A	
7332A	
T7326	
96B	
Co 7272	
7236D	
90B	
T7296	
7290B	

Table 3. Electrodes grouped according to phase angle correction

Corrected	Non-corrected
7279B	7280B
T110	Un 72
T112	91C
As 3A	T102A
T7326	7331A
96B	7236D
Co 7272	7228A
T7296	Ni 85B
7290B	90B

Diagrams of model fits for EC: R(QR)(Q(C(C(RW))))

Open squares represent the calculated fit while the solid dots represent the measured data.

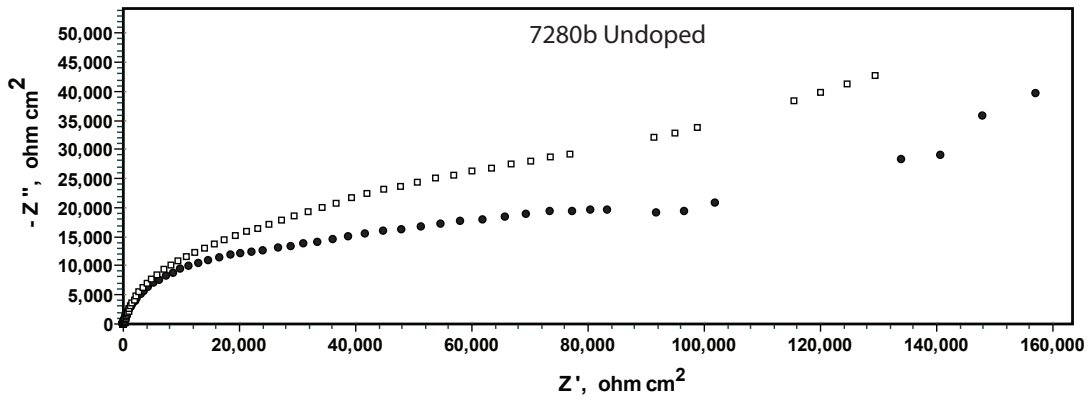

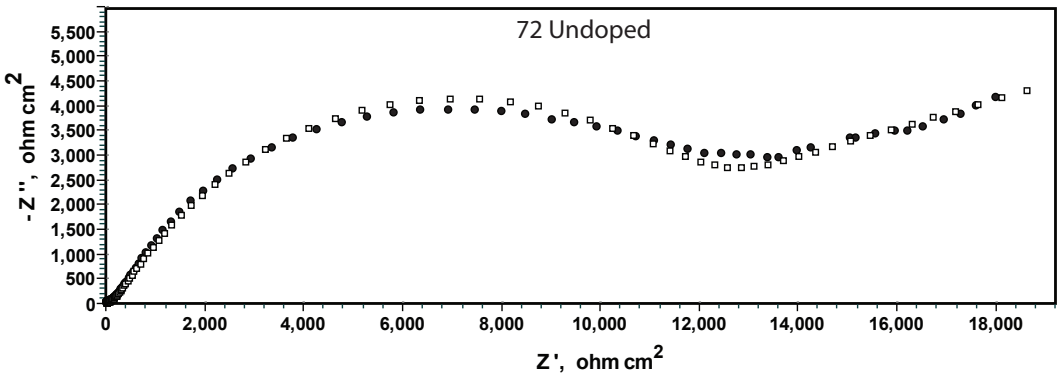

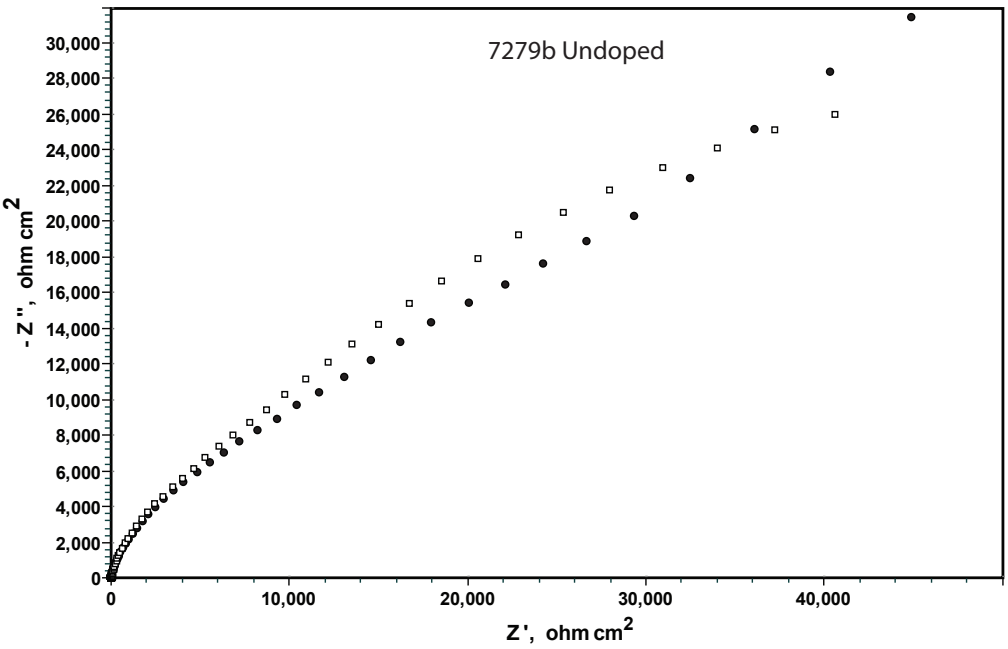
7279b Undoped
-Z'', ohm cm2
Z', ohm cm2
0
2,000
4,000
6,000
8,000
10,000
12,000
14,000
16,000
18,000
20,000
22,000
24,000
26,000
28,000
30,000
0
10,000
20,000
30,000
40,000

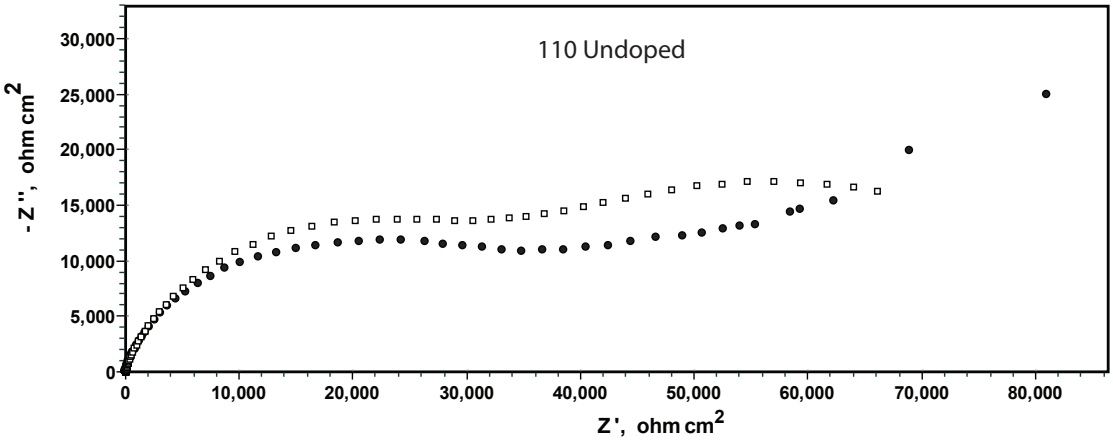
110 Undoped
-Z'', ohm cm2
Z', ohm cm2
0
5,000
10,000
15,000
20,000
25,000
30,000
0
10,000
20,000
30,000
40,000
50,000
60,000
70,000
80,000

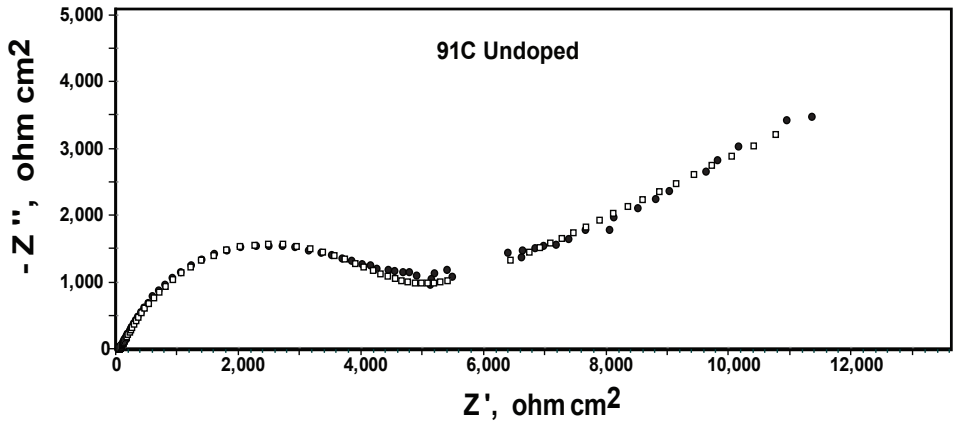
91C Undoped
-Z'', ohm cm2
Z', ohm cm2
0
1,000
2,000
3,000
4,000
5,000
0
2,000
4,000
6,000
8,000
10,000
12,000

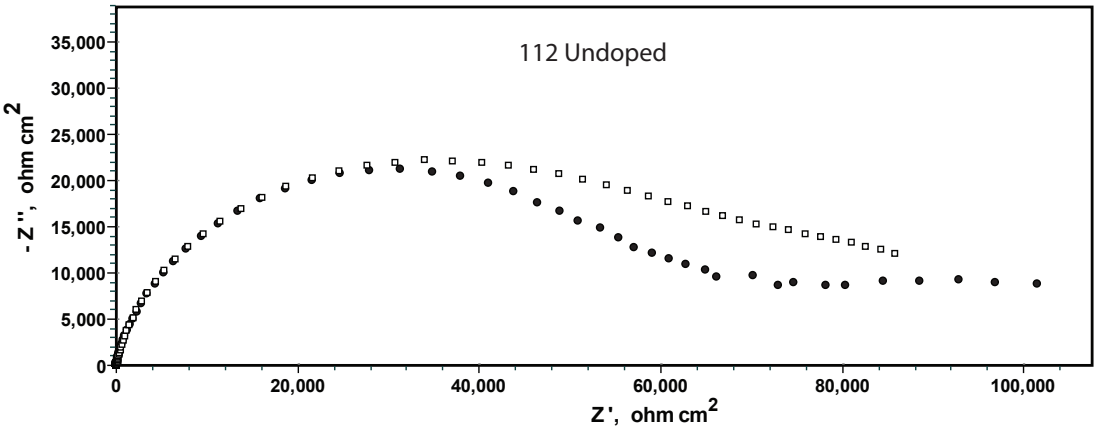
112 Undoped
-Z'', ohm cm2
Z', ohm cm2
0
5,000
10,000
15,000
20,000
25,000
30,000
35,000
0
20,000
40,000
60,000
80,000
100,000

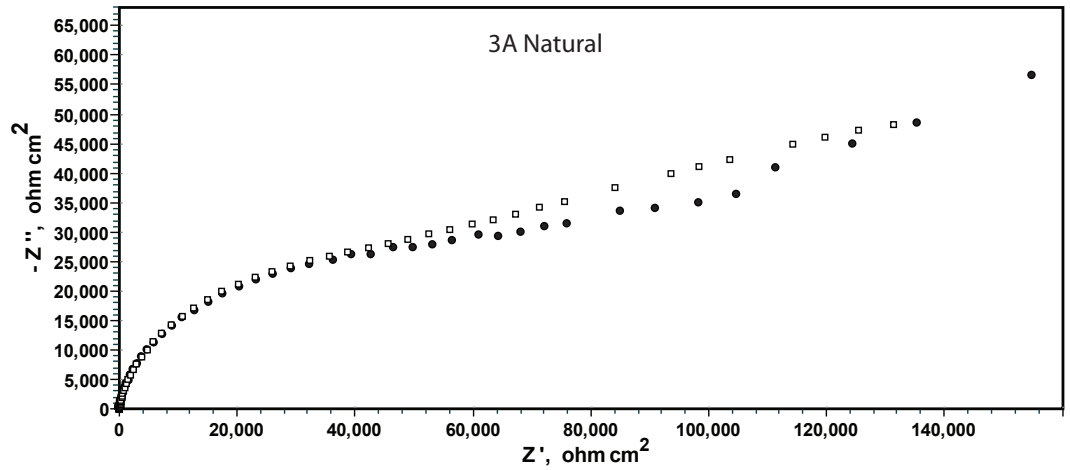
3A Natural
-Z'', ohm cm2
Z', ohm cm2
0
5,000
10,000
15,000
20,000
25,000
30,000
35,000
40,000
45,000
50,000
55,000
60,000
65,000
0
20,000
40,000
60,000
80,000
100,000
120,000
140,000

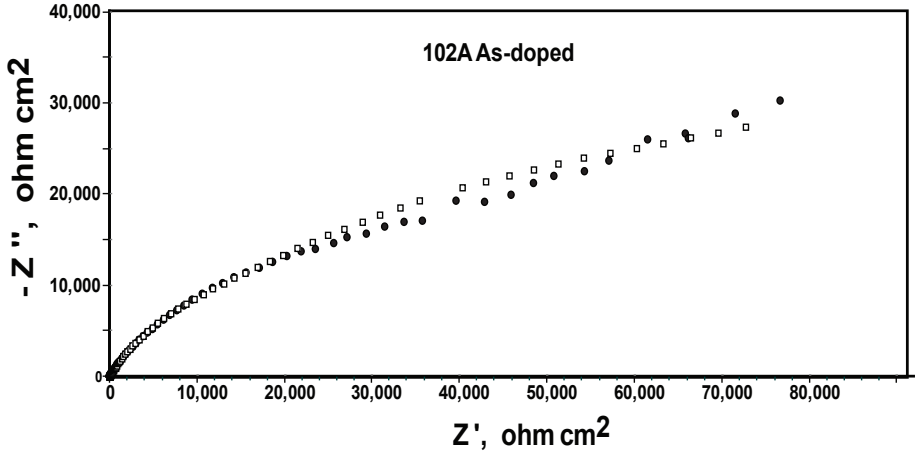
102A As-doped
- Z '', ohm cm2
Z', ohm cm2
0
10,000
20,000
30,000
40,000
0
10,000
20,000
30,000
40,000
50,000
60,000
70,000
80,000

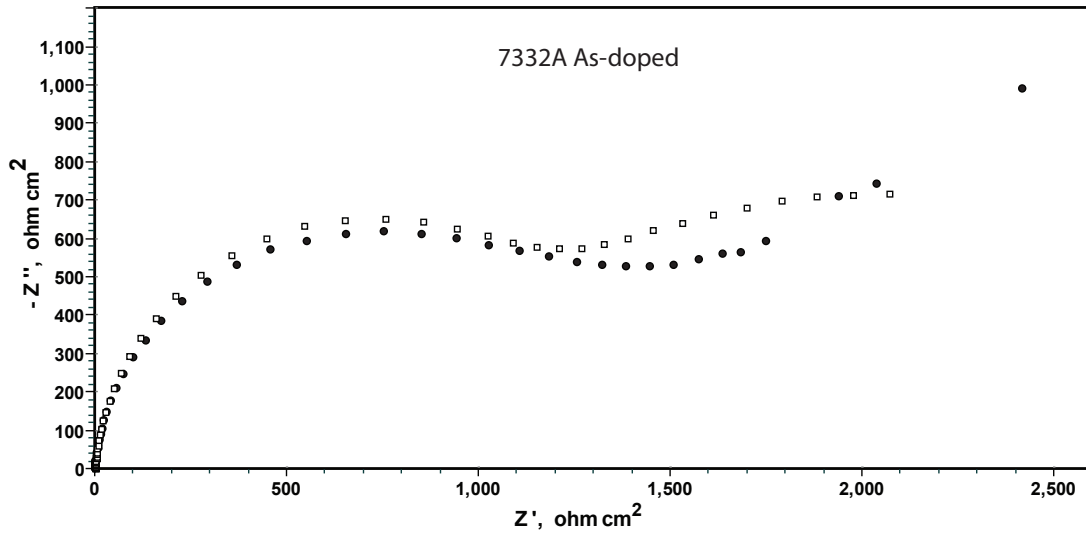
7332A As-doped
- Z '', ohm cm 2
Z ', ohm cm2
0
100
200
300
400
500
600
700
800
900
1,000
1,100
0
500
1,000
1,500
2,000
2,500

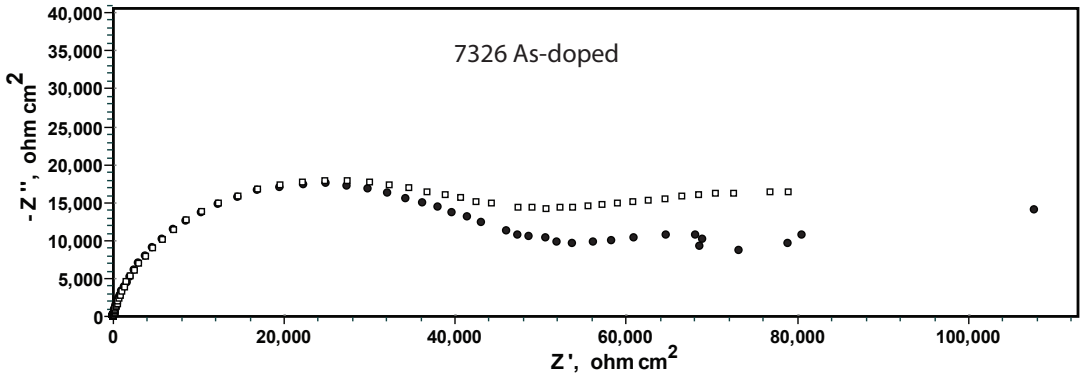
7326 As-doped
- Z '', ohm cm 2
Z ', ohm cm2
0
5,000
10,000
15,000
20,000
25,000
30,000
35,000
40,000
0
20,000
40,000
60,000
80,000
100,000

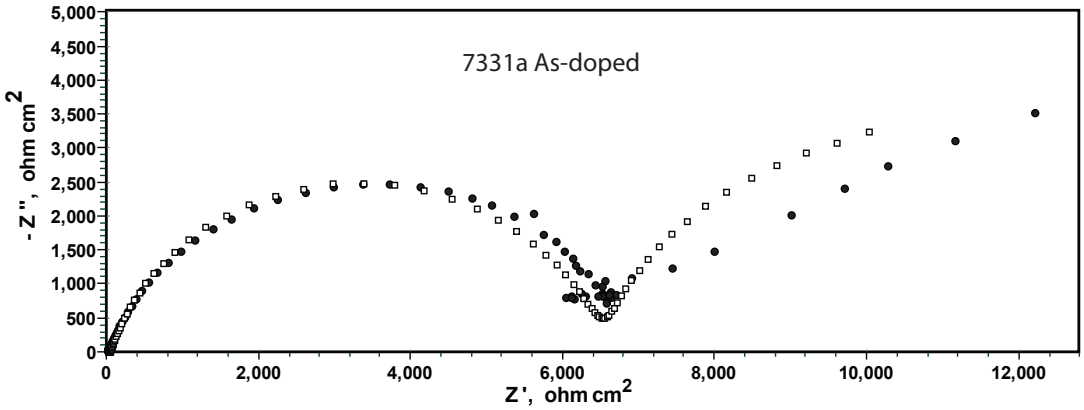
7331a As-doped
- Z '', ohm cm 2
Z ', ohm cm2
0
500
1,000
1,500
2,000
2,500
3,000
3,500
4,000
4,500
5,000
0
2,000
4,000
6,000
8,000
10,000
12,000

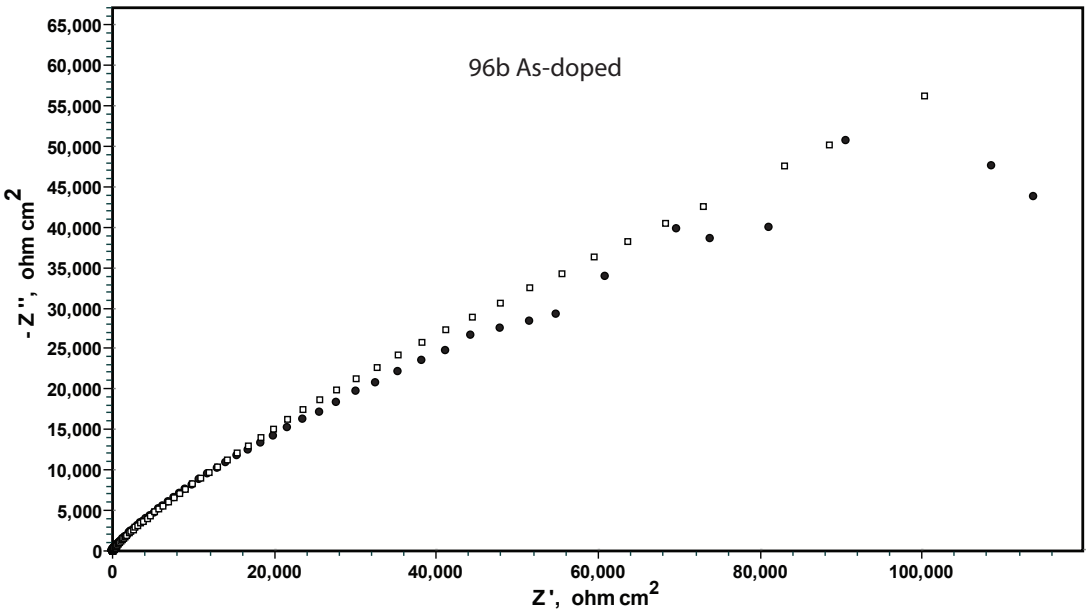
96b As-doped
- Z'', ohm cm2
Z', ohm cm2
65,000
60,000
55,000
50,000
45,000
40,000
35,000
30,000
25,000
20,000
15,000
10,000
5,000
0
0
20,000
40,000
60,000
80,000
100,000

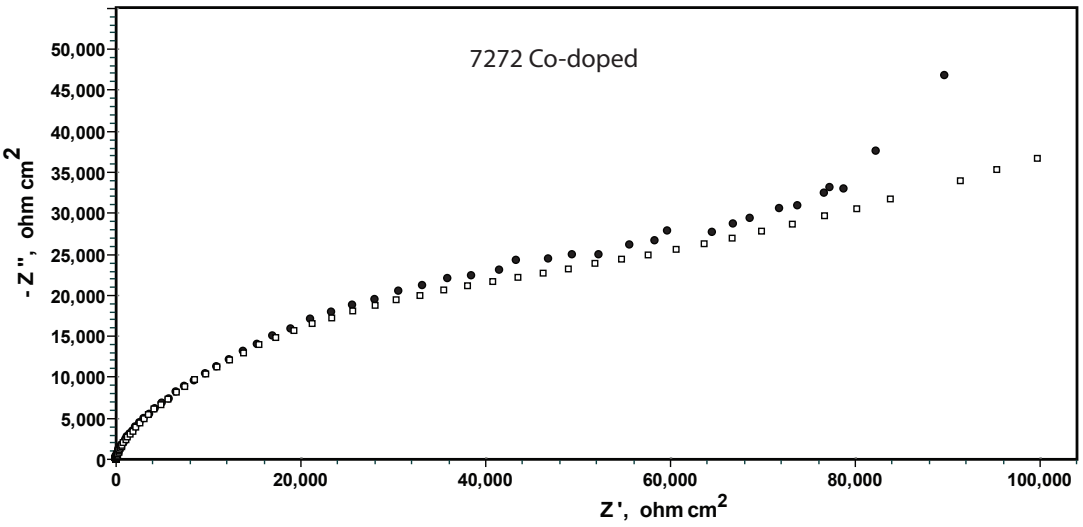
7272 Co-doped
- Z'', ohm cm2
Z', ohm cm2
50,000
45,000
40,000
35,000
30,000
25,000
20,000
15,000
10,000
5,000
0
0
20,000
40,000
60,000
80,000
100,000

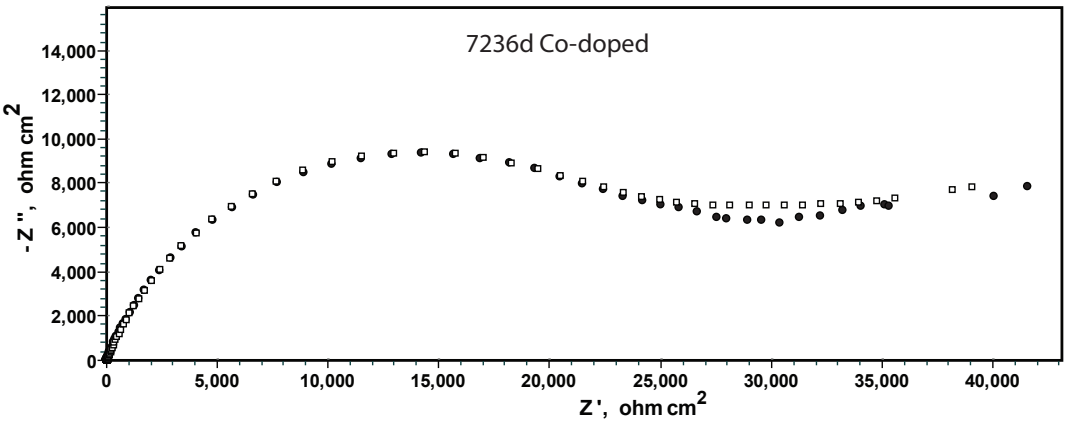
7236d Co-doped
- Z'', ohm cm2
Z', ohm cm2
14,000
12,000
10,000
8,000
6,000
4,000
2,000
0
0
5,000
10,000
15,000
20,000
25,000
30,000
35,000
40,000

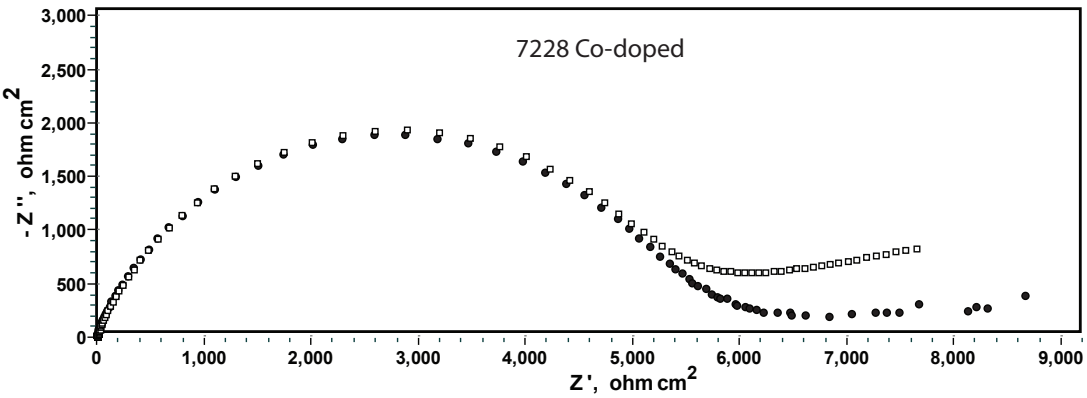
7228 Co-doped
- Z '', ohm cm2
Z ', ohm cm2
3,000
2,500
2,000
1,500
1,000
500
0
0
1,000
2,000
3,000
4,000
5,000
6,000
7,000
8,000
9,000

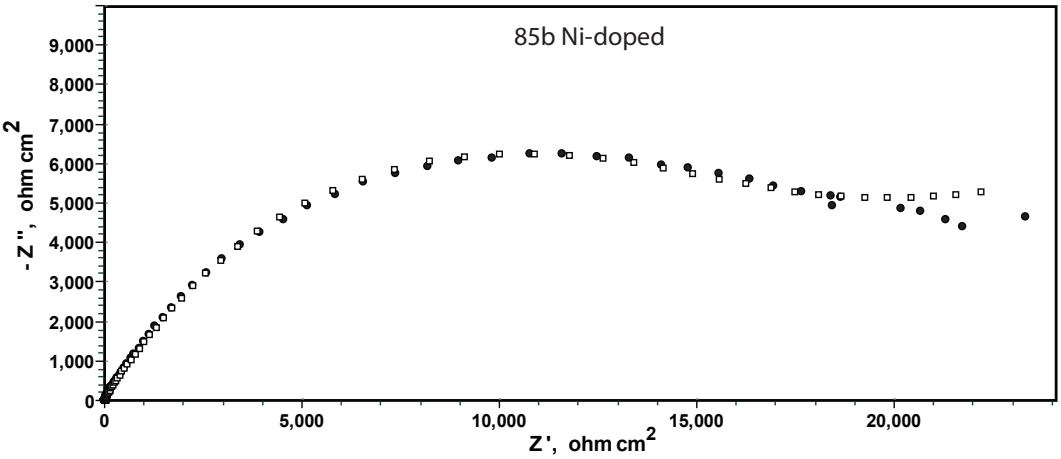
85b Ni-doped
- Z '', ohm cm2
Z ', ohm cm2
9,000
8,000
7,000
6,000
5,000
4,000
3,000
2,000
1,000
0
0
5,000
10,000
15,000
20,000

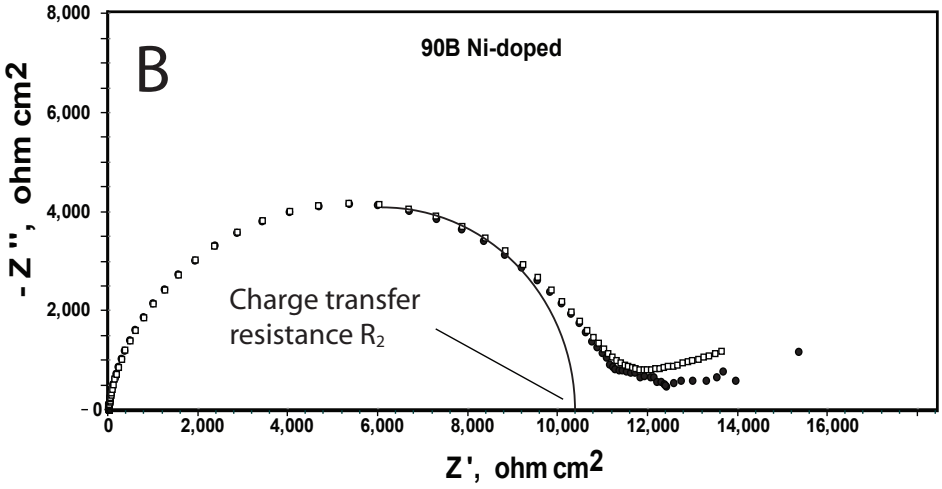
B
90B Ni-doped
- Z '', ohm cm2
Z ', ohm cm2
Charge transfer
resistance R2
8,000
6,000
4,000
2,000
0
0
2,000
4,000
6,000
8,000
10,000
12,000
14,000
16,000

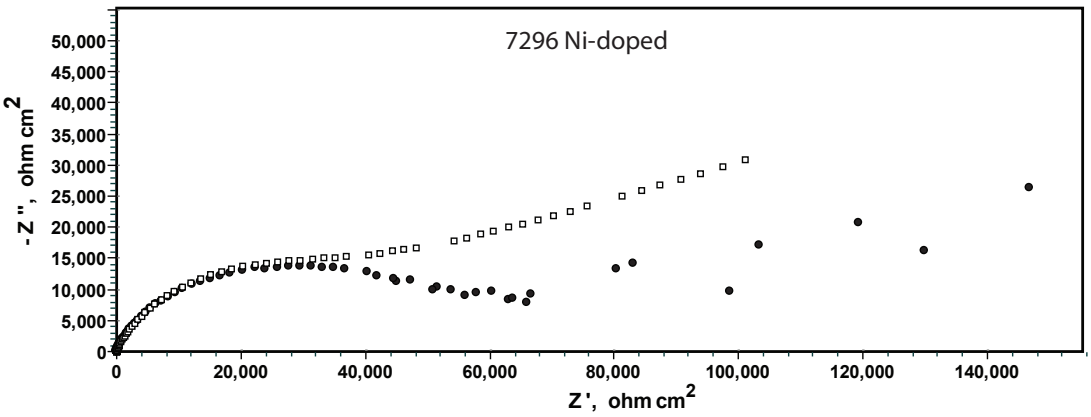
7296 Ni-doped
- Z '', ohm cm2
Z ', ohm cm2
0
5,000
10,000
15,000
20,000
25,000
30,000
35,000
40,000
45,000
50,000
0
20,000
40,000
60,000
80,000
100,000
120,000
140,000

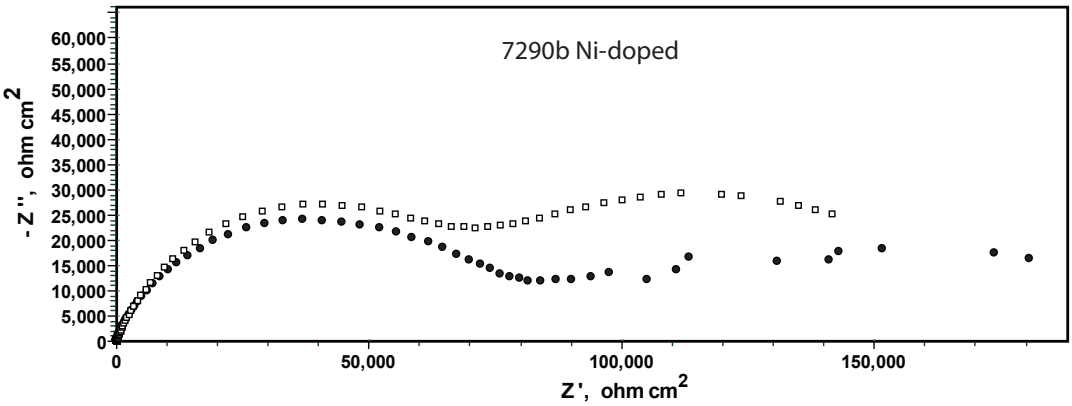
7290b Ni-doped
- Z '', ohm cm2
Z ', ohm cm2
0
5,000
10,000
15,000
20,000
25,000
30,000
35,000
40,000
45,000
50,000
55,000
60,000
0
50,000
100,000
150,000

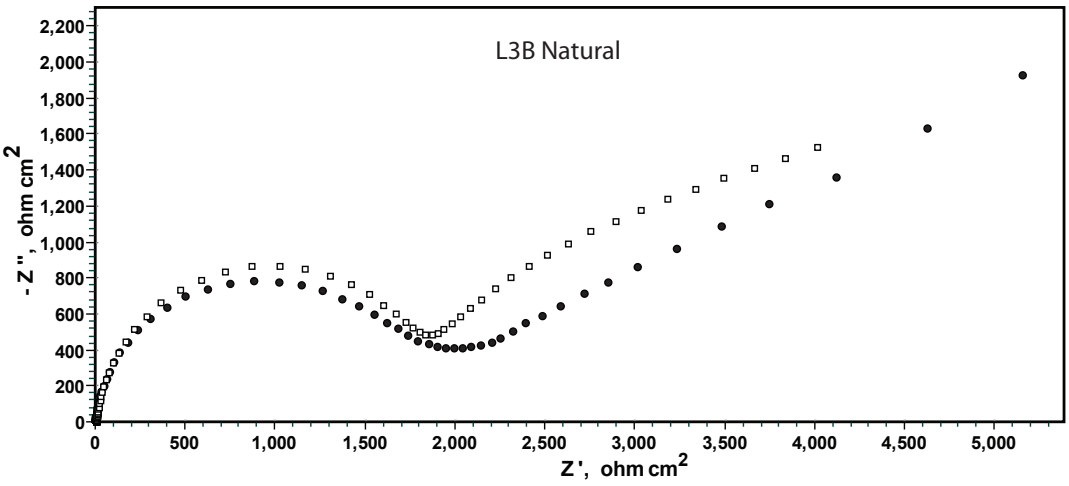
L3B Natural
- Z '', ohm cm2
Z ', ohm cm2
0
200
400
600
800
1,000
1,200
1,400
1,600
1,800
2,000
2,200
0
500
1,000
1,500
2,000
2,500
3,000
3,500
4,000
4,500
5,000

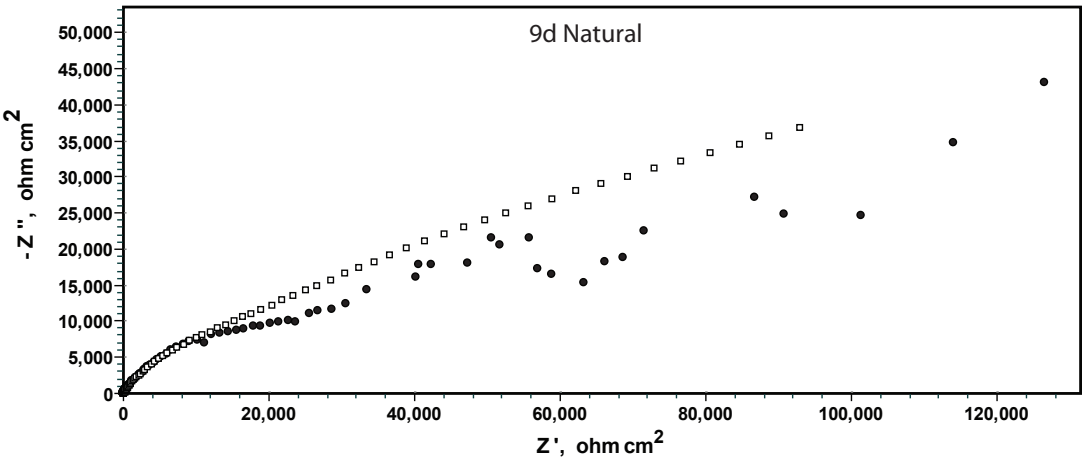
9d Natural
- Z '', ohm cm2
Z ', ohm cm2
0
5,000
10,000
15,000
20,000
25,000
30,000
35,000
40,000
45,000
50,000
0
20,000
40,000
60,000
80,000
100,000
120,000

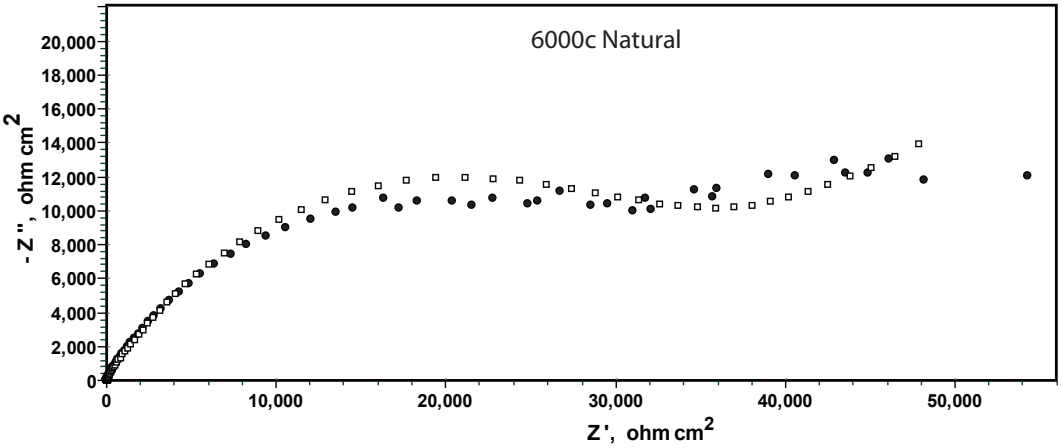
6000c Natural
- Z '', ohm cm2
Z ', ohm cm2
0
2,000
4,000
6,000
8,000
10,000
12,000
14,000
16,000
18,000
20,000
0
10,000
20,000
30,000
40,000
50,000

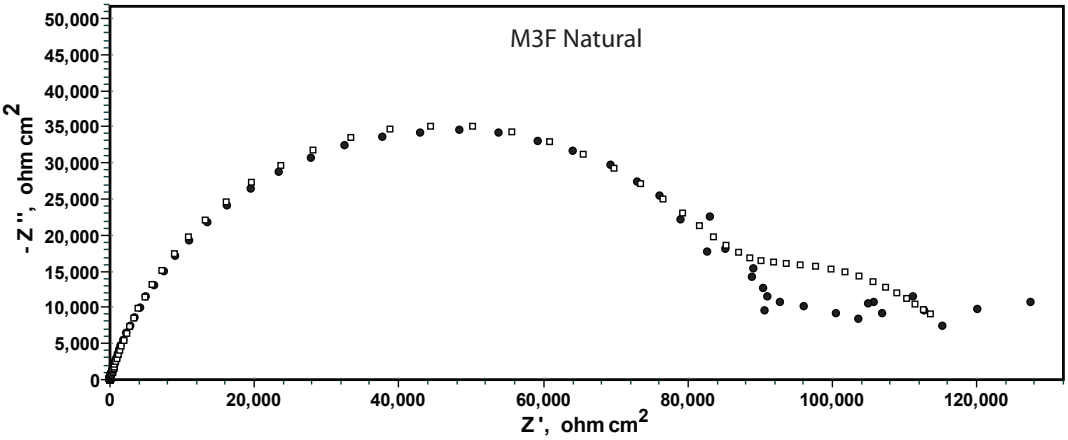
M3F Natural
- Z '', ohm cm2
Z ', ohm cm2
0
5,000
10,000
15,000
20,000
25,000
30,000
35,000
40,000
45,000
50,000
0
20,000
40,000
60,000
80,000
100,000
120,000